Raman Spectroscopy of Tumour Cells Exposed to Clinically Relevant Doses of Ionizing Radiation

by

Samantha Harder
B.Sc., University of Manitoba, 2011

A Thesis Submitted in Partial Fulfillment of the
Requirements for the Degree of

MASTER OF SCIENCE

in the Department of Physics and Astronomy

University of Victoria

Raman Spectroscopy of Tumour Cells Exposed to Clinically Relevant Doses of Ionizing Radiation

by

Samantha Harder
B.Sc., University of Manitoba, 2011

Supervisory Committee

Dr. Andrew Jirasek, Supervisor
(Department of Physics and Astronomy)

Dr. Will Ansbacher, Departmental Member
(Department of Physics and Astronomy)
(British Columbia Cancer Agency- Vancouver Island Centre)

Dr. Alexandre Brolo, Outside Member
(Department of Chemistry)

Supervisory Committee

Dr. Andrew Jirasek, Supervisor
(Department of Physics and Astronomy)

Dr. Will Ansbacher, Departmental Member
(Department of Physics and Astronomy)
(British Columbia Cancer Agency- Vancouver Island Centre)

Dr. Alexandre Brolo, Outside Member
(Department of Chemistry)

ABSTRACT

Improvements to radiation therapy treatment outcomes rely, in part, on consideration of patient specific radiosensitivity. Therefore an assay which quantifies radiation-induced biochemical changes, and subsequently characterizes radiation responses in tumour and normal tissue is required. This work investigates the use of a single cell Raman spectroscopic technique to identify radiation-induced responses in human lung (H460), breast (MCF-7, MDA-MB-231) and prostate (LNCaP) cancer cell lines each selected to create a panel of cells varying in tissue of origin and radiation sensitivity. Cells were cultured *in vitro* and exposed to clinically relevant ($<$ 10 Gy) doses of radiation. Cell populations receiving 30 and 50 Gy were also studied in order to further elucidate dose-dependent trends and give additional information about the ability of Raman spectroscopy to identify radiation-induced biochemical changes occurring in the cell populations.

It was found that using Raman spectroscopy to identify a radiation-induced response in human cells cultured *in vitro* is governed by the subtlety of the radiation-induced response inherent to a specific cell line. Also the type of biochemical changes occurring in response to exposure to radiation will be dependent on the specific cell line. This work suggests that effective use of single cell Raman spectroscopy to monitor a patient's response to radiation early on in treatment (where the disease has been exposed to 10 Gy or less) is possible. However, a detailed knowledge of the biochemical changes associated with the unique radiation response for that particular disease is required.

Contents

List of Tables

List of Figures

ACKNOWLEDGEMENTS

Foremost, I would like to thank Michael for being a great companion, motivating and supporting me throughout my career and partaking in many fun and exciting adventures with me. Thank you for the countless fun memories we share and I look forward to those to come.

I also would like to thank Mom, Dad, Ian and Baba for always encouraging me to pursue my dreams. Your support has been a guiding light for me.

Thank you to Dr. Jennifer van Wijngaarden for introducing me to the exciting world of research in spectroscopy, and being a great role model.

Also, thank you to Dr. Quinn Matthews and Dr. Martin Isabelle for invaluable mentorship in both the Raman and biology labs. Thank you for assisting me in the lab and the many useful discussions involving running ideas off each other. I apologize for scheduling such early morning experiments!

Finally, I would like to thank Dr. Andrew Jirasek, Dr. Alexandre Brolo, Dr. Julian Lum and Dr. Will Ansbacher for providing me with helpful advice and interesting discussions.

DEDICATION

For Michael, Mom, Dad, Ian and Baba.

Chapter 1

Introduction

1.1 Radiation therapy

Cancer is a disease resulting from the lack of growth regulation in a cell. Any cell has the potential to become cancerous and as a result, this disease can present its self in a variety of locations and forms throughout the human body. Much like no one person is identical to another, each case of cancer is unique. Factors such as cell biology, clinical indicators and disease outcome will vary over a cohort of patients [1]. Historically speaking, physics has played an important role in the quest for control of this intricate disease and this role continues to be important today through the application of radiation for cancer diagnostics and therapeutics.

In cancer care, radiation therapy (RT) is the application of ionizing radiation to control malignant lesions. Because ionizing radiation will kill both healthy and cancerous cells in an unbiased fashion, the goal of RT is to deliver a uniform dose of radiation to the cancerous lesion, while minimizing dose to the surrounding healthy tissue [2]. Along with surgery and chemotherapy, RT is a cornerstone in treatment or palliation for many cancer patients. Surveillance, Epidemiology and End Results (SEER) data from between 2003-2005 indicated approximately 29% of cancer patients in the United States of America received RT during their initial treatment course [3]. Because of the significant role RT plays in cancer care, considerable research efforts into developing and improving this technique are pursued.

The contributions of physics in cancer care were initially in developing high energy (Mega Voltage, MV) particle accelerators to produced photons of sufficient energy to deliver a uniform dose within a patient. Initial limitations on x-ray production meant only photons of low energies (100-400 kV) could be produced, giving rise to applications in medical imaging and therapeutic applications which lead to non-uniform doses in deep seated lesions with high levels of bone and skin toxicity [4]. As advancements in accelerator physics progressed, x-rays of increasingly higher energies were produced and by the 1950's x-rays up to 8 MeV could be achieved using linear accelerator (LINAC) technology. During that time radioactive decay of Co-60 was also found to be a valuable high energy (1.25 MeV) therapeutic option and led to the invention of the Co-60 teletherapy unit. These sources of high energy x-rays reduced skin toxicity, and improved dose uniformity in the lesion [4]. As MV x-ray technology allowed for improved depth-dose distributions, the focus for advancement of RT became improving the delivery and shaping of the dose distribution.

Delivering dose distributions which are conformal to the lesion of interest has driven significant efforts from researchers to develop field shaping techniques. One of the first attempts at this was the isocentric rotation capabilites of the Co-60 teletherapy unit introduced in 1959 by Johns and Cunningham [5]. Starting in the 1950's delivery of radiation to a lesion using LINAC technology was achieved using conventional external beam RT where single rectangular or simply shaped fields are used. Conformal RT brought dose sculpting one step further by shaping the radiation field to better conform the dose distribution to the shape of the lesion [6]. Beginning in the mid 1960's concepts in three dimensional conformal RT (3D-CRT) were developed [4]. 3D-CRT extended conformal RT to three dimensions by shaping multiple fixed beams to form a highly conformal three-dimensional dose distribution [7]. Intensity modulated radiation therapy (IMRT) became a popular research topic in the 1990's and by the late 1990's became a commercially produced technology [8]. IMRT improved upon 3D-CRT by using field intensity modulations which have been optimized to achieve maximum dose to the lesion and minimal dose to healthy tissue [6]. The dose conformity achieved with IMRT gave way to unique dose delivery options leading to dose escalation and healthy tissue sparing relative to conventional techniques in sites such as: lung [9], head and neck [10] [11] and prostate [12] [13], to name a few. Current techniques in RT combine the field shaping achieved with IMRT together with simultaneous changes in dose rate, gantry arching and couch motion. This technology is referred to as volumetric modulated arc therapy (VMAT) and is designed to maximize conformal dose delivery capabilities obtained with IMRT, while improving treatment times [14].

While efforts to improve the physical delivery of a dose distribution are important in facilitating the necessary balance between tumour control and normal tissue toxicity, there is another aspect of RT which warrants significant attention. It is important to consider not only the accurate delivery of a radiation dose to a lesion but also the optimal dose quantity intended to be delivered and choice of therapy (radiation alone, radiation and chemotherapy, radiation and surgery). In order to ensure the optimal dose and treatment regimen is prescribed, it is important to address the considerations used to define these parameters.

1.2 Radiobiological considerations for radiation therapy

The decision to include RT in a specific treatment regimen is based on demonstrating the efficacy of RT in improving local tumour control, relieving symptoms or improving quality of life [15]. Once it is decided that RT will be included in a patient's treatment regimen a couple of important decisions must be made. First, the capacity in which RT will be involved must be determined. Combining radiation with chemotherapy has proven advantageous for some forms of cancer [16], however RT can also be applied in combination with surgery, or used on its own [17]. Secondly, the prescribed dose must be determined such that it balances between achieving tumour control while reducing normal tissue toxicity.

These treatment details are decided by consideration of factors predictive of therapy outcome such as tumour and patient clinical indicators, technicalities of the treatment and the dose response relationship between tumour control and normal tissue injury [15] [18] [19]. The latter factor can be dependent on both empirical understanding, research based knowledge and personal experience [15]. Figure 1.1 gives a detailed list of some commonly considered indicators. These predictive factors can be combined together to give the physician an estimate of the probability of tumour control for that patient [19], based on previous understanding of how a similar population of patients responded to treatment. However, there is no way of knowing prior to treatment whether or not the standard prescribed treatment will achieve tumour control while sufficiently avoiding normal tissue complication for that specific patient. This arises in part from the inherent variation between patients in radiosensitvity of both normal tissue and tumour [18] [20]. Therefore any one patient will respond uniquely, in terms of cure and complication, to a standard treatment. Given that

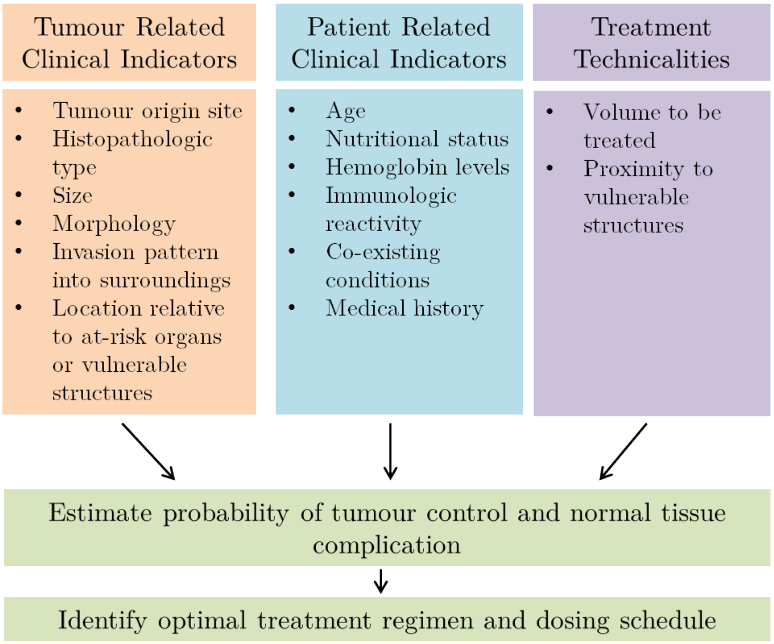

Figure 1.1: Detailed list of clinical indicators important for assessing appropriate application of radiation therapy for a given patient. Compiled from sources [15] [18] [19].

both tumour and healthy tissue response is patient specific, one may benefit from a personalized RT regimen. An objective assay for determining patient specific tumour and normal tissue radiation response is required and is currently the focus of much research.

1.3 Personalizing radiation therapy

Considerable efforts have been made in an attempt to identify a suitable predictive assay for radiosensitivity. These assays measure a cell based process or characteristic which is potentially linked to radiation response such as intrinsic radiosensitivity, oxygen tension or cell proliferation. Cell assays, functionality measurements, genetic surveys and molecular imaging have all been investigated as potential assays. Unfortunately, to date, no one assay has proven sufficient for clinical implementation.

1.3.1 Cell-based assays

Cell-based assays include measuring intrinsic cell radiosensitivity as characterized by counting the surviving fraction of cells after irradiation with 2 Gy (SF_2, discussed in detail in chapter 2 section 2.3.3. Also, see chapter 2, section 2.1.2 for definition of the unit Gy). This is a direct measure of cell response to radiation through observing the colony forming abilities of a specific cell line. SF_2 has been shown to be a significant prognostic factor in head and neck [21] and cervix [22] cancers. Unfortunately, such assays can be very time consuming (four weeks incubation), labor intensive (cell culturing, colony counting) [23] and have poor reproducibility because of the technical complexity of its methodology. The surviving fraction is a direct measure of colony formation and gives little insight into the underlying mechanisms driving radiation response. An alternative to direct measure of cell colony formation is through surrogates for cell radiosensitivity such as deoxyribonucleic acid (DNA) break and repair [24], chromosome aberrations [25] or apoptosis [26] (see chapter 2, section 2.3.2). Such measures of inherent radiosensitivity are less time consuming than colony assays however the surrogate technique is an imperfect measure of radiosensitivity [18].

1.3.2 Functional assays

Oxygen tension of tumour cells play an important role in sensitizing cells to radiation (see chapter 2, section 2.3.4), making the measure of hypoxia (both directly and indirectly) the basis of investigation into some radiosensitivity assays. Hypoxia levels can be measured directly through polarographic electrodes [27], or indirectly through endogenous hypoxic markers [28] [29]. Other indirect ways of measuring hypoxia are through tumour vasculature density, perfusion and tumour metabolic activity using functional imaging. Nordsmark et al. showed that head and neck patients with hypoxic tumours respond poorer to RT than those with well oxygenated tumours [30]. Unfortunately, direct measurements of hypoxia are invasive to the patient and indirect measures may require injection of a chemical tracer.

Cell proliferation rates can also be an indicator of cell radiosensitivity because of its effects on treatment outcome through tumour re-population (see chapter 2, section 2.3.4). This can be measured by counting the mitotic index (fraction of cells in mitosis), measuring tumour potential doubling time through thymidine analog uptake [31] or staining for proteins associated with proliferation (ex. Ki67) [32] [33]. Thymidine analong uptake is studied by injecting a thymidine species which preferentially accumulates in proliferating cells into the patient, and subsequently collecting a tumour biopsy for analysis. Such studies have shown significant trends correlating high labeling index (a measure of proliferation rate) with poor local control, although this result has limited implications [31]. The techniques associated with determining cell proliferation rates are also limited because thymidine uptake studies require injection of a drug/tracer making it invasive for the patient, and common protein labeling assays give little information on the involved radiation response mechanisms.

1.3.3 Genome-wide assays

In recent years there has been a considerable shift in research efforts towards genomic based assays. Gene expression associated with a radiation response mechanism (ex. hypoxia or proliferation) can be used to identify signatures of response. For example, Khodarev et al. showed that Signal Transducer and Activator of Transcription-1 (STAT1) may be linked to increased tumour survival following exposure to ionizing radiation [34]. However, the predictive power of this pathway has not been tested clinically.

Another extensively investigated gene is p53, which has been studied as a biomarker for radiation response for a variety of tumour origin sites (ex. central nervous system, bladder, ovarian, colon, prostate) [35] [36] [37] [38] [39]. McIlwrath et al. looked at carcinomas originating in brain, bladder and ovary and concluded that wild-type p53 gene status is required for cell sensitivity to radiation, however the presence of this gene does not necessarily predict radiation sensitivity because other radiation response mechanisms can annul its function [35]. Slichenmeyer et al. looked at colorectal carcinoma and suggested that loss of p53 gene function has no effect on cell radiosensitivity [36]. Scott et al. found that functional p53 gene in prostate carcinoma is related to significantly increased clonogen survival [37]. Although extensively studied, the potency of p53 gene status for determining patient response to radiation has yet to be verified through clinical trial. p53 gene status alone as a predictor of radiation sensitivity may be insufficient because its implications seem to vary with tissue of origin, suggesting that a collection of genes or other factors (clinical indicators) should be used in combination to adequately capture the complexity of radiation response in tumours.

A move to genome-wide assays eliminates the narrow scope associated with single gene assays, because many biological processes can be monitored simultaneously with no bias as to which genes should be studied. Torres et al. have devised a gene expression classifier to identify a series of genes from a panel of established cell lines, which successfully predicted radiation sensitivity in 22 of 35 established cell lines [40]. This classification algorithm was then extended to identify radiation-specific biomarkers by integrating gene expression information with biological variables like tissue of origin and p53 gene status [41]. This gene set was applied to independent cohorts of patients with either rectal, esophageal, breast or head and neck cancer treated with concurrent chemoradiation and proved to carry significant predictive power [42] [43]. Despite these advances, such techniques have not been clinically implemented for several reasons. The clinical validation of the gene set reported inaccuracies in the prediction due to false negatives [42]. Also some biases in the model used to generate the gene set can be identified; the classification algorithm favored well-studied genes, the gene set is determined based on a limited panel of established cell lines and there is an absence of known tumour micro-environment related genes (ex. hypoxia). Further testing, in a larger and more modern cohort of patients is required in order to assert its clinical use.

1.3.4 Molecular imaging

Molecular imaging techniques can also be used for radiosensitivity assays. These imaging methods include positron emission tomography (PET), magnetic resonance (MR) and optical imaging techniques like fluorescence imaging. Such techniques facilitate imaging of the entire tumour which addresses selection problems associated with biopsy-based techniques, since a biopsy is a section of a heterogeneous tumour [44]. These techniques provide spatial information and in some cases can provide dynamic imaging options. Imaging methods can be designed to study characteristics of the tumour linked to radiation response like hypoxia [45] (measures of oxygen uptake or surrogates for hypoxia like perfusion [46] and angiogenesis [47]), cell proliferation [48], apoptosis [49], receptors or gene expression [50]. Unfortunately, these techniques can involve injection of toxic or radioactive agents, making them invasive to the patient. Clinical studies investigating molecular imaging as a radiation response assay have shown some promise [46] [47] [51] [52], however, further clinical validation in large controlled studies is required.

1.3.5 New innovations in radiosensitivity assays

Genetic-wide assays and molecular imaging techniques hold potential as clinically implemented radiosensitivity assays. However, new assays which can augment these techniques or alleviate the draw backs associated with them are required. A clinically implemented radiosensitivity assay should be an *in vitro* or *in vivo* technique which: can be performed rapidly relative to the time line of a patient's treatment process, is cost effective, is reproducible, is insensitive to tumour sampling, is non-invasive, has high specificity and sensitivity to identifying changes in radiosensitivity and correlates directly to local tumour control [18] [19]. Finally, an assay which can measure biochemical signatures of radiation response would facilitate further understanding of the mechanisms of radiation response. This capability could provide mechanistic information that could be used to enhance treatment and determine the optimal treatment for a patient.

1.4 Raman spectroscopy as a radiosensitivity assay

Raman spectroscopy (RS) offers a label-free way of obtaining an objective and quantitative measure of the molecular content of a sample. Raman scattering arises when monochromatic light incident on a sample is inelastically scattered, inducing transitions to vibrationally excited normal modes in molecules present in the interacting sample. Physical bond properties of these molecules will determine the energies of the available normal modes, and therefore the energy shifts in the scattered photons. The type and quantity of vibrational excitations induced in a sample are measured by detecting these scattered photons and counting the number of photons of a particular scattering energy (see chapter 3), resulting in a unique Raman spectrum based on the molecular content of the sample.

1.4.1 Raman spectra of biological samples

RS can reveal detailed information about the chemical content of a sample and the physical bonds making up these molecules. To date, RS has been applied to study biological materials by looking at biomolecule characteristics in: solution, individual live cells, tissue.

RS has been used to determine secondary structure and side chain chemical environment in proteins [53], determine chromatin structure [54], distinguish DNA structure types, study characteristics of DNA/ribonucleic acid (RNA) [55] or DNA/protein hybrid structures [56] as well as nucleic acids and membranes (protein/lipid assemblies). See Fabian et al. for a concise review of these applications [55]. RS has also been established as an effective technique for studying human cells. Puppels et al. demonstrated the use of RS to study the biomolecular content of individual human cells in cytoplasmic and nuclear regions [57] and showed that Raman is sensitive to content differences between the two regions of the cell. They then showed that RS was capable of measuring spectral differences between neutrophilic, eosinophilic and basophilic cells [58]. Other studies have applied RS to monitor cell functions like cell cycle [59], proliferation [60] and cell death [59] [61]. RS has also been used to study tissue composition changes arising from factors like disease (ex. cancer [62] or Alzheimers [63] [64]) and tissue structure changes (ex. muscle contraction [65] [66]).

In addition to the wealth of biochemical information that can be obtained, RS is advantageous for collecting spectra of biological materials because it can be non-destructive to live cells or tissues. With the appropriate instrumentation, RS can be applied to cells or tissue *in vitro*, *ex vivo* or *in vivo* in a label-free manner. Selection of instrumentation can also give Raman systems that are capable of probing sample sizes less than 10 μm (along all three spatial dimensions), giving spatial resolutions below the typical size of a cell [57] [67]. Also, with the appropriate detector, laser power and system efficiency, a single Raman spectrum with acceptable signal-to-noise ratio can be collected in seconds. These advantages make RS an ideal technique for studying live tissue and cells for medical purposes.

1.4.2 Applications of Raman spectroscopy in cancer care

Raman spectroscopy in cancer diagnosis

The motivation for using RS in cancer diagnosis is that it is expected cancer leads to changes in the molecular composition of the diseased tissue, which should be reflected in the spectra [68]. Research using *ex vivo* biopsies have demonstrated the ability of RS to differentiate between healthy and cancerous tissue in a variety of sites including brain [69], breast [70] [71], cervix/gynecological tract [72] [73], colon [74] [75] [76], bladder [75], head and neck [77] [78] and prostate [77]. Improvements to fiber optic probes has opened up the opportunity to collect *in vivo* Raman measurements, meaning Raman could be applied during biopsy or surgery to direct therapeutic intervention in an objective manner [79]. Several researchers have demonstrated the use of a fiber optic probe to collect Raman spectra *in vivo*, and effectively differentiate healthy from basal cell/squamous cell carcinomas [80] as well as breast [70], colon [76] and cervix [81] carcinoma. Nijssen et al. have performed an *in vitro* study which suggests RS can be used as an objective technique for tumour border demarcation in basal cell carcinoma [82]. Furthermore, if molecular composition differences are specific enough to a certain stage of disease, RS could also be used for grading disease. Mahadevan-Jansen et al. have demonstrated the use of RS to differentiate between metaplasia, inflammation, normal tissue, and low and high grade cervical pre-cancers [83]. Additionally, Crow et al. have demonstrated the ability to use RS to differentiate between different grades of prostate carcinoma [84].

Raman spectroscopy in radiobiology

The wealth of structural and chemical information obtained with RS has made this technique appealing for studying the effects of ionizing radiation on biological materials. Spectral differences between irradiated and unirradiated DNA solutions have been observed using RS [85] [86] [87], and have been attributed to structural changes in the DNA as a result of radiation damage. Furthermore, a dose-dependent denaturation of bovine and human serum albumin (an abundant plasma protein in mammals) was observed with RS [88]. Work by Torreggiani et al. has demonstrated the use of RS to identify radiation-induced changes in protein structure [89] and radiation was shown to cause conformal changes in the lipid chains of artificial lipid membranes using Fourier Transform RS [90]. RS has also been used to study the role of the cell membrane in radiation-induced cell death by: studying the effect of lipid phase state on lipid membrane radiation sensitivity [91], studying the effect of radiation on liposomes in the presence of proteins [92] and using RS to identify radiation-induced changes in plasma membranes isolated from hamster cells [93]. Synytsya et al. detected gamma and proton radiation-induced destruction of primary structure, functional group loss and cross-linking in sodium hyaluronate (a chief component of the extracellular matrix and present in connective, epithelial and neural tissues) [94].

RS has also been applied to study the effects of proton radiation on mammalian tissues. Synytsya et al. show that RS is suitable for identifying proton radiation-induced damage to normal and tumourous human tissue, mainly in the form of protein damage, and their results suggested human tumour tissue is more radiosensitive than normal human tissue based on the extent of radiation-induced damage observed [95]. Lakshmi et al. have demonstrated radiation-induced differences, mainly in protein content, between unirradiated mouse brain tissue and tissue irradiated to 10 Gy of gamma radiation, *in vivo*. Their work also identified spectral differences between the irradiated and unirradiated populations in tissue distant from the irradiation site (leg muscle), supporting the hypothesis that protective factors are released throughout the body when the central nervous system is exposed to radiation [96]. Vidyasagar et al. successfully identified minor but significant differences between responding and non-responding cervical tissue, post irradiation (to 4.5 Gy x-rays) [97]. This result demonstrates the potential of RS for clinical applications in monitoring radiation response, however the author offers no description of the biochemical differences motivating differentiation between responding and non-responding samples.

Tissue is a composition of cells and varying levels of extracellular matrix or basement membrane (in epithelial tissue) constituents [98]. Although the Raman spectral features arising from this collection of materials can be useful for applications of RS in diagnosis or radiobiology [99], cell function its self forms the basis of tissue function [74]. RS on single living cells will eliminate potentially confounding information from other material in the tissue, and has the potential to offer valuable information on the biochemical mechanisms fueling cell-specific activity. In the case of radiobiology; a biochemical snapshot of a collection of single living cells responding to radiation would be valuable for elucidating the radiation response mechanisms in these cells. In obtaining the clearest possible picture of cell response to radiation, a way of classifying this response could potentially emerge.

To date, radiation responses in single cells have been studied in a variety of human lung, prostate and breast cancer cell lines, *in vitro*, following a relatively high x-ray dose of 50 Gy [67] [100]. This work demonstrated the use of RS in combination with principal component analysis (PCA) to identify spectral features which appear to be correlated with dose. Furthermore, comparison of the cell lines observed suggested the dose-dependent spectral features segregate with p53 gene status and intrinsic radiosensitivity [100]. These results illustrate the potential of RS in further understanding the driving mechanisms behind variations in both tumour and normal tissue radiation sensitivity between patients, and potential to apply RS as a radiosensitivity predictive assay to monitor patient response during treatment. While promising, clinical practice will limit the dose delivered to the cells being studied, thus requiring

RS to be sensitive to biochemical changes in cells following dose levels much less than 50 Gy.

A predictive assay to monitor tumour response or normal tissue response during treatment will be most beneficial within the first few fractions of treatment. Conventional total doses for curative RT are on the order of 40-70 Gy (in 2 Gy fractions) [101]. Sensitivity of RS to biochemical changes indicative of radiation response at earlier time points in treatment (and hence lower doses of around 4-8 Gy) would lead to the possibility of adjusting a patient's treatment (total dose or fractionation schedule) to compensate for their individual response to radiation. Therefore, the capability of RS to detect radiation-induced biochemical changes in single cells for doses well below 50 Gy must be determined.

1.5 Thesis scope

The goal of this work is to investigate the use of a single cell Raman spectroscopic technique to identify radiation-induced responses in human cancer cell lines, cultured *in vitro*, following irradiation with doses typical of early time points in a RT treatment regimen. RS is used in combination with PCA to identify radiation-induced responses in a panel of four human cancer cell lines varying in tissue of origin, intrinsic radiation sensitivity (SF_2) and p53 gene status. This is done by collecting Raman spectra and applying PCA to study biochemical changes occurring in cell populations from each of the four lines exposed to single radiation doses ranging from 0-10 Gy. Cell populations receiving 30 and 50 Gy are also studied in order to further elucidate dose-dependent trends and give additional information about the ability of RS to identify radiation-induced biochemical changes occurring in the cell populations. The application of RS to identify radiation-induced biochemical changes in cells is presented separately for each cell line. Common trends between cell lines are discussed and implications of these results and possible biological mechanisms which could result in the observed biochemical changes are also discussed. The feasibility to identify biochemical changes for doses below 10 Gy (representative of early time points during a patients treatment, section 1.4.2) for each of the four cell lines is also addressed.

First an overview of the basic knowledge of RT, cell biology, radiobiology and theoretical ways of describing microscopic and macroscopic response of cells to radiation are explored in chapter 2. Chapter 3 gives a detailed overview of the theoretical aspects and instrumentation important for RS with concentration on application to studying biological materials. Chapter 4 discusses details on the materials and methods used to carry out the work presented in this thesis.

The results of this thesis are presented in a series of four chapters; one per cell line. Chapter 5 presents Raman data for the H460 cell line and discusses the observed biochemical changes arising from both cell cycle and radiation response heterogeneity between populations. Chapter 6 presents data for the MCF-7 cell line and discusses the observed biochemical changes arising from cell cycle and radiation response heterogeneity between populations for this cell line. A discussion about the relationship between the observed biochemical changes in the MCF-7 and H460 cell lines is offered. Chapter 7 presents data for the MDA-MB-231 cell line and discusses both cell cycle and radiation-induced biochemical changes in the populations studied. Application of single cell RS for identifying radiation-induced biochemical changes in cells in a subtly responding cell line are discussed. Chapter 8 presents results illustrating cell cycle and dose-dependent biochemical changes in the LNCaP cell line. A discussion regarding common trends in dose-dependent biochemical changes between the MCF-7, MDA-MB-231 and LNCaP cell lines, as well as implications for using single cell RS to identify radiation-induced biochemical changes in a variety of cell lines is presented.

This work is concluded by highlighting the main conclusions drawn from the four Raman studies and the implications of these results for using a single cell Raman spectroscopic technique to identify radiation-induced responses in human cancer cell lines, cultured *in vitro*, following irradiation with clinically relevant levels of radiation are discussed. Appendices A, B and C offer supporting biological experiment results (cell cycle distributions, total cell counts and viability) for the experiments presented in this thesis. Finally, appendix D presents Raman data which were part of the data sets presented but were not discussed explicitly in this thesis.

Chapter 2

Radiation Therapy and Radiation Biology

This chapter introduces fundamental background knowledge on RT and radiation interactions with matter. Section 2.1 discusses the various forms of RT for the treatment of cancer, a detailed description of the mechanics of a LINAC and a description of the physical processes resulting in dose deposition in tissue. Section 2.2 introduces the biomolecules responsible for driving cell and tissue function and the cell cycle. Lastly, section 2.3 combines the two preceding sections to discuss the effects of radiation on cells and biological systems by addressing the various forms of radiation-induced cell damage and the cell's subsequent response mechanisms. Macroscopic descriptions of cell and tissue response to radiation are also discussed.

2.1 Radiation therapy physics

The RT process starts by using imaging techniques (ex. CT, PET or MRI) to locate the site of macroscopic disease within the patient. Motion, patient setup errors and microscopic spread of disease are accounted for by the addition of a margin around the macroscopic disease, forming the treatment volume. A specific radiation dose is then prescribed by the physician, and the accurate and conformal delivery of the radiation dose becomes priority. In modern cancer clinics, treatment modalities such as brachytherapy and external beam RT (EBRT) are most commonly used to deliver radiation to the treatment volume.

EBRT makes use of a high energy (MV) photon beam located external to the patient and conformal dose delivery techniques (such as 3DCRT or IMRT as discussed in chapter 1, section 1.1) to deliver the required dose to the treatment site. EBRT can be used as a treatment option in conjunction with surgery as is common for treatment of bladder and breast carcinomas or in conjunction with brachytherapy as is common for treating cervix and prostate carcinoma [102]. The radiation source in EBRT is produced by accelerating charged particles to create a relatively homogeneous radiation field.

2.1.1 The linear accelerator

The clinical LINAC offers versatility in treatment delivery techniques and as a result has become a widely used treatment option for EBRT in modern clinics [103]. Both electron and photon beams can be produced using a LINAC, however only photon mode will be discussed here. A scheme of a clinical LINAC is shown in Figure 2.1. First, power is supplied to a modulator which emits high voltage pulses simultaneously to an electron gun and magnetron or klystron. The magnetron or klystron produces an electromagnetic wave which is propagated through a linear accelerator structure, creating a magnetic field. At the same time, the modulator pulse heats up a wire filament in the electron gun which allows electrons, at an initial energy of about 50 keV [104], to be injected into the linear accelerating structure by thermionic emission. The electromagnetic field present in the structure causes the electrons to accelerate to energies between 4-25 MeV. Using bending magnets, the accelerated electrons are bent (90 or 270 degrees), towards a high atomic mass material (ex. tungsten) target.

In the target, high energy electrons undergo inelastic collisions through interactions with the Coulombic field of the atoms causing the electrons to decelerate and emit bremsstrahlung photons. For a MV photon beam, the bremsstrahlung photons are forward directed and approximately continue along the direction of travel of the electrons. A narrow continuous energy photon beam with energies ranging from approximately 100 keV to the maximum (4-25 MeV) accelerated electron energy emerges and continues through the treatment head towards the patient. In the treatment head the photon beam passes through a variety of collimation and radiation field shaping devices resulting in a custom shaped radiation field directed towards a pre-planned target site on a strategically placed, immobilized patient. The LINAC is designed to have an axis of rotation centred around isocentre as indicated in Figure 2.1. The distance from the target to the isocentre is referred to as the source-axis-distance

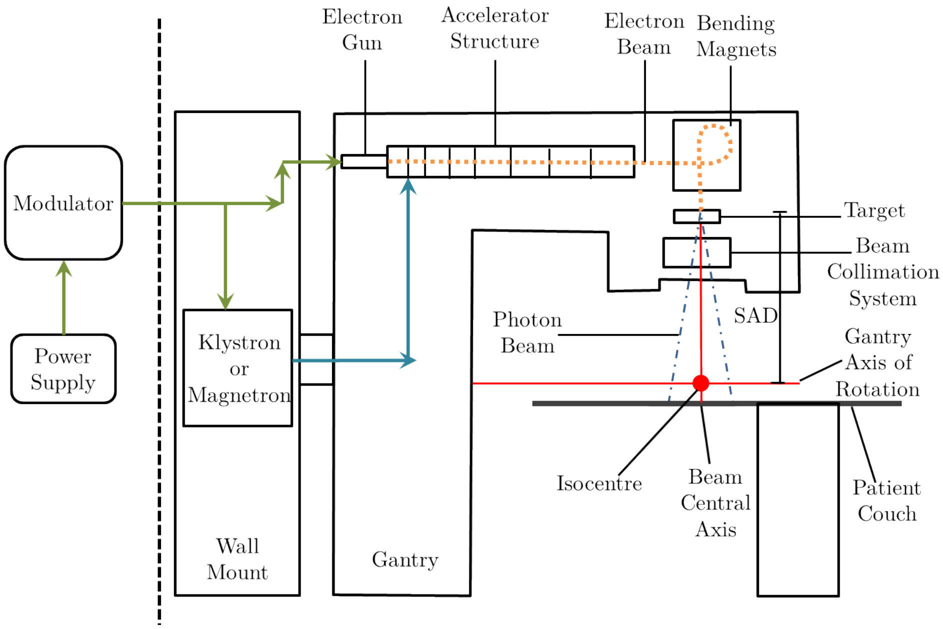

Figure 2.1: Schematic of a clinical linear accelerator (LINAC). The source-to-axis distance (SAD) is typically set to 100 cm and measures the distance from the target to the LINAC's isocentre.

(SAD) and is commonly set at 100.0 cm.

2.1.2 Interactions of radiation with tissue

Photons emerging from the LINAC treatment head mostly interact with tissue within a patient. Tissue is composed of 73% oxygen and 10% hydrogen by weight, making its radiation interaction properties very similar to water (89% oxygen and 11% hydrogen by weight) [105]. Photons with energies common for a clinical LINAC (100 keV to maximum accelerated energy of electrons) predominantly interact through photoelectric, coherent scattering, incoherent scattering and pair production interactions. The proportion of each type of interaction which occurs is dependent on photon energy. While coherent scattering does occur for photons in this energy range, it is an elastic scattering event and therefore does not contribute to dose deposition in the interacting medium.

Photoelectric effect

The photoelectric effect is the interaction of a photon with a bound orbital electron of an atom in the interacting medium. The photon energy is completely absorbed by the orbital electron, and the photoelectron is ejected from the atom with a kinetic energy equal to the energy of the photon minus the binding energy of the orbital electron. Photoelectric interactions dominate for photon energies lower than 20 keV in water [106].

As a photoelectron is ejected from the interacting atom, the atom assumes an unstable excited state. The atomic vacancy will rapidly be replaced with an outer electron to bring the atom back to a stable state. As the outer electron replaces the inner orbital vacancy a characteristic photon equal to the difference in energy between the outer and inner orbitals will be released. This characteristic photon can then leave the atom and continue through the interacting medium for further potential interaction, or interact with another bound orbital electron in the same atom ejecting it from the atom. This electron is referred to as an Auger electron and can continue interacting in the medium.

Incoherent scattering

Incoherent scattering (Compton scattering) is the scatter of a photon off a loosely bound orbital electron of an atom in the interacting medium. The incident photon transfers a portion of its energy to the electron, resulting in an ejected electron with kinetic energy equal to the difference between the initial and scattered photon energy. This scattered photon has the potential to further interact in the medium. Much like in the photoelectric effect the ejected electron creates an unstable excited atom which becomes stable by emission of characteristic radiation or an Auger electron. Incoherent scattering dominates for photon energies between 20 keV and 20 MeV in water [106].

Pair and triplet production

Pair production can only occur for photons with an energy greater than 1.022 MeV. Pair production is the complete transfer of photon momentum (and therefore complete absorption of the photon) to an electron-positron pair in the presence of the Coulombic field of an interacting atomic nucleus, with excess photon momentum transferred to the nucleus. The nucleus (whose mass is large relative to the momentum transferred) simply absorbs this energy and only two particles leave the interaction; an electron-positron pair.

Triplet production is the complete transfer of photon momentum to an electron-positron pair in the presence of the Coulombic field of an orbital electron, and simultaneous transfer of excess photon momentum to the electron. This interaction can only occur for photons with energies greater than 2.044 MeV. The electron (whose mass is not large relative to momentum transfer) is ejected from the interaction site with finite kinetic energy. Therefore, three particles leave the interaction site; the electron-positron pair and the ejected orbital electron. For photon energies around 5 MeV, in water, the triplet production cross section is only 5-10% of the pair production cross section, making pair production the dominant interaction type between the two [107]. Pair production and triplet production are the dominant form of photon interaction for energies greater than 20 MeV in water [106].

Dose deposition

Photons are classified as indirectly ionizing radiation, meaning a photon deposits energy in a material by first interacting with the atoms of the material to release electrons, which are directly ionizing radiation and so directly deposit energy into the medium. Of the photon-matter interactions just mentioned, energetic electrons are released into the medium through photoelectric, incoherent scatter, pair or triplet production and the Auger effect. These electrons propagate through the medium and interact by (a) inelastic collisions with atomic electrons (ionization or excitation), (b) inelastic collisions with nuclei (bremsstrahlung), (c) elastic collisions with atomic electrons and (d) elastic collisions with nuclei. Inelastic collisions result in energy loss by the electron, and therefore energy transfer to the medium (as is the case for type (a) interactions) or into photon energy which can then propagate through the medium as previously discussed (as is the case for type (b) interactions). Elastic collisions cause no loss in kinetic energy by the electrons. In water, the dominant energy loss mechanism is through ionizing events with atomic electrons [107]. These electrons will continually lose energy as they travel through the medium until they reach thermal energies, after which they will be captured by surrounding atoms.

Positrons created in pair and triplet production will interact with the medium through collisional and radiative interactions, similar to that for the electron. After the positron loses its kinetic energy it will annihilate with an orbital electron in the interacting medium, resulting in the creation of two photons each with energy of 0.511 MeV emitted in opposite directions relative to one another. These photons then continue to propagate through the medium as previously discussed.

Energy absorbed by the interacting medium through electron (or positron) interactions is what gives rise to dose deposition by the photon beam in the medium. Dose is measured in units of Gray (Gy), and can be thought of as the amount of energy transferred per kg of interacting material (1 Gy=1 J/kg). This deposited energy has the potential to cause molecular damage which, in the case of live tissue, can lead to biological damage.

2.2 Cell characteristics and processes

Tissues are the building blocks for organs which drive the functions necessary for sustaining human life. Tissues are composed of collections of cells which all possess similar functions and characteristics, meaning the individual cells of a tissue represent the general qualities of that tissue. The quality and quantity of various cellular constituents will vary between cells from different tissues, based on the function of that given tissue. For example, gangliosides are large complex lipids which play a role in the specific function of ganglion cells, spleen cells and erythrocytes and therefore are only found in these cells [108]. While cell and tissue function will determine some of the specific chemical content in cells, general similarities exist between all mammalian cells.

Section 2.2.1 describes the components which make up a typical mammalian cell. Those biomolecules which are commonly involved in driving the function of these cellular components are also discussed. An important cellular processes that relies and affects the balance of these biomolecules is the cell cycle, as discussed in section 2.2.2.

2.2.1 The building blocks of cells: biomolecules

The human cell is composed of an outer cell membrane enclosing a nucleus and cytoplasm, containing a variety of organelles. Cells are chiefly composed of water, as it makes up about 75% of a cells total mass [108]. In addition to water, the human cell is made up of approximately 1% inorganic constituents [108] and the remaining is a complex collection of organic constituents including several important biomolecules:

protein (15% of the cell content), nucleic acid (1%), carbohydrates (1%) and lipids (2%) [109]. These materials are the main building blocks of the structures making up the cell, and drive cellular function.

The cell membrane contains the cell from its surroundings and controls what can enter or leave the cell. The cell membrane is 40-50% lipid, 50-60% protein and can be rich in enzymes [108]. The nucleus contains the cell's DNA and is surrounded by a two-layer membrane separating it from the rest of the cytoplasm but contains pores which allow exchange of proteins or other substances. The nucleus contains a large amount of nucleoprotein consisting of 50% DNA and 50% protein. The nucleus also contains some RNA, enzymes, free amino acids, lipids, calcium, magnesium and potassium as well as chromatin [108]. The nucleolus is also located in the nucleus and is a small dense structure which contains 10-20% of the RNA for the entire cell [108]. The cytoplasm is the fluid in which the organelles are suspended. It is an aqueous solution of proteins, RNA, glucose (a cellular metabolite), cellular waste products, enzymes and electrolytes. The organelles include the mitochondria (cellular metabolism), endoplasmic reticulum (synthesis of steroids, phospholipids and complex polysaccharides), ribosomes (protein synthesis), golgi apparatus (protein storage) and lysosomes (contain enzymes for autolysis of cell contents). On the macroscopic level, the combined action of these subunits yields cell function, however it is the microscopic dynamics of the biomolecules making up these cellular subunits which ultimately drives chemical processes and, therefore, function of the cell.

Nucleic acids

Nucleic acids are of two forms in the human cell; DNA and RNA. They are polymers made up of nucleotide (nitrogenous base- pentose sugar- phosphate group) monomers, as shown in Figure 2.2. In the case of DNA the monomer has the form:

$$\text{DNA}=(\text{base-deoxyribose-phosphate})_n$$

and in the case of RNA:

$$\text{RNA}=(\text{base-ribose-phosphate})_n$$

In both cases the monomers are linked through a $3'$, $5'$-phosphodiester bond. In DNA the possible nitrogenous bases are adenine, guanine, cytosine and thymine and in RNA uracil replaces thymine. The precise ordering of the bases in the nucleic acid

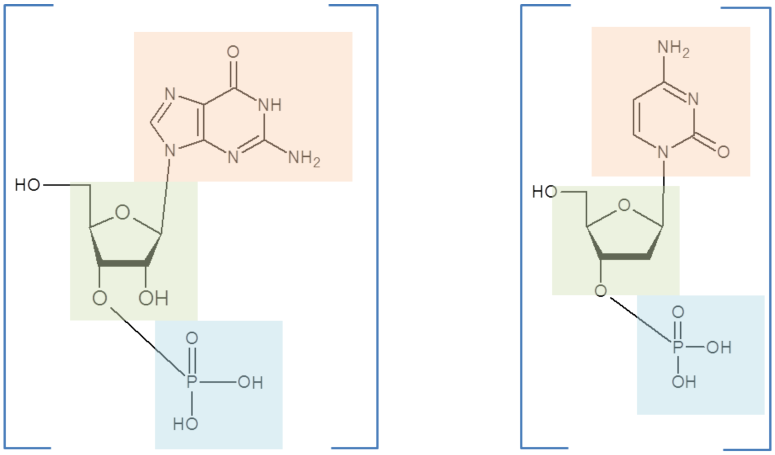

(a)

(b)

Figure 2.2: Monomer units for (a) RNA containing a guanine base and (b) DNA containing a cytosine base. The base is highlighted in orange, the phosphate in blue and the sugar (deoxyribose for DNA and ribose for RNA) is shown in green.

molecule describes its primary structure and contributes to its function and physical properties.

DNA is primarily located in the cell nucleus and is stored in compact entities called chromosomes. The chromosomes are made up of a seres of genes and each gene contains a finite segment of DNA characterized by a specific sequence of bases. DNA is composed of two polynucleotide chains which are wound about each other in a double helix conformation such that the bases are complimentary to one another. The two chains maintain stable contact through either double (A-T) or triple (G-C) hydrogen bonds between the complimentary bases. In unwinding the DNA structure the molecule forms a ladder-like appearance with the sides of the ladder made of the sugar-phosphate backbone and the rungs of the ladder the complimentary bases interacting through hydrogen bonds, as shown in Figure 2.3a. Unlike DNA, the majority of RNA exists in a single-strand formation as shown in Figure 2.3b.

DNA is responsible for directing cell activity and passing on genetic information from one cell to the next. This information is stored and regulated by DNA through the ordering of base pairs on the DNA molecule. Information stored in the DNA is put into action through transcription of the DNA base ordering to yield messenger RNA (mRNA) in a process called DNA transcription. mRNA then leaves the nucleus and travels to the ribosomes where the mRNA base sequence is used as a template to form proteins. The specific sequencing of the bases in the mRNA dictates the type and ordering of amino acids to be polymerized to yield a protein. These proteins then go on to carry out a variety of different biological functions. Nucleic acids are the basis of protein synthesis, which gives rise to biological function in the cell, tissues and organs.

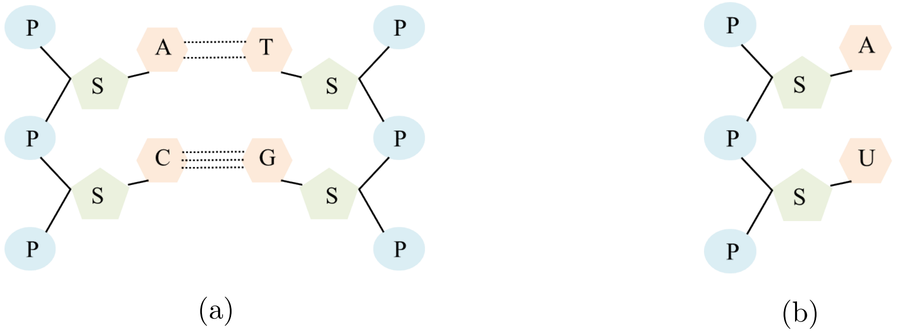

Figure 2.3: A simplified section of (a) double-stranded DNA composed of a phosphate (P), deoxyribose sugar (S) backbone connected together through hydrogen bonding between complimentary bases adenine (A) and thymine (T), cytosine (C) and guanine (G). A simplified section of (b) single stranded RNA composed of a phosphate (P), ribose sugar (S) backbone with bases attached to the sugar, and uracil (U) in place of thymine.

Proteins

Proteins are essential to cell and tissue function. They are important structural components (ex. membranes, nucleoproteins) and are invaluable for functional processes like maintaining fluid balance (serum albumin), regulation of metabolism (hormones or enzymes) as well as cellular transport and defense mechanisms. Proteins are high molecular weight polymers composed of α-amino acid subunits bonded together with peptide bonds forming a polypeptide chain. The types of amino acids forming the protein will have a significant impact on the physical, chemical and biological properties of the protein. The linear sequence of amino acids making up the polypeptide chain is referred to as the primary structure of the protein. Arrangement of the polypeptide chain in either helical, pleated sheet or random coils is described as the secondary structure. Tertiary structure is the final three-dimensional interaction of the helixes, sheets and coils. Lastly, the quaternary structure is the aggregation of various proteins to make up a functioning unit. Three-dimensional structure of a protein also plays a significant role in the functionality of the biomolecule.

Lipids

Lipids are an important source of energy and an essential component in cell and organelle membranes. Lipids are a group of molecules possessing three characteristics: 1) insoluble in water but soluble in organic solvents, 2) actual or potential to be an ester of fatty acids and 3) have the potential to be used by a living organism. Simple lipids are considered those lipids which are esters of fatty acids with alcohols. Some examples include triglycerides which are triesters of fatty acids with glycerol, or cholesterol esters which are fatty acid esters with cholesterol. Compound lipids are fatty acid esters with alcohols and other groups. Lastly, derived lipids stem from hydrolysis of either a simple or compound lipid and still possess the characteristics of a lipid. Some examples include saturated and unsaturated fatty acids, mono and di-glycerides, sterols, carotenoids and vitamins E and K.

Carbohydrates

Carbohydrates play an important role as an energy source (ex. glycogen or glucose). The resulting glucose metabolites supply the necessary precursors for synthesis of biological substances such as purines, pyrimidines, amino acids, cholesterol, mucopolysaccharides (ex. hyaluronic acid), fatty acids, glycoproteins and glycolipids. A carbohydrate is composed of carbon, oxygen and hydrogen and can be defined as polyhydroxyl ($^{-}$OH) alcohols with aldehyde or ketone groups. They are classified as basic monosaccharides (simple sugars), oligiosaccharides (composed of a few monosaccharides) or polysaccharides which are formed by polymerization of one (homo-) or several (hetero-) types of monosaccharides.

2.2.2 Cell cycle

The specific contents of a cell at any given time will be dependent on the type and function of that cell. However common cellular processes, such as cell cycle progression also alter the quantity and types of biomolecules present in the cell. The cell cycle describes the series of events leading to cell division and production of two identical daughter cells which are exact copies of a parent cell. The cell cycle consists of interphase and mitosis as shown in Figure 2.4. Interphase is the longest phase of the cell cycle, occupying approximately 90% of the entire cycle [110]. Interphase is divided into three parts: gap 1 (G1), DNA synthesis (S) and gap 2 (G2). In G1 no DNA replication occurs however the cell grows by way of increased RNA and protein content in preparation for DNA replication [111] [112]. Following G1, the cell enters S phase where DNA synthesis results in formation of two new DNA strands identical to the parent DNA. S is characterized by increased RNA, protein and DNA content relative to G1 [112]. The cell then enters G2 where it continues growth and preparation for cell replication by further increasing RNA and protein content [112]. Following interphase, the cell enters the relatively rapid mitosis phase in which the parent cell cleaves into two separate daughter cells, each containing a full compliment of the parent cell's DNA and approximately half of the biological content of the parent cell [109]. A cell can also suspend progression through the cell cycle and enter into gap 0 (G0) phase. Here the cell stays in a quiescent state with a relatively low level of RNA and protein content [111] [113], but retains its dividing capabilities. Most cells entering G0 do so during G1 phase and re-enter the cell cycle at S phase [114].

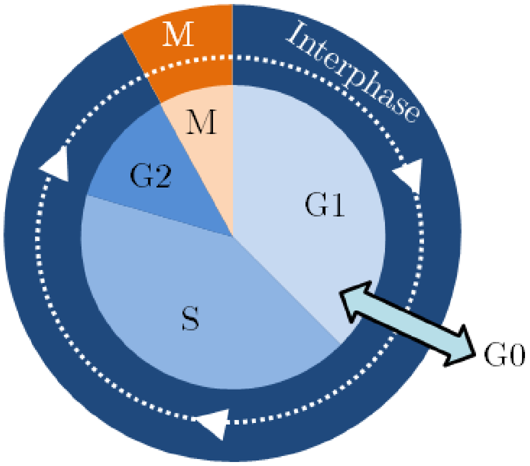

Figure 2.4: Phases of the cell cycle. The relative time spent in each phase is reflected in the size distribution for gap 1 (G1), DNA synthesis (S) and gap 2 (G2) in interphase, as well as mitosis (M). Cells can also enter a non-mitotic state of cellular quiescence (G0).

A dividing human cell typically progresses through the full cell cycle in approximately 24 hours [114]. Mitosis is the most rapid cell cycle phase, lasting around 1 hour. S phase lasts up to approximately 15 hours and G2 lasts for between 1-5 hours [109]. The remaining time is spent in G1 (approximately 8 hours), however the largest variation in temporal progression between cells comes in at this phase [109].

2.3 Radiation biology

The function of a cell and the biological system it belongs to relies on a delicate balance of biochemicals. A disturbance to the quantity or quality of these biochemicals can alter function of both the cell and the biological system it contributes to. In RT, ionizing radiation deposits energy through ionization and excitation interactions with the biochemical constituents of the cells in a specific location within a patient. Such interactions result in damage to the chemical structure of individual molecules, affecting the chemical and physical properties of those molecules, ultimately leading to altered biological function in the cell and the over arching biological system that cell supports. In this section the various forms of radiation-induced damage in cells will be discussed (section 2.3.1), as well as the cellular response to this damage (section 2.3.2) and methods for characterizing and modeling the effect of radiation on biological systems (section 2.3.3).

2.3.1 Radiation interactions in cells

As discussed in section 2.1.2, a photon beam releases electrons into the interacting medium and these electrons deposit energy through ionization and excitation of the atoms and molecules present in the medium. In human tissue, electrons will interact and damage a variety of locations within the cell including the nucleus, cell membrane, cytoplasm and its organelles. For a reasonably energetic electron transversing through tissue, it will take on the order of 10^{-18}s for the electron to traverse a DNA molecule and on the order of 10^{-14}s to traverse a cell suggesting the initial physical damage of biomolecules occurs immediately following exposure to radiation [101]. While ionization and excitation interactions will occur non-selectively, damage to target structures will be more problematic then damage to other components within the cell. For example radiation damage can result in structural damage to carbohydrates, proteins and lipids which can alter functions in these entities however the rapid and continuous turnover of the cell coupled with the abundance of certain molecules (ex. water, proteins, carbohydrates) within the cell means the consequences of damaging a small portion of these molecules will be minimal [101]. The limited quantity of DNA and its profound biological importance in conducting the cell and parenting future generations makes DNA damage a potentially lethal and significant perturbation. Studies by Warters et al. showed that radiation damage to the cell plasma membrane and cytoplasm were less toxic than DNA associated damage to the nucleus [115] [116], suggesting DNA to be one of the main target structures for ionizing radiation.

The nature of the damage caused by non-selective ionizations and excitations occurring within a single cell can be classified as causing either indirect or direct damage to target structures. Indirect damage is caused by the creation of highly reactive free radical species through electron interactions with non-target biomolecules (ex. water) within the cell, that then go on to cause damage to target structures through a series of rapid (~1 ms [101]) chemical reactions. Roots et al. have demonstrated that 71% of DNA single strand breaks result from indirect radiation damage [117].

Direct ionization or excitation interactions between DNA and ionizing radiation can manifest as: 1) DNA base damage including chemical change to, or loss of, a base in the DNA structure, 2) single-strand breaks (SSB) manifesting as a single break in one of the two DNA backbone chains, 3) double-strand breaks (DSB) appearing as a break in both backbone chains in the DNA molecule, 4) crosslinks which are the formation of covalent bonds between two locations on the same DNA strand (intrastrand), between locations on the two complementary DNA strands, between locations on two different DNA molecules (interstrand) or between a location on the DNA molecule and a protein. While radiation damage to the DNA has the potential to be detrimental to cell function or survival, an important set of mechanisms are executed in response by the cell.

2.3.2 DNA damage response and repair

Following radiation-induced DNA damage a series of pathways referred to as the DNA damage response (DDR) are used to determine cell outcome. First, DNA damage is identified by proteins that survey the genome for damage and upon identification, signal for recruitment of a variety of other proteins, ultimately leading to effector pathway initiation. Together the effector pathways determine the outcome of the cell.

Damage sensor pathways

DNA damage identification and initiation of the damage response pathway involves the phosphorylation of histone H2AX. Within 5-30 minutes of a DNA DSB or SSB proteins which phosphorylate H2AX are recruited to the damaged site [101]. Some examples of such proteins include the ataxia telangiectasia mutated (ATM) and the ataxia telangiectasia and Rad3 related protein (ATR). Phosphorylation of H2AX is also accompanied by the activation of over 700 other proteins [118] and this collection of activated proteins is referred to as the ionizing radiation-induced foci (IRIF). Activation of the DDR and formation of IRIF focuses the cell's attention on damage response by stopping normal cell processes in order to appropriately respond to the damage via three main mechanisms: cell cycle checkpoints, DNA damage repair and cell death.

Cell cycle checkpoints

One of the major effector pathways following formation of IRIF is activation of cell cycle checkpoints which delay cells with detectable DNA damage from progressing into mitosis. This is done to allow more time for damage repair in order to prevent development of mutations or other complications due to mis-repair in the cell's progeny. There are four cell cycle checkpoints and the activation of a specific checkpoint is dependent on the cell cycle phase for which an individual cell is occupying during irradiation.

Cells irradiated while in G1 can undergo G1 arrest which is the delay (transient or permanent) of progression from G1 to S [119]. The S-phase checkpoint applies to cells irradiated in S, causing a reversible delay in this phase by inhibition of any new DNA replication initiation signaling, and as a result slowing down this process [120]. There are two cell cycle checkpoints which result in blocked progression from G2 to M. Cells in G2 during irradiation can undergo the G2-early checkpoint which rapidly blocks progression from G2 to M and requires low radiation doses (above 0.5 Gy) [121] to be activated. The G2-early checkpoint results in a rapid decrease in the number of cells in M post irradiation [122]. The G2-late checkpoint is characterized by a long, dose-dependent G2 delay post irradiation [122] and becomes activated in cells who were irradiated in G1 or S but made it to G2 with DNA damage. As a result, this checkpoint is often initiated several hours after irradiation and leads to an accumulation of cells in G2 [122].

DNA repair

DNA damage repair occurs within 1-2 hours of radiation damage [101]. DSB repair can occur through homologous resection (HR) or non-homologus end joining (NHEJ). These processes along with SSB and base damage repair are described in detail elsewhere (see [101]).

Cell Death

Radiation-induced damage can also lead to cell death in an attempt to avoid dangerous mutations by eliminating the cell as opposed to attempting damage repair. Cell death following radiation damage can occur in two forms: interphase death and post-mitotic death. Interphase death typically occurs within a few hours of irradiation [123] where as a cell may undergo cell cycle checkpoints, DNA repair [101] and pass through full progression of the cell cycle one or two times prior to post-mitotic death [124]. The complex nature of when cell death occurs following irradiation, makes defining a dead cell difficult, therefore it is traditionally described as the loss of clonogenic capabilities of a cell. With this definition of cell death in mind, this process can be accomplished through a variety of mechanisms including: apoptosis, autophagy, necrosis, senescence and mitotic catastrophe.

Apoptosis can be the mechanism responsible for interphase or post-mitotic death. Apoptosis is a sort of programmed cell death, often referred to as type I cell death, which can be initiated by the DDR in the presence of DNA damage. If enough IRIFs are present in a single cell the amount of apoptosis-promoting proteins up-regulated by the IRIF may cause apoptosis before the cell can go on to respond through other effector pathways. Autophagy can also be initiated in response to radiation damage and is often referred to as type II cell death. Necrosis is another possible form of death which is initiated by changes in the cell environment, possibly as a result of radiation-induced damage. Some cells can become senescent following irradiation [124]. This is characterized as a cell which retains some metabolic function but is in a state of cell cycle arrest [125], therefore the cell is no longer dividing and creating viable progeny. Finally, mitotic catastrophe can occur in which a cell entering M phase with DNA aberrations triggers the initiation of a cell death path way (apoptosis, senescence, necrosis or autophagy) ultimately leading to elimination of the cell.

2.3.3 Quantifying and modeling radiation response

Upon exposure to ionizing radiation the fate of a cell can be one of three options: 1) the cell receives no damage from the radiation and is unaffected by it, 2) The cell receives a lethal amount of damage and dies, 3) The cell receives a sub-lethal amount of damage which it attempts to repair. Upon repair of the damage the cell continues to survive however upon unsuccessful repair the cell becomes mutated and survives. If the cell is unable to fully repair the sub lethal damage before it obtains further damage the cell will be more likely to die.

In RT, ionizing radiation is directed at tumour cells in an attempt to cause loss of reproductive ability, incapacitating the uncontrolled cell division associated with tumour cells in an attempt to control the cancer cell population present in the patient. Selection of an appropriate treatment in RT relies on understanding the relationship between a given dose of radiation and the resulting biological effect it has on normal and cancerous tissues. Therefore, it is desirable to quantify the extent of cell killing for a given radiation dose. This can be quantified using clonogenic assays in which a control and irradiated cell population are plated. After a reasonable incubation period, the number of colonies larger then a set threshold (selected to eliminate colonies forming from cells with limited growth potential before they die) are counted for each population. The ratio of the number of colonies formed to the initial number of plated cells is called the plating efficiency for a given cell culture and the ratio of irradiated to control plating efficiency is the surviving fraction (SF). A special case of the SF metric is the SF_2 which is the SF following 2 Gy radiation dose as mentioned in section 1.3.1.

Cell survival curves are a log-linear plot of SF as a function of dose, giving a graphical representation of the dose response of a given cell population. Figure 2.5 demonstrates cell survival curves for a radiosensitive and radioresistant hypothetical cell population relative to a moderately sensitive population. A typical mammalian cell survival curve is characterized by an initial shoulder region at low doses followed by a curved portion which asymptotically approaches SF=0. The curvature of a sensitive cell line will give a very steep drop off in the cell survival curve where as a resistant line will have gradual curvature. This relates to the fact that a sensitive cell line will have a smaller surviving fraction than that for a resistant cell line at the same dose. The cell survival curve can therefore be used to describe the radiation response of a specific cell population.

A cell survival curve can approximately be modeled using the linear-quadratic (LQ) model

$$-\ln(\mathrm{SF}) = \alpha D + \beta D^2. \tag{2.1}$$

The LQ model describes the logarithm of SF as a second order polynomial of dose (D) with the constant term being zero. α and β are the fit parameters which carry units of Gy^{-1} and Gy^{-2} respectively. The ratio $\frac{\alpha}{\beta}$ describes the curvature of the survival

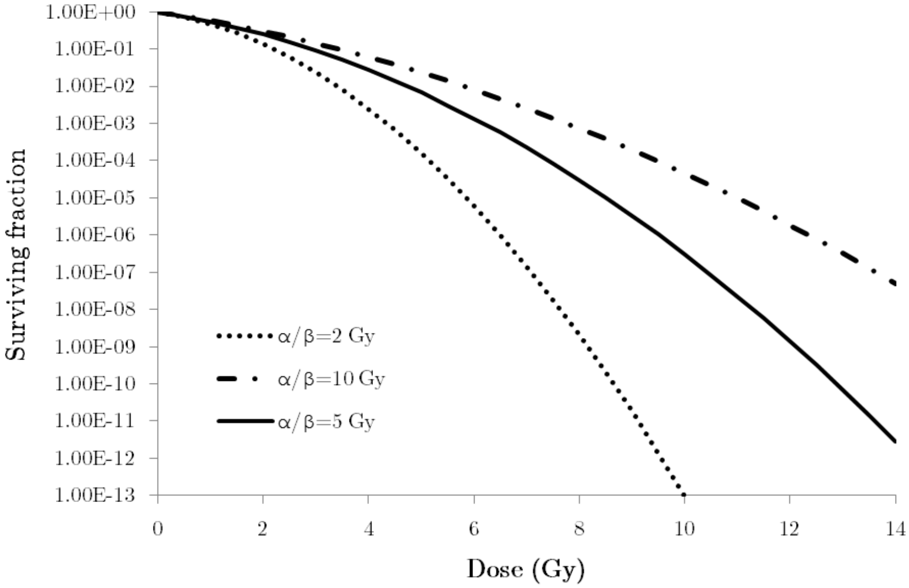

Figure 2.5: Three cell survival curves for a radiosensitive ($\frac{\alpha}{\beta} = 2$ Gy), moderately radiosensitive ($\frac{\alpha}{\beta} = 5$ Gy) and radioresistant cell population ($\frac{\alpha}{\beta} = 10$ Gy).

curve and therefore has a relation to radiosensitivty [109]. A common radiobiological interpretation of the LQ model suggests the linear term corresponds to single DNA lesion cell kill and the quadratic term corresponds to lethality from interaction between two DNA lesions [101]. The LQ model is well adopted for use in experimental and clinical radiobiology and generally works well for modeling *in vitro* and *in vivo* radiation responses [126] [127]. This model describes radiation responses to doses relevant for single fractions of RT (> 1 and < 3 Gy) very well, but as dose increases the quadratic term dominates meaning the curve continues to bend towards 0 rather than become linear as is observed in experiment. For that reason, use of LQ model for modeling response in RT using high acute doses such as in sterotactic surgery has been doubted [128].

Attempts at theoretical and clinical descriptions of dose-response relationships for both tumour (tumour control probability, TCP) and normal tissue (normal tissue complication probability, NTCP) have been made. It is important to identify the dose-response relationship of a tumour or healthy tissue in order to determine the optimal dose for therapeutic gain: high tumour control and low normal tissue response. From the LQ model, $\frac{\alpha}{\beta}$ values for tumour tend to be large while $\frac{\alpha}{\beta}$ for late-responding normal tissue complications tend to be small [101] meaning there is a slight difference in the dose-response relationship between tumour and healthy tissue. This suggests there is a small window of doses for which tumour control will be high and normal tissue complication low, often referred to as the therapeutic window. It is this fact that is the basis for RT and research behind accurate delivery of a prescribed dose. Unfortunately attempts at characterizing dose-response relationships using clinical data can be sparse depending on the treatment site, vary with treatment characteristics [129] and do not account for differences in tumour characteristics between patients [130].

2.3.4 Biological factors affecting radiation response

A thorough understanding of the dose-response relationship in both normal and cancerous tissues can only be obtained through consideration of environmental factors and cell characteristics because these characteristics will determine how the tissue responds to radiation. Important biological factors which will affect tissue response to radiation include cell cycle, tissue micro-environment and re-population.

Cell cycle

Cell sensitivity to radiation will be dependent on the phase of cell cycle an individual cell occupies during irradiation. Sinclair et al. show that cells with a short G1 phase are most sensitive in M and G1 and their sensitivity decreases in G2 and is lowest in S phase. Cells with a long G1 phase were found to be most sensitive during the end of G1, late G2 and M and became less sensitive in early G1 and S [131].

Micro-environment

The tissue micro-environment will also play a role in the sensitivity of that tissue to radiation. Specifically, the presence of O_2 in a cell will increase cell sensitivity to radiation and decrease the required dose to obtain the same level of cell killing [132]. Direct damage to the DNA from radiation (recall section 2.3.1) will create free radicals on the DNA ($\dot{\mathrm{R}}$) which will rapidly react in the presence of oxygen (O_2)

$$\dot{\mathrm{R}} + \mathrm{O}_2 \rightarrow \mathrm{R}\dot{\mathrm{O}}_2 \rightarrow \mathrm{ROOH}\ .$$

This reaction results in stabilization of the DNA radical by fixation of an oxygen compound which is subsequently recognized as DNA damage by the DDR mechanisms and dealt with accordingly. In the absence of oxygen it is more likely that $\dot{R}$ will just recombine with H^+ returning the DNA radical back to its original chemical composition and avoiding the DDR [101]. Therefore, oxygen presence in the cell increases the likelihood of DNA damage and therefore increases radiation sensitivity.

Tumour development is poorly regulated and the corresponding vasculature tends to be poorly distributed as a result, making O_2 diffusion from the blood into the cells difficult. Therefore the tumour micro-environment will contain inhomogeneous regions of oxygenated and hypoxic cells [133]. As a result portions of the tumour will be more sensitive than others to ionizing radiation, thus affecting the overall tumour response.

Re-population

Delivering fractionated RT treatments or radiation doses insufficient to incapacitate all clonogenic cells results in the continued presence of viable cells in the tissue. These cells will continue to divide and re-populate the tissue. In the case of tumours, this re-population can decrease the efficacy of a treatment. However, in the case of normal tissues this fact can allow tissue sparing and recovery between exposures to radiation. This may ameliorate the adverse effects of radiation on normal tissues and allow increased total dose tolerance of the tissue. The rate of cell proliferation will determine how many new cells will appear between treatment fractions which will affect the aggressiveness of the tumour or the severity of normal tissue complication.

2.4 Summary

In this chapter the fundamentals of RT and radiation biology were addressed. RT uses ionizing radiation to preferentially target and kill cancerous cells. The cell is a complex collection of biomolecules and normal cell processes like progression through the cell cycle as well as stress-inducing situations such as radiation-induced cell damage all cause changes to the levels of lipids, proteins, carbohydrates and nucleic acids in a cell. Raman spectroscopy offers a potentially useful technique for identifying these radiation-induced biochemical changes in cells. In the next chapter, a discussion on Raman spectroscopy with specific focus for applications to biological samples will be presented.

Chapter 3

Raman Spectroscopy & Data Analysis

RS involves collecting information about the underlying molecular composition of a sample by way of photon scattering interactions of light in the visible, near-infrared or ultraviolet energy range. The phenomenon of RS was first observed experimentally by Raman and Krishnan in 1928 [134] and has become a valuable technique for applications in biology, materials science, medicine and inorganic and organic chemistry. This chapter presents fundamental background information describing RS. In section 3.1 a brief overview of the physics of RS will be presented. Section 3.2 will address instrumentation and experimental considerations for a Raman experiment and section 3.4 will discuss special considerations for performing Raman experiments on biological material.

3.1 The physics of Raman spectroscopy

Photons incident on a sample can undergo Rayleigh scattering, resulting in no net frequency shift in the scattered photon (elastic scattering). A photon also has the potential to be inelastically scattered. Such interactions are referred to as Raman scattering and exists in two forms.

Stokes Raman scattering originates from photon interactions with a molecule found in its ground vibrational energy state G as shown in Figure 3.1. An incident photon with frequency ν_0 interacts with this molecule by distorting the electron cloud of the molecule causing it to enter a short-lived virtual state. The molecule then

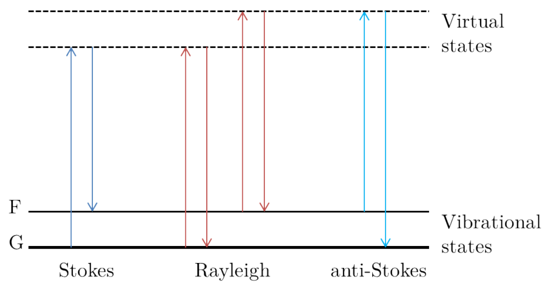

Figure 3.1: Energy level transitions involved in Rayleigh (Red), Stokes Raman (dark blue) and anti-Stokes Raman (light blue) scattering.

returns to an excited vibrational state, F, and concurrently re-radiates the photon with a lower frequency compared to the incident photon.

Alternatively, anti-Stokes Raman scattering originates from photon interactions with a molecule initially in an excited vibrational energy state F as shown in Figure 3.1. The incident photon interacts by distorting the electron cloud of the molecule causing it to enter a short-lived virtual state. Since the molecule was initially in an excited vibrational energy state, de-excitation to the ground vibrational energy state occurs. The resulting scattered photon is shifted to a higher frequency relative to the incident photon.

3.1.1 Classical description of light scattering

Classically, Raman scatter can be described by considering an incident electromagnetic field with frequency ν_0. The non-polarized electric field ($\mathbf{E}$) of this wave, with amplitude E_0 evolves in time (t) according to

$$\mathbf{E} = \mathrm{E}_0 \cos(2\pi\nu_0 t). \tag{3.1}$$

As the incident electromagnetic field approaches the molecule (approximated as a polarizable electron cloud) it will induce a distortion in the electron cloud by displacing charges. This creates a dipole moment $\mathbf{M}$ in the electron cloud which is dependent on the polarizability of the molecule α such that

$$\mathbf{M} = \alpha\mathbf{E}. \tag{3.2}$$

Raman scattering results from interactions of the polarizability with vibrational modes of the molecule. Atomic nuclei in the molecule can vibrate at specific frequencies characterized by the bond characteristics between two atoms. This vibration is referred to as a normal mode (Q). The k$^{\mathrm{th}}$ normal mode has a specific frequency of vibration (ν_k) and amplitude ($\mathrm{Q}_{\mathrm{k}}^{0}$) and evolves in time according to

$$Q_{\mathrm{k}} = Q_{\mathrm{k}}^{0} \cos(2\pi\nu_{\mathrm{k}} t). \tag{3.3}$$

Expanding the polarizability in terms of the k$^{\mathrm{th}}$ normal mode gives

$$\alpha = \alpha_0 + \frac{\delta\alpha}{\delta Q_{\mathrm{k}}} Q_{\mathrm{k}} + ... \tag{3.4}$$

where $\frac{\delta\alpha}{\delta Q_{\mathrm{k}}}$ is the rate of change of the polarizablity with respect to the k$^{\mathrm{th}}$ normal mode about the equilibrium position, and α_0 is the polarizability of the molecule at its equilibrium position. Substituting equations 3.3 and 3.4 (first two terms only for simplicity) into 3.2 gives

$$\begin{aligned}\mathbf{M} &= \alpha_0 \mathrm{E}_0 \cos(2\pi\nu_0 t) + \frac{\delta\alpha}{\delta Q_{\mathrm{k}}} Q_{\mathrm{k}} \mathrm{E}_0 \cos(2\pi\nu_0 t) \\ &= \alpha_0 \mathrm{E}_0 \cos(2\pi\nu_0 t) + \frac{\delta\alpha}{\delta Q_{\mathrm{k}}} Q_{\mathrm{k}}^{0} \cos(2\pi\nu_{\mathrm{k}} t) \mathrm{E}_0 \cos(2\pi\nu_0 t) \\ &= \alpha_0 \mathrm{E}_0 \cos(2\pi\nu_0 t) + \mathrm{E}_0 \frac{\delta\alpha}{\delta Q_{\mathrm{k}}} Q_{\mathrm{k}}^{0} [\cos(2\pi(\nu_0 + \nu_{\mathrm{k}})t) \cos(2\pi(\nu_0 - \nu_{\mathrm{k}})t)]. \end{aligned} \tag{3.5}$$

From equation 3.5 it is recognized that interaction of the electron cloud of a molecule with an incident electric field (**E**) results in an induced dipole (**M**) which arises from a combination of two separate terms. The first term is the Rayleigh light scattering term for which the frequency of the incident electromagnetic field is unshifted. The second term is the Raman term for which the frequency of the incident electromagnetic field is shifted by the frequency of vibration of the involved normal mode; $\nu_0 \pm \nu_{\mathrm{k}}$. Only one in $10^6 - 10^8$ scattered photons will undergo Raman scattering, making Rayleigh the dominant form of photon scattering [135].

Stokes v.s. anti-Stokes Raman scattering

The second term in equation 3.5 contains a portion involving the incident electromagnetic field shifted to higher frequency ($\nu_0 + \nu_{\mathrm{k}}$) corresponding to anti-Stokes Raman scattering. The other portion is shifted to a lower frequency ($\nu_0 - \nu_{\mathrm{k}}$) and corresponds to Stokes Raman scattering. Contrary to what is predicted by equation 3.5, the relative proportion of Stokes v.s. anti-Stokes scattering is not equal but is dependent on the proportion of molecules in excited vibrational states during the interaction. The fraction of molecules in excited vibrational states will be low at room temperature (Boltzmann statistics). Because of this, Stokes Raman scattering is the form of interaction of interest for work in this thesis.

3.1.2 Selection rules for Raman activity

In three dimensions the dipole moment induced from interaction of an electromagnetic field with the electron cloud of a molecule can be described by induced dipole moments along all three spatial dimensions (x, y, z),

$$\begin{bmatrix} M_x \\ M_y \\ M_z \end{bmatrix} = \begin{bmatrix} \alpha_{x,x} & \alpha_{x,y} & \alpha_{x,z} \\ \alpha_{y,x} & \alpha_{y,y} & \alpha_{y,z} \\ \alpha_{z,x} & \alpha z,y & \alpha_{z,z} \end{bmatrix} \begin{bmatrix} E_x \\ E_y \\ E_z \end{bmatrix} \tag{3.6}$$

where α is the polarizability tensor of the molecule and a larger value of α means greater polarizability.

An atomic configuration involving constituent atoms which are closely situated to one another means the electron cloud occupies a smaller volume and as a result is less polarizable than an atomic configuration for which the atoms are further apart from one another and occupying a larger volume of space. The main selection rule governing Raman activity can be found in equation 3.5. We see that the Raman scattering term (second term) in this equation has a prefix of $\frac{\delta\alpha}{\delta Q_{\mathrm{k}}}$, therefore Raman scattering only arises if there is a non-zero change in the polarizability of the molecule during a vibration [136]. Specifically, if one of the elements of the polarizability tensor changes during vibration then it is said to be Raman active.

The number of Raman active vibrations for a given molecule is determined by the types of vibrations available to that molecule. This depends on molecular structure and atomic content. The total number of vibrational degrees of freedom (D) in a molecule containing η atoms is found by subtracting the possible translational and rotational degrees of freedom from the total possible degrees of freedom (3η), since each molecule occupies three dimensional space. For a linear molecule this is

$$D_l = 3\eta - 5, \tag{3.7}$$

and for a non-linear molecule

$$D_{nl} = 3\eta - 6. \tag{3.8}$$

While multiple vibrational modes may exist for a molecule recall that only those causing a change in the polarizability of the molecule are expected to be Raman active. This will be illustrated with a simple example by considering the vibrational normal modes of CO_2. CO_2 is a triatomic linear species ($\eta = 3$), and therefore according to equation 3.7 has four vibrational degrees of freedom. One of these vibrations is a symmetric stretch along the chemical bond (Figure 3.2a), another an asymmetric stretch along the chemical bond (Figure 3.2b) and the last two vibrations are degenerate bending modes with the same vibrational frequency in two different planes perpendicular to the chemical bond (Figure 3.2c) [136].

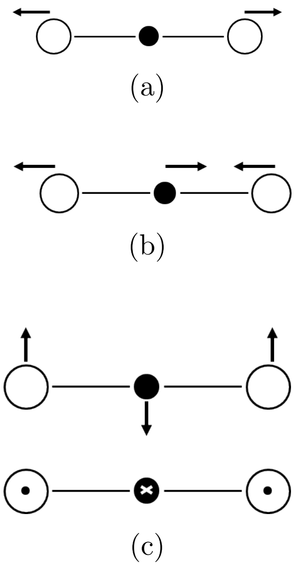
(a)

(b)

(c)

Figure 3.2: The symmetric stretch (a), asymmetric stretch (b) and two degenerate bending vibrational modes (c) of CO_2. The carbon atom is in black and two oxygen atoms in white. Arrows indicate the direction of motion of each atom during the vibration, dots represent motion out of the page and x represents motion into the page.

For a simple molecule the polarizability can be visualized by plotting $1/\sqrt{\alpha}$ along the x, y and z axes (in the molecule's centre of gravity reference frame) to give a polarizability ellipsoid. If the size, shape or orientation of the three dimensional polarizability ellipsoid changes during a vibration then the vibration is Raman active. Characteristics of the polarizability ellipsoid for atomic displacement extrema about the equilibrium position for the two stretching modes of CO_2 are shown in Figure 3.3. The symmetric stretching normal mode of CO_2, shown in Figure 3.3a, is characterized by the two oxygen atoms being very close to the carbon atom at the minima of the stretch where the polarizability of the molecule will be smaller than when the molecule is in its equilibrium position. Conversely, the two oxygen atoms will be very far from the carbon atom at the maxima of the stretch where the polarizability of the molecule will be larger than it is in the equilibrium position. Therefore, in one cycle of the symmetric stretch the polarizability of the molecule will change from relatively small to large about the equilibrium position and so the symmetric stretch is Raman active.

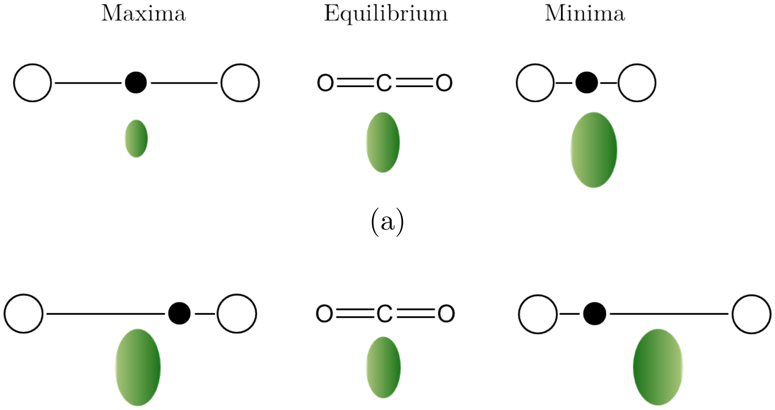

(a)

(b)

Figure 3.3: Symmetric (a) and asymmetric (b) vibrational modes of CO_2 with polarizability ellipses illustrating changes in polarizability during the vibration. By definition a small polarizability ellipse corresponds to a large polarizability (recall the polarizability ellipse is related to $1/\sqrt{\alpha}$).

Now take a look at the asymmetric stretching mode of CO_2, shown in Figure 3.3b. At one extrema of the vibration, one of the oxygen atoms is very close to the carbon atom and the other is very far. The polarizability of the molecule at this extrema will be less than that at the equilibrium position. Similarly at the other extrema of the vibration, the roles of the two oxygen atoms are reversed but the overall effect on the molecule is the same due to the indistinguishable nature of the oxygen atoms. While the size of the polarizability changes during one cycle of this vibration, the degree of change is the same at one extrema and the other. As a result the rate of change of the polarizability near the equilibrium position ($\frac{\delta\alpha}{\delta Q_\mathrm{k}}$) is zero and this vibration is not Raman active. A similar argument can be made for the two bending normal modes of CO_2 and this makes them Raman inactive as well. Generally symmetric vibrations result in Raman activity, while asymmetric vibrations do not. Determining Raman activity in larger molecules is much more complex and can be elegantly described using group theory as described in detail elsewhere [136].

3.1.3 Raman peak intensity

Predicting the intensity of Raman scattered light is valuable for gauging which peaks are expected to be present in a Raman spectrum. Description of Raman peak intensity requires a quantum mechanical approach to light scattering theory and is treated in detail in the literature [137] [138]. Only a brief overview of the main results of such analysis for Raman peak intensities is discussed here. Consider Raman scattering between a ground vibrational state in the ground electronic state (G) and a final vibrational state in the ground electronic state (F), passing through an intermediate vibrational state in an excited electronic state (I). The intensity of this Raman scattering can be described as

$$I = \frac{\pi^2}{c\varepsilon_0^2}(\nu_0 \pm \nu_{GF})^4 \mathrm{E}_0^2 \sum_{\rho\sigma} |[\alpha_{\rho\sigma}]_{GF}|^2. \tag{3.9}$$

Where c is the speed of light, ε_0 is the permittivity of free space, ν_0 and ν_{GF} are the frequencies of the incident radiation and Raman transition between the G and F vibrational states and E_0^2 is the intensity of the incident radiation. $|[\alpha_{\rho\sigma}]_{GF}|^2$ is the $\rho\sigma^{\text{th}}$ element of the transition polarizability tensor which is defined by the Kramer Heisenberg Dirac (KHD) expression. Detailed discussion of the KHD expression can be found elsewhere [135]. However, an interesting result is that solving the KHD expression yields a series of integrals which are non-zero only if there is a single quantum of energy difference between the initial and final vibrational states (i.e F-G= ±1). This is the first selection rule for RS (within the harmonic oscillator approximation). The second selection rule, requiring symmetric vibrations (which result in a change in polarizability), can also be obtained from the solution of the KHD expression. The integrals involved in the solution have operators of ungerade (odd parity) nature so that multiplication of these operators leads to a result which is gerade (even parity). The resulting solution is of even parity and therefore only symmetric vibrations are allowed for Raman scattering.

Equation 3.9 indicates that the Raman peak intensity is dependent on molecular polarizability which is a sample-dependent parameter and can not be controlled by the spectroscopist. Equation 3.9 also indicates that the Raman peak intensity is dependent on incident radiation frequency and intensity. Both of these variables can be controlled by the spectroscopist. The optimal selection of these variables is discussed in detail in section 3.4.1.

3.1.4 Raman shift

In a Raman experiment, the scattered light is detected with frequencies shifted from the incident monochromatic light source. It is convention to report the energy of the detected light as the Raman shift, in units of wavenumbers (cm^{-1}). The Raman shift for a photon with incident frequency ν_0, wavenumber $\bar{\nu_0}$ and wavelength λ_0 with scattered frequency ν, wavenumber $\bar{\nu}$ and wavelength λ is

$$\Delta\bar{\nu} = \frac{1}{\lambda_0} - \frac{1}{\lambda} = \frac{\nu_0}{c} - \frac{\nu}{c} = \bar{\nu_0} - \bar{\nu}. \tag{3.10}$$

3.2 Instrumentation considerations in Raman spectroscopy

Several components are used in concert to make up a working Raman spectrometer, these include: an excitation laser, sample illumination and scatter collection system, sample holder, spectrometer and detecting system. For any one of these items there is a wide array of options and it is up to the spectroscopist to select the optimal combination of instrument components for their specific needs. In this section the vital components for a RS system are discussed in general, as well as in the context of collecting Raman spectra for single cells.

3.2.1 Raman spectrometer

A schematic diagram of a typical Raman spectrometer is shown in Figure 3.4. Light exiting the laser source passes through a series of filters and mirrors and is incident on the sample. Upon interaction scattered light is collected, focused and collimated into a spectrometer. The spectrometer then disperses the light and focuses it onto a detector which is used to count the number of photons at a given wavenumber, producing the Raman spectrum. Details specific to the spectroscopy system used in this work is discussed in chapter 4, section 4.3.1.

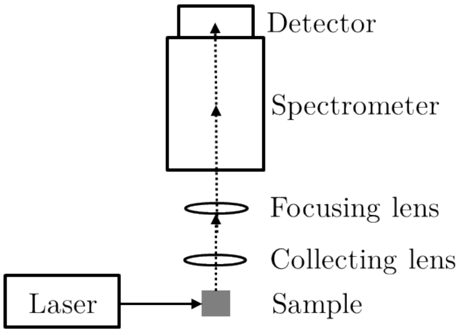

Figure 3.4: Basic schematic of a Raman spectrometer. Laser light is indicated by a solid line and Raman scattered light is indicated by a dashed line.

3.2.2 Raman microscopy

A variation on the traditional Raman spectrometer set up is to couple an upright microscope to the system. Such an instrument is referred to as a Raman microscope (RM). A schematic of a RM is shown in Figure 3.5. Typically the excitation laser is coupled to an upright microscope which acts as the sample holder offering precise spatial control of the excitation laser on the sample by way of a motorized sample stage. Excitation light passes through the microscope objective, is focused onto a small portion of the sample and interacts with the sample in that specific region. The Raman scattered light is also collected by the microscope objective at (typically) a 180° orientation. Scattered light collected by the aperture passes through a series of filters and is passed to the spectrometer and on to the detector, producing the Raman spectrum.

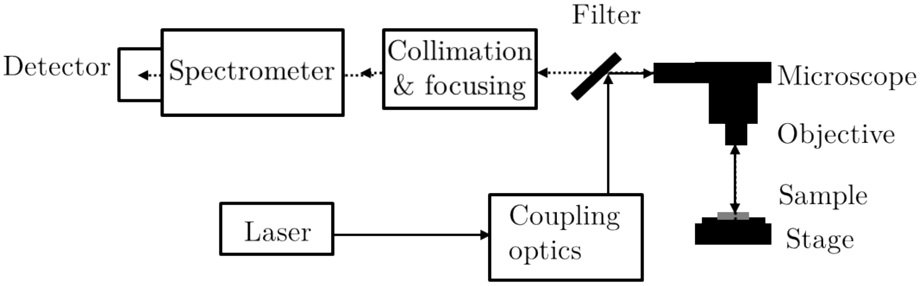

Figure 3.5: Basic schematic of a Raman microscope. Laser light is indicated by a solid line and Raman scattered light is indicated by a dashed line.

Raman microscopy has the advantage that small samples (such as cells) and therefore small amounts of material can be probed [135]. Furthermore, the RM offers good spatial control of the excitation laser and therefore improves selectivity of the sample volume [135]. While there are clear advantages to using Raman microscopy, especially for small samples like individual cells, there are some important technical considerations for optimal operation of this technology.

Microscope coupling

The laser has a specific beam size which must be expanded in order to fill the back aperture of the microscope objective. In doing so the full power of the laser can be used efficiently to excite the selected sample area. The laser is focused through a pinhole and expanded to the appropriate size to match the size of the objective's back aperture.

Objective

The choice of objective used in Raman microscopy will play an important role in the performance of the system. Composition of the objective components must be of sufficient optical quality to avoid creating any confounding fluorescence signals in the Raman spectrum. Also, the numerical aperture (NA) will determine the collection efficiency of the objective and play an integral role in the spatial and confocal resolution of the system. According to [139] NA is defined as

$$NA = \mu \sin \theta, \tag{3.11}$$

where μ is the refractive index in the imaging medium and θ is one half of the objective angular aperture which is defined as the maximum area of the light cone captured by the objective, as shown in Figure 3.6. The brightness of the image collected by the objective will determine the signal strength of the collected spectrum, and is proportional to the square of the NA of the objective and inversely proportional to the square of its lateral magnification. For two objectives with the same magnification, one with a higher NA will have improved light collecting ability and smaller collecting volume.

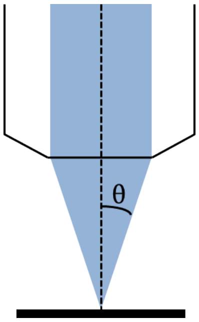

Figure 3.6: Objective with light cone illustrating the value θ, equal to the angle subtended by one half of the area of the light cone. The dotted line illustrates the orientation of the principal optical axis.

The minimum detectable resolution of the objective is dependent on the NA [139]

$$r = \frac{\lambda}{2\mathrm{NA}}. \tag{3.12}$$

The depth of penetration of the laser spot along the principal optical axis is described by the depth of field (DOF) [140]. This value is also dependent on the NA,

$$DOF = \frac{\lambda\mu}{\mathrm{NA}^2}. \tag{3.13}$$

While a higher NA results in better collection efficiency, it also results in a smaller collecting volume. A smaller collecting volume means the laser power density is higher and more concentrated in the volume being sampled. The trade-off to this is that a smaller sample volume is being probed and so the number of molecules present in this volume is reduced compared to a larger sample volume, affecting the already weak Raman signal.

Collection orientation

A 180° collection orientation is ideal for Raman microscopy because it can allow for high powered objectives to be brought close to the sample. This enables the precise focusing of the laser spot onto a small (ex. 10 μm for a 100× objective) portion of the sample. Both Rayleigh and Raman scattered light are collected by the objective. A filter is used to remove the Rayleigh scattered light and isolate the Raman signal following collection of the scattered light as shown in Figure 3.7. This light is then focused and passed through a confocal (along the principal axis of the optics system) aperture as shown in Figure 3.7, improving the spatial resolution of the

Raman system and removing undesirable signals originating from outside the region of interest in the sample. Light emerging from the confocal aperture is then passed on to the spectrometer.

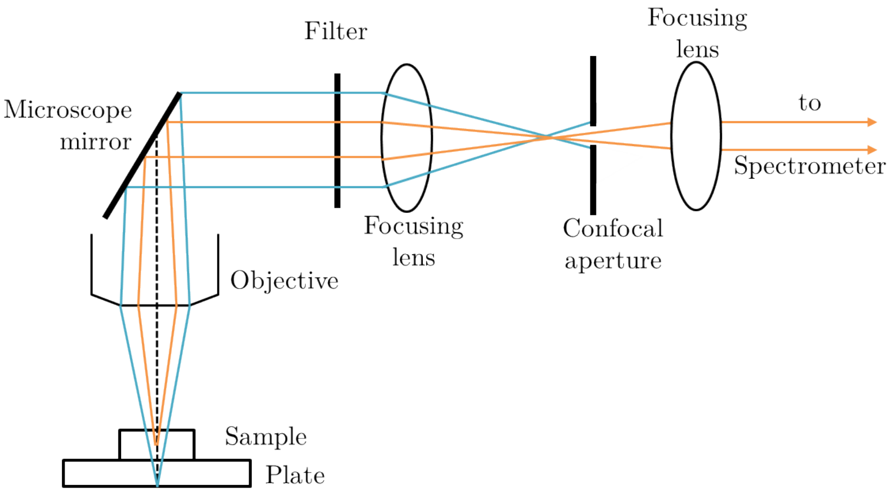

Figure 3.7: Filtering and collimation of Raman scattered light prior to entering the spectrometer. The orange rays represent scatter originating within the region of interest and blue rays represent scatter originating outside of the region of interest. The principal axis is indicated by the dotted line.

3.2.3 Principles of light dispersion

Raman scattered light collected from the aperture is passed into the spectrometer where the various wavelengths of light scattered off the sample are separated before moving on to the detector. Modern RS uses either a dispersive or Fourier transform (FT) spectrometer system [135]. FT spectrometers are typically used with infrared excitation lasers and use an interferometer based system making use of FT mathematics to produce the spectrum. Dispersive spectrometers are typically used with visible laser excitation wavelength. The spectrometer used in the work presented in this thesis is a derivation of the single grating Czerny-Turner dispersive spectrometer (as shown in Figure 3.8). Light incident on the entrance slit of the spectrometer is focused onto and reflected by a plane mirror onto a diffraction grating. Light of a specific wavelength emerges from the diffraction grating at a unique angle, according to

$$\sin\alpha + \sin\beta = 10^{-6}kn\lambda. \tag{3.14}$$

Where α and β are the angle of incidence and angle of diffraction of light with wavelength λ, k is the diffraction order and n is the density of slits in the diffraction grating. Therefore the angle of diffraction is dependent on the wavelength of the light, and it is this fact which allows separation of the various wavelengths of Raman scattered light. The separated light is then reflected off a second plane mirror and focused at the focal plane of the spectrometer.

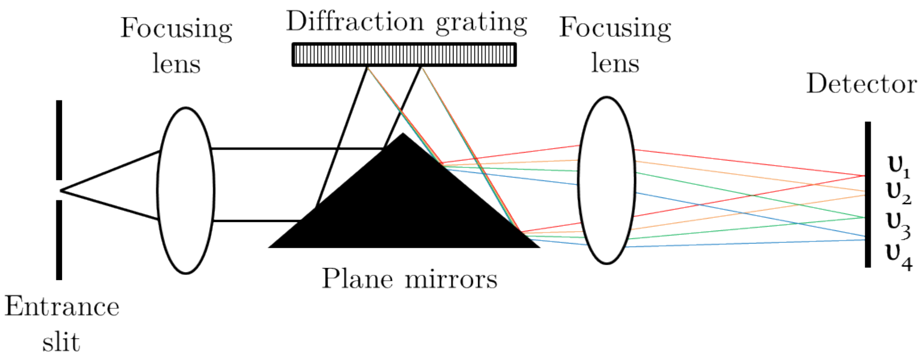

Figure 3.8: Schematic of light dispersion in the single grating spectrometer. Light of differing frequencies (ν_x) diffract from the grating at a unique angle. Light of the same frequency reaches the detector at the same, discrete position.

The spatial distribution for the light emerging from the spectrometer is dependent on the linear dispersion of the diffraction grating. The linear dispersion defines the amount of spread of a given spectral interval across the focal field of the spectometer [141]. The linear dispersion is commonly expressed in terms of $\frac{nm}{mm}$ and is defined according to

$$\frac{d\lambda}{dx} = \frac{10^6 \cos\beta}{knL_B}, \tag{3.15}$$

where x is the unit interval and L_B is the effective exit focal length. In understanding the implications of linear dispersion, consider diffraction grating A which disperses 1 nm over a 1 mm range and diffraction grating B which disperses 100 nm over a 1 mm range. More spectral detail would be shown in spectrometer A compared to B, and spectrometer A is referred to as having a higher linear dispersion compared to B. From this example it is clear that linear dispersion is associated with describing the ability of a spectrometer to resolve fine spectral detail. The spatial distribution of the light becomes very important as it is passed on to the detector.

3.2.4 Detecting and displaying Raman spectra

A common detector used in RS is the charge-coupled device (CCD) [136]. A CCD is comprised of a two dimensional array of photosensitive diode detector elements as shown in Figure 3.9. CCD elements range in size from 6-30 μm along each pixel dimension, and are made of a silicon-metal-oxide semiconductor material [142] making up the photosensitive material on the detector element. Each edge of the element is held at a positive charge and connected to the grid circuit, defining the CCD array. Photons incident on the photosensitive silicon material of a detector element cause electrons to be released from the material, resulting in an accumulation of charge proportional to the photon intensity incident on the element and the length of time an element is exposed. This later point contributes to why it is important to control the acquisition time between independent Raman experiments (see chapter 4, section 4.3.2). Once exposure of the CCD is complete, the charges collected on each element in a column are transferred sequentially down the column to the end element. In the Raman spectrometer used for this work the charge coupling occurs along the binning axis as labeled in Figure 3.9. The collected charge on each element at the end of each column is then read out along the dispersion axis (Figure 3.9), converted into a voltage, amplified and converted into a digital signal. The read out signal at each column is proportional to the binned charge collected (and hence number of photons exposed) at each column position in the detector.

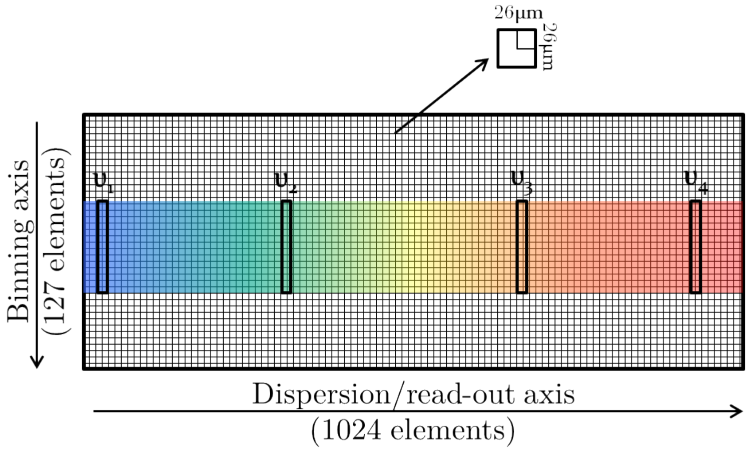

Figure 3.9: Schematic of a charge-coupled device (CCD) detector. Light of differing frequencies (ν_x) are separated out spatially by the diffraction grating and each frequency hits a different part of the CCD. Incident photon intensities are binned along the binning axis and read out along the dispersion axis.

In a Raman system the CCD is placed at the focal plane of the spectrometer and because the various Raman shifts have been spatially dispersed from the spectrometer, each wavelength falls at a unique position of the detector (Figure 3.9). Each pixel column will detect photon intensities for the wavelength of light landing at that specific spatial region of the detector array.

3.3 Data analysis

A single Raman experiment can contain a large number of spectra and making sense of the trends present between the spectra in this data set can be a daunting task. A variety of data analysis techniques have been explored for applications in making sense of the large data sets inherent to a Raman experiment. Such techniques include linear discriminant analysis, hierarchical cluster analysis and principal component analysis (PCA) [143]. PCA is the data analysis technique used throughout the work presented in this thesis and therefore the theoretical basis of this technique is presented here. Details specific to applications in this thesis are discussed in chapter 4, section 4.4.4.

PCA takes a set of observations which are potentially correlated and performs an orthogonal linear transformation of that data set to a basis in which projection of the data onto the first coordinate of this basis yields the greatest variance of the set of observations. For that reason, PCA is useful in analyzing data sets where the relationships between the variables are not easily visualized.

A rigorous description of PCA can be found in [144]; only main concepts in PCA will be addressed in this thesis. Define an $n \times p$ matrix ($\mathbf{X}$) containing the observations ($x_{i,j}$) in the form of: n samples ($i = 1, ..., n$) and p measurements ($j = 1, ..., p$). The empirical mean of $\mathbf{X}$, is a row vector ($\bar{\mathbf{X}}$) and is defined as the mean of all measurements in the j^{th} column over all n samples

$$\bar{x}_j = \frac{\sum_{i=1:n} x_{i,j}}{n}. \tag{3.16}$$

The centred data set ($\tilde{\mathbf{X}}$) is found by subtracting the mean of each measurement ($\bar{\mathbf{x}}_\mathbf{j}$) from $\mathbf{X}$ [144]

$$\tilde{x}_{i,j} = x_{i,j} - \bar{x}_j. \tag{3.17}$$

The sample covariance matrix ($\mathbf{C}$) of $\tilde{\mathbf{X}}$ is then determined according to

$$\mathbf{C} = \frac{\tilde{\mathbf{X}}^{\dagger}\tilde{\mathbf{X}}}{n-1}. \tag{3.18}$$

Using computing techniques the following equation must be solved such that $\mathbf{C}$ is diagonalized

$$\mathbf{A}^{\dagger}\mathbf{C}\mathbf{A} = \mathbf{\Lambda}, \tag{3.19}$$

Where matrix $\mathbf{A}$ is the orthogonal matrix containing the eigenvectors of $\mathbf{C}$, each with length p. $\mathbf{\Lambda}$ is the diagonal matrix containing the eigenvalues (λ) of $\mathbf{C}$. The set of eigenvectors described in $\mathbf{A}$ forms a complete orthogonal basis set [144] of $\tilde{\mathbf{X}}$ and it follows that

$$\alpha_{\mathbf{i}}^{\dagger}\alpha_{\mathbf{j}} = \delta_{ij}. \tag{3.20}$$

The k^{th} eigenvector of $\mathbf{C}$, corresponds to the k^{th} column of $\mathbf{A}$, namely $\alpha_{\mathbf{k}}$, and is referred to as the k^{th} principal component (PC). The PCs described in $\mathbf{A}$ each correspond to a specific eigenvalue of $\mathbf{C}$. According to [144], the eigenvalues in $\mathbf{\Lambda}$ correspond to the variance a specific PC contributes to the total variance of the data set $\tilde{\mathbf{X}}$

$$\lambda_k = \text{variance}(\tilde{\mathbf{X}}\alpha_{\mathbf{k}}). \tag{3.21}$$

A PC describes the relationships between measurements and all PCs are orthogonal to one another. The first ($k = 1$) PC is selected to correspond to the largest variance and so explains the largest portion of the total variance of $\tilde{\mathbf{X}}$. Similarly, the second PC contributes the second largest variance and the k^{th} PC, has the k^{th} highest variance.

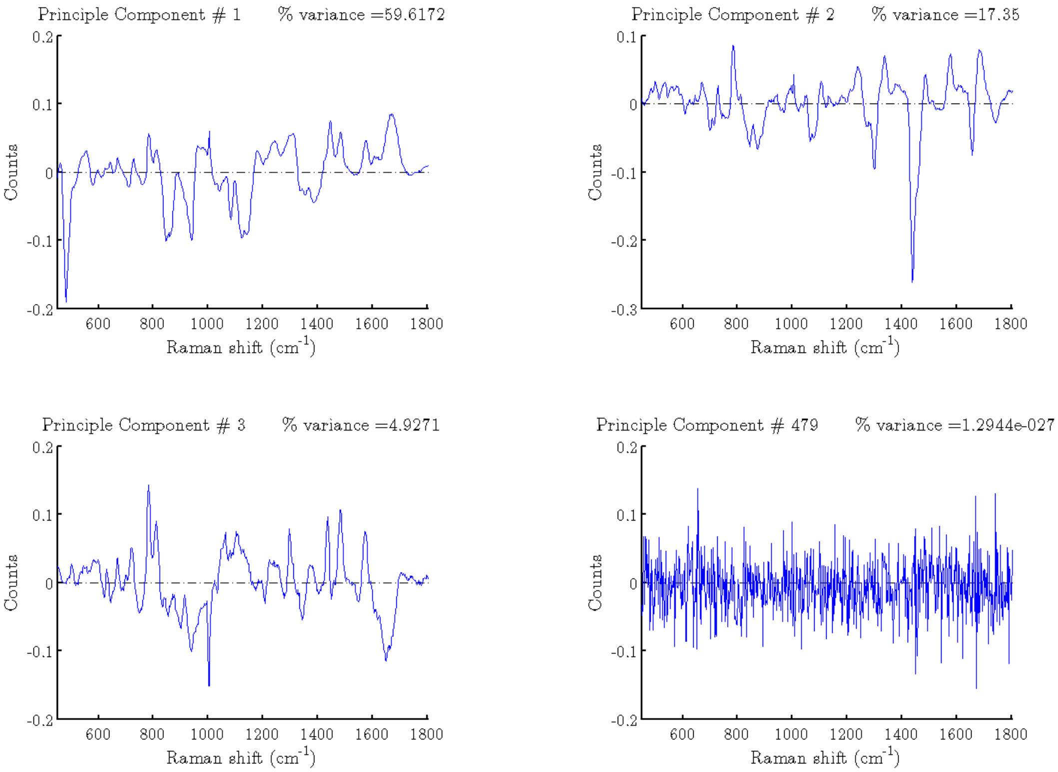

Figure 3.10: Components 1, 2, 3 and 479 with their respective percent variances for an $n = 480$ data set.

Figure 3.10 illustrates this concept by presenting the 1st, 2nd, 3rd and 479th PCs and their respective percent variances for a hypothetical data set containing $n = 480$ samples. As expected, the 1st PC holds the largest percent variance and the 479th holds the lowest. With reference to Figure 3.10 some conclusions about PCs can be made:

1) The first few PCs contribute the most significantly to the total variance of the data set. In this example PCs 1, 2 and 3 combine to give approximately 80% of the total variance, leaving the remaining 476 components to make up 20% of the total variance. Because the variance is larger in the first few PCs, they will contain information which represents the variability in the data set more than the later PCs. Therefore, PCA can be used to essentially reduce the size of a data set.

2) A single PC will contain both positive (counts > 0) and negative features (counts < 0). The selection of which features are positive and which are negative is arbitrary, and the features can be reflected about zero without affecting the results. However, according to [144] it is important that the positive and negative features remain complimentary to one another, in order to maintain orthogonality of the basis set.

The PC score of the k^{th} PC, can be found for all ($\tilde{\mathbf{x}}_\mathbf{i}$) samples in $\tilde{\mathbf{X}}$ (n samples total) using

$$z_{i,k} = \tilde{\mathbf{x}}_\mathbf{i} \alpha_\mathbf{k}, \tag{3.22}$$

where $i = 1...n$.

The degree of expression of a PC for a given sample is quantified using PC scores. Therefore, a single sample ($\mathbf{x_i}$) in the full data set ($\mathbf{X}$) can be reconstructed using the PC scores as weightings for the PCs,

$$\mathbf{x_i} = \bar{\mathbf{x}} + z_{i,1}\text{PC}_1 + z_{i,2}\text{PC}_2 + z_{i,3}\text{PC}_3 + ...z_{i,n-1}\text{PC}_{n-1}. \tag{3.23}$$

The PC scores describe the contribution of each PC in reconstructing the i^{th} sample. To visualize how PC scores facilitate interpretation of a data set, consider a hypothetical data set containing 30 samples (n=30), from three different sample populations within a single experiment (10 samples per population). The PC scores for this data set are shown in Figure 3.11, and the PCs of this data set are identical to those shown in Figure 3.10.

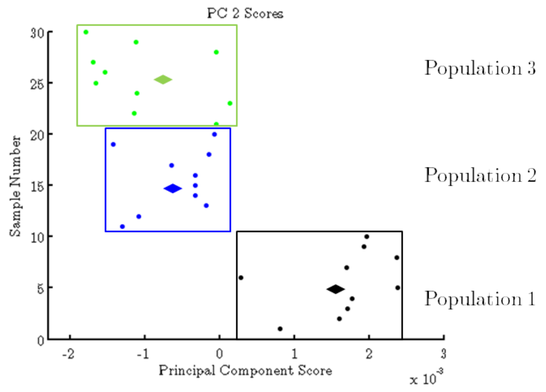

Figure 3.11: Principal component (PC) scores for a hypothetical data set ($n = 30$). Individual data points represent the PC score for one sample. The square region contains all samples in a population and the diamond data points represent the mean PC score for each population.

The PC score of a sample (circular data points in Figure 3.11) represents how much that PC is represented in that sample. Negative PC scores correspond to a greater expression of the negative features relative to the positive features of that PC, where as positive PC scores correspond to a greater expression of positive features relative to negative features. Using PC scores, the experimenter can identify trends between populations, and also between samples within a population.

The mean PC score for a population can be found by averaging the PC scores for each sample in a population. The mean PC score for each of the hypothetical populations in Figure 3.11 is described by the horizontal diamond marker in each population box. The mean PC scores for populations 2 and 3 are shifted more negative relative to population 1. This means that PC 2 describes variability arising from differences between samples in population 1 relative to populations 2 and 3. If population 1 differs from populations 2 and 3 by some controlled variable, the variability arising between these populations would be related to that controlled variable.

3.4 Biological experiment considerations in Raman spectroscopy

Applications of RS to living biological samples requires special consideration of experimental parameters such as laser wavelength and power, spectral region of interest, sample holding environment and spatial resolution. These considerations are addressed here, in general, and those details specific to the work presented in this thesis can be found in chapter 4, section 4.3.

3.4.1 Laser wavelength and power

The choice of excitation laser wavelength, power and exposure time is important for Raman experiments with biological materials, and specifically living cells. These factors will all affect Raman peak intensity, spectral quality (in terms of biological fluorescence) and cell viability and phenotype.

Inherently low Raman scatter efficiency can be addressed by choice of laser wavelength and power. Recall equation 3.9 shows that the intensity of Raman peaks is proportional to the frequency of the excitation laser to the fourth power and the intensity of the incident laser light. This suggests the use of a low wavelength excitation laser, such as in the ultra violet (UV) range and high laser power is necessary in order to increase the Raman peak intensity as much as possible.

Biological fluorescence levels increase for low laser wavelengths [145]. Biological fluorescence causes a high background in the spectrum of already weak Raman peaks and therefore must be minimized. This can be done by using lasers with wavelengths in the upper visible or near-infrared region ($\lambda \geq 600$ nm) [145] [146]. Also, reducing the incident laser power will reduce biological fluorescence however in doing so the Raman scattering intensity will also decrease. Therefore there is a clear trade-off between pushing towards increased Raman peak intensities while minimizing biological fluorescence. Fortunately high powered lasers in the near-infrared region (ex. 785 nm) significantly reduce biological fluorescence and operate in the spectral region for which CCD detectors have relatively high quantum efficiency [143], making the 785 nm laser a good compromise in this trade-off.

Maintaining phenotypic integrity and viability in the cell while collecting the Raman spectrum is important for ensuring the cellular state observed during the measurement was not a perturbation of its natural state as a result of taking the measurement. Laser wavelength, exposure time and power all contribute to the extent of photodamage causing loss of phenotypic integrity. Puppels et al. showed that cell exposure to light for 5 minutes caused sample degradation for laser powers from 0.5-20 mW at 457.9 nm, 488 nm and 514.5 nm but not at laser powers of up to 20 mW for wavelengths of 632.8 nm or 660 nm [147]. This suggests that larger wavelengths cause less photodamage in individual cells exposed to laser light. Further evidence to this was demonstrated by Notingher et al. by showing that irradiation of single, living human cells exposed to 785 nm light with 115 mW power and 40 minute exposure did not cause noticeable changes to the Raman spectrum of the cells or affect cell viability [148]. Meanwhile, Notingher et al. also showed that irradiation of cells with 488 nm or 515 nm light at 5 mW power for less than 5 minutes caused loss of viability and drastic morphological changes [148]. Therefore the use of a higher laser wavelength (ex. 785 nm) reduces photodamage to cells and allows much higher laser powers and exposure times to be used.

A trade-off exists in selection of laser wavelength, power and exposure time between obtaining improved Raman peak intensities and reducing cell photodamage and biological fluorescence. As previously mentioned, a 785 nm laser wavelength is optimal for avoiding cell photodamage and overpowering biological fluorescence. The efficient conversion of light to charge in modern CCD detectors at the spectral range associated with excitation at 785 nm makes the trade-off of lower Raman peak intensities at this (relatively) higher wavelength less problematic [143]. Also, because the 785 nm laser does not induce noticeable levels of photodamage in live cells for high laser powers and long exposure times Raman peak intensity can be improved by using a higher total integrated (over time) laser power exposure. For these reasons collecting Raman spectra of live single cells is optimal with a 785 nm laser.

3.4.2 Spectral considerations

There are two spectral ranges of primary interest for biological samples. Various Raman active normal modes belonging to protein, nucleic acid, lipid and carbohydrates have Raman shifts between 450-1800 cm^{-1}. Lipid and proteins also have Raman shifts from 2400-3600 cm^{-1}. It is therefore constructive to collect Raman spectra in these specific ranges when studying biological materials. In the context of work presented in this thesis spectra are only collected in the 450-1800 cm^{-1} range. This was decided because all four of the important biomolecules for cells have Raman peaks in this range as opposed to the higher wavenumber range which only really has lipid and protein contributions.

3.4.3 Sample holding environment

When collecting spectra of live cells is it important to consider the environment surrounding the cells during data acquisition. Cells can be kept in an aqueous suspension if immersion objectives are used [59], and held at their incubation temperature during data collection if sample heating stages are used as well [149]. Another technique involves growing cells onto slides and freeze drying [150] in which case a dry objective can be used. Cells can also be fixed onto a disk of appropriately selected material, in which case a dry objective is employed [100], and it is this technique which is used for the work presented in this thesis.

If the plating substrate is within the sample volume of the laser it has the potential to contribute background fluorescence and Raman peaks in the spectra collected. By selecting a plating substrate which does not have Raman peaks in the wavenumber region of interest confounding Raman peaks from the plating substrate can be avoided. Also selecting a substrate with low background fluorescence is ideal because of the inherently low intensity of Raman peaks. As long as the background fluoresence is minimal enough to allow good presentation of the Raman peaks in the biological sample and has a reproducible and consistent background, spectral processing techniques can be used to remove these effects [151]. A variety of substrate materials have been investigated for use in RS including sodium glass [145], quartz [145] [150], barium fluoride [152], magnesium fluoride [100] and calcium fluoride [145] [153]. Of these materials the X-F$_2$ materials appear to work best for RS [145].

3.4.4 Spatial resolution

The size of a cell is typically on the order of tens of micro-metres and, within the cell, organelles are on the order of 50-100 nm [114]. Selecting both the spatial and confocal resolution of the laser spot is therefore dependent on the application of interest. The study of sub-cellular distributions of biomolecules, ex. contents in the nucleus compared to cytoplasm will require spatial and confocal resolutions on the order or less than 1 μm^3 [57]. On the contrary studying the entire biochemical content of the cell with little interest in differentiating between sub-cellular regions will require spatial and confocal resolutions on the order of the size of the cell.

3.5 Summary

In this chapter concepts in theory and instrumentation associated with RS were presented. Particular focus was made on the applications of RS to study biological materials. Instrumentation and Raman spectral acquisition parameters specific to the original work presented in this thesis are discussed in chapter 4.

Chapter 4

Materials and Methods

This chapter introduces the materials and specific experimental methodologies used for the work presented in this thesis. Section 4.1 presents the cell cultures used and the protocols for maintaining them. Section 4.2 discusses the protocol for irradiating cell populations including LINAC set-up and dosing schedule. Protocol for collecting cell cycle and viability information for the populations is also presented in this section. Raman microscope and data acquisition parameters are discussed in section 4.3 and, lastly, spectral processing and data analysis protocols are outlined in section 4.4.

4.1 Cell lines and culture parameters.

4.1.1 Radiobiological parameters of cell lines.

Cancer cell lines used in this work were derived from a human host and have been selected based on tissue of origin, literature reported surviving fraction after 2 Gy (SF_2), and p53 gene status. The cell lines used, and selected biological parameters are described in Table 4.1. The SF_2 value reported for each cell line in Table 4.1 is an average of literature reported values, compiled by Matthews et al. and reported in [100].

4.1.2 Storage and maintenance of cell lines

Cell culturing was performed in a laminar flow biological safety cabinet (BSC) to maintain sterility of the cell populations. This work took place in the biological safety level 2 (BSL2) lab at The Deeley Research Centre (DRC) located at British

Cell Line	**Tissue Origin**	**Source**	**SF_2**	**p53 Status**
H460	Lung	ATCC	0.64[100]	wt[154]
MCF-7	Breast	ATCC via ARU	0.64 [100]	wt[39]
MDA-MB-231	Breast	ATCC via ARU	0.71[100]	mt[155]
LNCaP	Prostate	ATCC via ARU	0.27 [100]	wt[39]

Table 4.1: Cell lines explored in this work and relevant biological parameters. Radiosensitivity of each cell line is described by the average literature reported surviving fraction at 2 Gy (SF_2). p53 gene status is listed as wild-type (wt) or mutant-type (mt). Abbreviations: ATCC: American Type Culture Collection, ARU: Antibody Research Unit at British Columbia Cancer Agency's Vancouver Island Centre.

Columbia Cancer Agency's Vancouver Island Centre (BCCA-VIC). Cells were cultured according to protocol typical for adherent cell lines. Growth characteristics and cell morphology are unique to each cell line, and the morphological differences are demonstrated in the optical images of Figure 4.1.

Cells were received either directly from American Type Culture Collection (ATCC, Manassas, VA, USA) or ordered through ATCC but obtained for this work via Dr. Xiaobo Duan formerly of the Antibody Research Unit (ARU) at DRC. Once received, stock cells were cryopreserved by suspending cells in fetal bovine serum (FBS) (Hyclone Labs Inc., Logan, UT, USA) supplemented with 10% dimethyl sulfoxide (DMSO) (Hyclone) by volume and frozen at a rate of 1°C/minute in a -80°C freezer. Once frozen, cells were transferred for long-term storage in a nitrogen vapour storage tank at -182.0°C.

Stock cells remained cryopreserved until a few weeks prior to experiments in order to minimize the amount of genetic variation, aging and transformation which may occur from continuous propagation of the cell line. In preparation for an experiment, the cell line of interest was thawed by bringing the cryopreserved cell pellet to 37.0°C and resuspending in either Roswell Park Memorial Institute (RPMI) or Dulbecco's Modified Eagle's Medium (DMEM) (both from Hyclone) , as listed in Table 4.2. The sample was then placed in a centrifuge and spun at 1500 rpm for 5 minutes at 4°C to separate cell from suspending media. The supernatant liquid was poured off, and the isolated cells resuspended in 1 mL of media. An aliquot of this cell suspension was plated in a T-75 cell culture flask (75 cm^2 growth area, polystyrene, vented cap, BD Falcon Franklin Lakes, NJ, USA) containing 15 mL of media. The size of aliquot

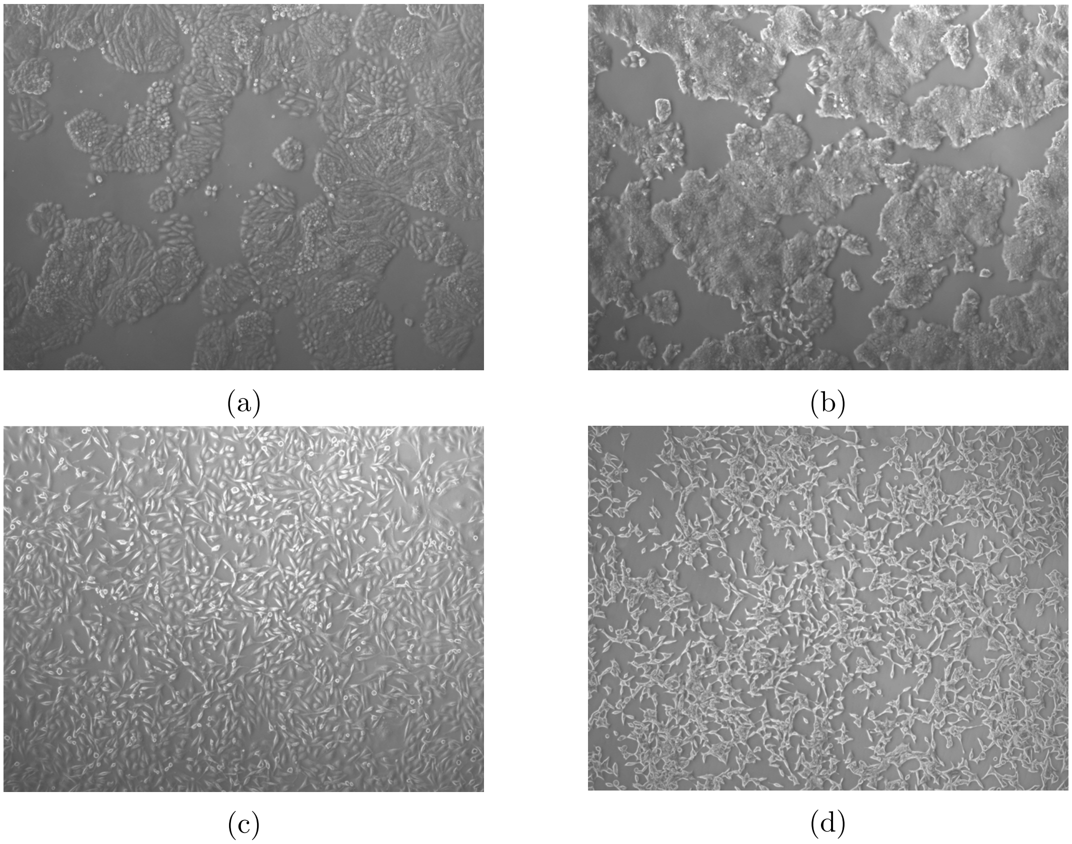
(a) (b) (c) (d)

Figure 4.1: Optical images depicting the physical morphology of (a) H460, (b) MCF-7, (c) MDA-MB-231 and (d) LNCaP cell lines. Images were collected using a optical microscope with a 5x objective.

used is dependent on the growth characteristics of the cell line and is selected so that within the incubation period cells will remain in exponential growth phase. Splitting ratios (which determine the size of aliquot used) are listed in Table 4.2. The flask was then placed in an incubator at 37.0°C with 5% CO_2.

The population was split every three to four days in order to keep the number of cells in a flask below 50-60% confluency, promoting exponential growth and also to avoid exhausting the media's nutritional content. This was done by first pouring off the old media and rinsing fixed cells with 9 mL of Phosphate Buffer Saline 1x 0.0067 M PO_4 (PBS) (Hyclone) to remove any excess media and debris. Enzymatic dissociation of cells was achieved by adding 3 mL of 0.25% Porcine Trypsin-EDTA(1X) (Hyclone) to the flask and allowing the cells to rest in trypsin at 37.0°C for 5-10 minutes. Once all cells detached, the solution was mixed with 9 mL of media and spun down in a centrifuge at a rate of 1500 rpm for 5 minutes at 4°C. The supernatant was poured off then cells were resuspended in 1 mL of media and plated into a T-75 flask filled with 15 mL of media, using the splitting ratios listed in Table 4.2. The flask was then placed back in the incubator for another 3-4 days of exponential growth.

Cell Line	**Media Characteristics**	**Splitting Ratio**
H460	RPMI-1640 Medium + L-Glutamine + 25 mM HEPES + 10% FBS	1:30
MCF-7	DMEM High Glucose Medium 4500 mg/L Glucose + 4.00 mM L-Glutamine + Sodium Pyruvate + 10% FBS	1:10
MDA-MB-231	DMEM High Glucose Medium 4500 mg/L Glucose + 4.00 mM L-Glutamine + Sodium Pyruvate + 10% FBS	1:5
LNCaP	RPMI-1640 Medium + L-Glutamine + 25 mM HEPES + 10% FBS	1:3

Table 4.2: Cell culturing parameters. Abbreviations: RPMI: Roswell Park Memorial Institute, HEPES: 4-(2-hydroxyethyl)-1-piperazineethanesulfonic acid, FBS: fetal bovine serum, DMEM: Dulbecco's Modified Eagle's Medium .

4.2 Cell irradiation

4.2.1 Preparation for irradiation

In preparing a cell line for a radiation experiment, the stock cells were brought to a 1 mL suspension according to the protocol mentioned in section 4.1.2 and this suspension was split according to the splitting ratio listed in Table 4.2. A single aliquot was placed into 1 of 24 T-75 flasks containing 15 mL of media, giving 24 identical cell populations. These flasks were left to incubate for 96 hours such that the cells become approximately 50% confluent. One hour prior to irradiation the expended culture media was replaced with 15 mL of fresh media. All flasks were removed from the incubator at the same time and were stored in a closed box to minimize exposure of the cells to light. All flasks were kept outside the incubator for the duration of the cell irradiations and this time never exceeded 40 minutes.

Set-up Parameter	**Value**
Gantry Rotation	180.0°
Collimator Rotation	0.0°
X Field Dimension	30.0 cm at isocentre
Y Field Dimension	30.0 cm at isocentre
Couch Vertical	5.4 cm
SSD	95.0 cm
SAD	100.0 cm

Table 4.3: Linear accelerator (LINAC) set-up parameters. Abbreviations: SSD: Source to Surface Distance, SAD: Source to Axis Distance.

A Varian 21EX LINAC (Varian Medical Systems Inc., Palo Alto, CA, USA) was set up with geometry as described in Table 4.3. Flasks were placed on the treatment bed symmetrically about the photon beam's central axis between two 5 cm thick, 40×40 cm^2 area, slabs of water equivalent plastic material (solid water) (Gammex RMI, Middleton, WI, USA). The flask surface to which the cells were attached was placed at the LINAC's isocentre. Flask orientation and LINAC set-up is illustrated in Figures 4.2 and 4.3 respectively.

All irradiations were carried out using 6 MV photons at a dose rate of 6 $\frac{\text{Gy}}{\text{min}}$ at isocentre. The monitor units (MU) required to deliver a dose of 2 Gy (MU_2) to isocentre at a depth of 5 cm in water was calculated using the Vancouver Island Cancer Centre MU Calculator version 5.05 courtesy of Dr. Will Ansbacher. The MU required can be found using equation 4.1 where 1 $\frac{\text{cGy}}{\text{MU}}$ is the LINAC output factor for a 10 cm × 10 cm field at isocentre at a depth of d_{max}.

$$\begin{aligned} \mathrm{MU}_2 &= \frac{2\ \mathrm{Gy} \times \frac{100\mathrm{cGy}}{\mathrm{Gy}}}{1\frac{\mathrm{cGy}}{\mathrm{MU}} \times \mathrm{TMR} \times \mathrm{NPSF} \times \mathrm{ISL} \times \mathrm{HF}} \\ &= \frac{200\ \mathrm{cGy}}{\frac{1\ \mathrm{cGy}}{\mathrm{MU}} \times 0.939 \times 1.038 \times 1.000 \times 1.043} \\ &= 196.656\ \mathrm{MU} \\ &= 197\ \mathrm{MU}. \end{aligned} \tag{4.1}$$

Where:

$\mathrm{TMR}(d, r_d, E)$ =0.939=Tissue Maximum Ratio; at depth d=5 cm water, for field size of r_d= 30 .0 cm at the calculation point, with beam energy E=6 MV.

$\mathrm{NPSF}(r_d, E)$=1.038= Normalized Peak Scatter Function; for field size r_d= 30.0 cm at the calculation point, for a 6 MV beam.

ISL= 1.000 = Inverse Square Law Factor (because calculation point is at isocentre).

$\mathrm{HF}(r_c, E)$= 1.043 = Head Scatter Factor; for collimator size $r_{c,x}$=30.0 cm and $r_{c,y}$=30.0 cm, for a 6 MV beam.

The MU required to deliver all doses other than 2 Gy were then calculated by applying an appropriate multiplicative factor to MU_2. The MU used to deliver all doses used for the single dose experiment are listed in Table 4.4.

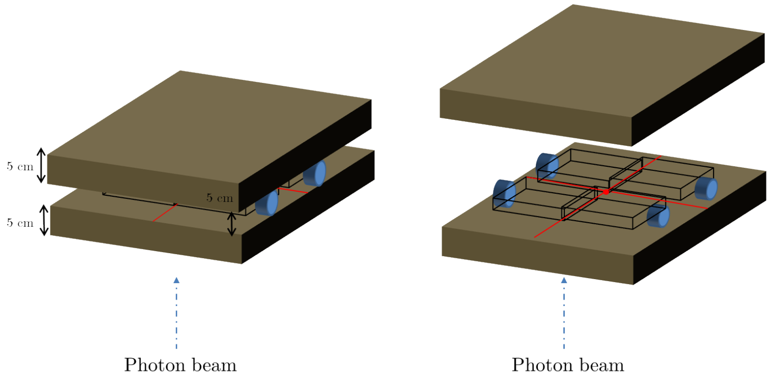

Figure 4.2: Flask orientation for cell irradiation relative to isocentre (indicated by red dot in the image to the right).

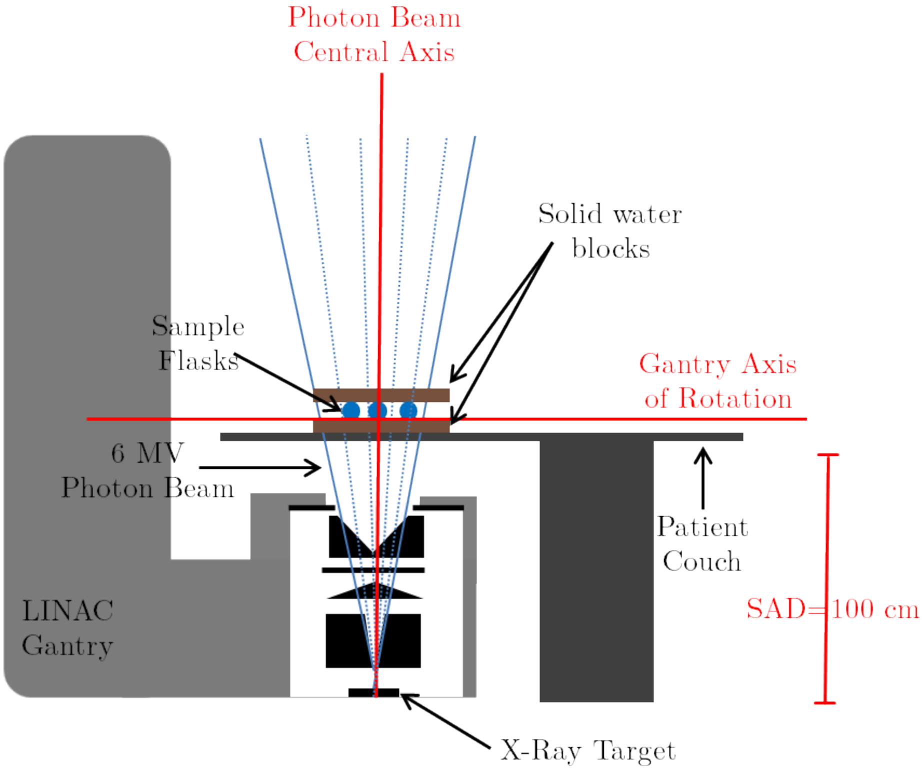

Figure 4.3: Linear accelerator (LINAC) set-up for cell irradiation. Abbreviations: SAD: Source to Axis Distance.

4.2.2 Single dose experiment schedule

Single fractions of 2 Gy, 4 Gy, 6 Gy, 8 Gy, 10 Gy, 30 Gy or 50 Gy were delivered to three flasks per dose. The remaining three flasks acted as control samples, receiving no radiation dose. One flask from each dose, and one control flask were harvested at each of 18, 42 and 66 hours post irradiation. A summary of this dose and harvesting schedule can be found in Table 4.4.

4.2.3 Cell harvesting for Raman microscopy

Each harvested flask was first washed with PBS and 3 mL trypsin was added to detach cells. Cells were then placed in an incubator at 37.0°C for 5 minutes. The trypsinized cells were mixed with 9 mL of media and transferred to a 50 mL conical tube. The cells were then centrifuged at 1500 rpm, for 5 minutes at 4°C. Supernatant was removed and the pellet was resuspended in 1 mL of fresh media.

Flask Number	**Total Dose**	**MU Delivered**	**Post Irradiation Time to Harvest**
1, 9, 17	0 Gy	0 MU	18h, 42h, 66h
2, 10, 18	2 Gy	197 MU	18h, 42h, 66h
3, 11, 19	4 Gy	394 MU	18h, 42h, 66h
4, 12, 20	6 Gy	591 MU	18h, 42h, 66h
5, 13, 21	8 Gy	788 MU	18h, 42h, 66h
6, 14, 22	10 Gy	985 MU	18h, 42h, 66h
7, 15, 23	30 Gy	2955 MU	18h, 42h, 66h
8, 16, 24	50 Gy	4925 MU	18h, 42h, 66h

Table 4.4: Single dose irradiation and harvesting schedule.

From the 1 mL cell suspension, 350 μL of cells were transferred to a 1.5 mL Eppendorf tube containing 300 μL of fresh media and centrifuged at 5000 rpm for 5 minutes at room temperature. The supernatant fluid was then removed, cells resuspended in 180 μL of a PBS + 3% FBS (by volume) solution and transferred to a 0.2 mL polymerase chain reaction (PCR) tube. Once again, cells were centrifuged at 5000 rpm for 5 minutes at room temperature and placed in an ice filled cooler for subsequent Raman data collection.

4.2.4 Cell viability and cell cycle assays

From the remaining cells in the original 1 mL suspension, several biological assays were also performed. First, 25 μL of cells were added to each of two 5 mL polystyrene round bottom tubes containing 325 μL of fresh media. To one of the two tubes, 1.5 μL of propidium iodide (PI) (Invitrogen, Eugene, OR, USA) was added and a 488 nm laser coupled with a BD FACSCalibur Fluoresence Activated Cell Sorter (FACS) (BD Biosciences, Missasauga, ON, Canada) was used to sample the proportion of viable cells in 20 000 cells from each population.

Furthermore, 50 μL of cells were placed in a 15 mL conical tube containing 950 μL of fresh media and centrifuged at 1500 rpm for 5 minutes, at 4°C. The supernatant liquid was poured off and cell pellet resuspended in 495 μL of 70% ethanol. To that, 5 μL of RNaseA (Qiagen Inc., Mississauga, ON, CA) and 27 μL of PI were added. This solution was left to rest for 25 minutes, after which it was centrifuged and resuspended in PBS spiked with 1% FBS. FACS was then used to measure the cell cycle distribution of 100 000 cells in the flask.

Approximately 50 μL of cells were added to a 15 mL conical tube containing enough fresh media such that the final concentration of cells in this liquid was between 10 000-500 000 cells/μL. An aliquot of 10 μL of Guava ViaCount reagent was added to the diluted cell solution and this was incubated for a total of 20 minutes upon which a Guava EasyCite 8HT flow cytometer (EMD Millipore, Billerica, MA, USA) was used to determine the concentration of viable cells in each flask using the ViaCount Assay.

All remaining cells were placed in a 1.5 mL Eppendorf tube containing 300 μL of media. This was centrifuged at 5000 rpm for 5 minutes then supernatant liquid poured off and pellet resuspended in 200 μL of PBS and centrifuged again. Supernatant PBS was poured off and warm lysate buffer which had been heated to 36.5°C was added to the cell pellet in a 2 (buffer) : 5 (cell) ratio. This was then heated and stirred for ten minutes, and immediately placed in a -80°C freezer. This stored solution has the potential to be used for future biological experiments of interest for the cell populations in this work.

4.3 Raman microscopy

4.3.1 The Raman microscope

Raman spectra were collected with a Renishaw inVia Raman Microscope (Renishaw Inc., Illinois, IL USA) coupled to a 100x dry objective (Leica Microsystems, Wetzlar, Germany) with NA of 0.9. The light source used was a 785 nm continuous wave diode laser with laser power measured at the sample to be 55 ± 5 mW (power density of 0.53 $\frac{\mathrm{mW}}{\mu\mathrm{m}^3}$). The laser sampling volume was measured to be $1.2 \pm 0.3\mu$m (along x-axis), $5.8 \pm 0.3\mu$m (along y-axis) and $14.8 \pm 0.5\mu$m (along z-axis); allowing the sample volume to be focused on a single cell at a time. All components associated with the spectrometer including microscope stage, laser/grating/filter combinations and spectral acquisition parameters were controlled by WiRE version 3.0 software package (Renishaw). An image of the Raman microscope, as well as the incident laser and scattered Raman signal paths are shown in Figure 4.4. The Raman excitation laser exits the laser source with dimensions of 5 x 2 mm^2 and passes through a beam expander which causes the laser spot to assume a circular shape of 5 mm diameter, matching the size of the back aperture of the 100x objective. This light is then reflected upward, onto a 785 nm high pass optical filter (Renishaw) which reflects 785 nm light and transmits light of wavelengths greater than 785 nm. The 785 nm light is then reflected in high purity to an upright microscope (Leica) focusing the laser light through the objective and onto the sample.

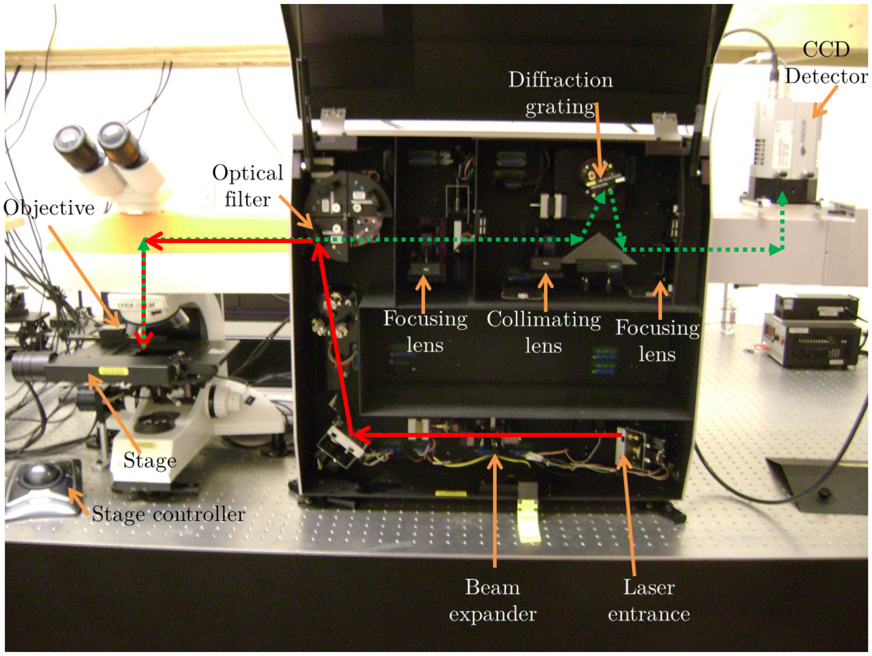

Figure 4.4: Raman microscope and the incident (red solid line) and scattered (green dotted line) light paths.

The sample is held in place on a linearly encoded motorized microscope stage (Prior Scientific Inc., Rockland, MA USA), see Figure 4.5. The spatial location of the sample stage can be controlled within 0.1 μm steps along the x, y and z directions.

Laser light incident on the sample is isotropically scattered and a portion of the scattered light is collected by the microscope objective and transmitted back through the optical filter where it is focused onto a 600 line/mm diffraction grating which spatially disperses the scattered light. The light is then focused along the dispersion axis of an Andor iDus DU-401A-BR-DD (back illuminated, deep depletion, single quartz window with anti-reflective coating optimized to 900 nm light) charge coupled device (CCD) detector (Andor Technology, Conneticut USA). To reduce thermal detector noise the CCD is cooled to -80 °C using a thermoelectric cooler, where the heat sink is treated with standard air cooling. The detector has dimensions of 1024 x 127 pixels, and pixel size of 26 x 26 μm^2. The dispersion axis of the detector is 1024 pixels wide, however the detector collection area along this axis is truncated to 600

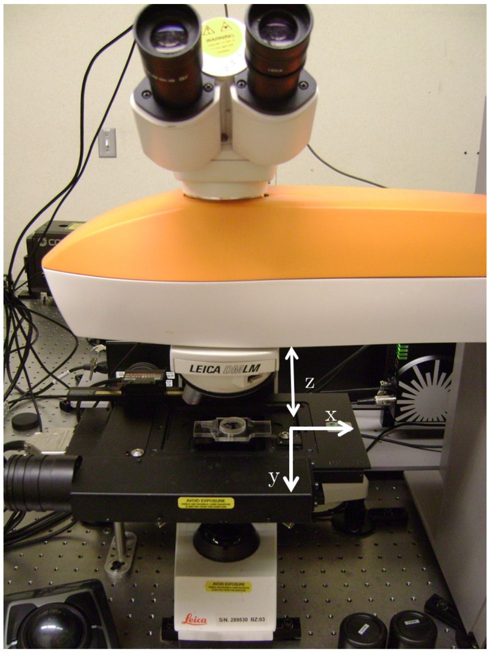

Figure 4.5: Sample holding stage and its degrees of freedom.

pixels. The detector collection area is centred at 1070.000 cm^{-1} making the spectral acquisition window from 423.570 cm^{-1} to 1819.520 cm^{-1}.

4.3.2 Spectral acquisition

The pelleted cell populations remained on ice for 1-4 hours prior to spectral acquisition. In preparation for spectral acquisition, individual populations were removed from the PCR tube and the supernatant was lifted away from the cell pellet. The cells were then evenly spread onto a MgF_2 disk (5 mm thick, Janos Technology Inc., Keene, NH, USA). Raman spectra were collected from plated cells within 2 hours of placing the cells on the MgF_2 disk.

A total of 480 spectra were collected per experiment over three days, with 8 populations per day and 20 spectra (one spectra per cell, total of twenty cells) per population. A variety of cell sizes, shapes and locations throughout the plated sample were probed. This minimizes biases which could potentially be introduced based on the selection of cells used to collect spectra. To minimize background debris contaminating the Raman signal, cells which do not appear to be obstructed by debris on upper and lower optical focal planes and only cells located on the upper layer of the splayed out sample on the MgF_2 disk are selected. Optical light is used

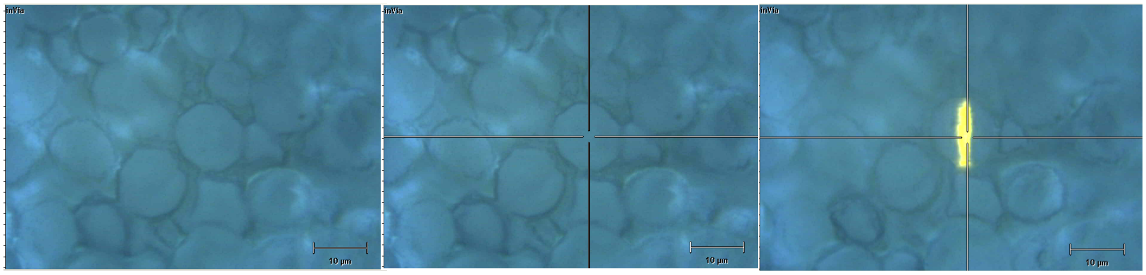

(a) (b) (c)

Figure 4.6: Cell selected for data collection (a), and focused along all spatial axes relative to the laser (b). Figure (c) shows the laser spot defining the sampling volume.

to adjust the z-axis position of the cell by visually aligning the upper surface of the cell to the focal plane of the instrument. The position of the cell relative to the laser is optimized in the x- and y-axes by positioning the laser cross hairs at the centre of the cell. The laser is then focused at a depth of 10μm below the cell surface by shifting the sample stage upward along the z-axis by 10μm after focusing the laser at the upper surface of the cell. A cell which meets selection requirements for data collection, has been focused along all spatial axes relative to the laser spot and the laser properly focused on the cell is depicted in Figure 4.6.

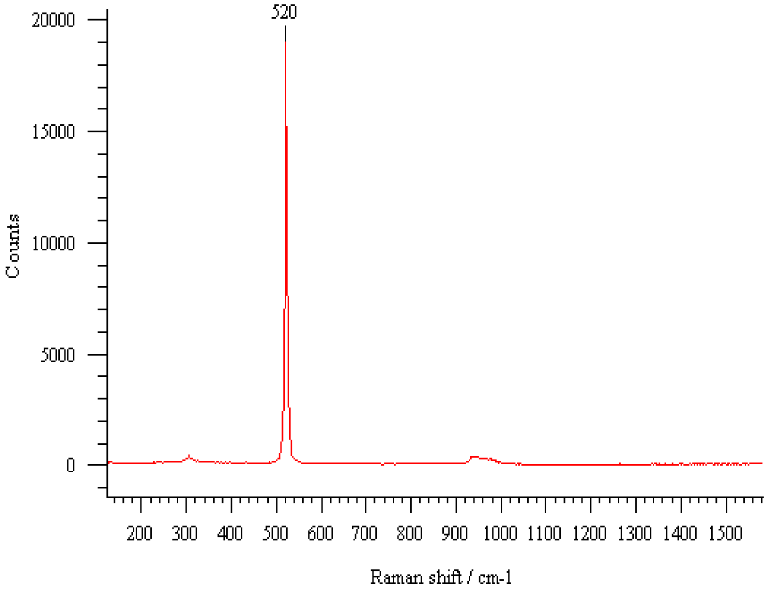

Figure 4.7: Silicon peak centered at 520.000 cm^{-1} used as a system check for the Raman system prior to data collection.

Careful control of the spectral acquisition parameters between cells, populations, experiment days and experiments is important for isolating spectral features which are a result of changes in cell responses rather than inconsistencies in data acquisition, and to ensure reproducible Raman measurements [156]. Control of laser/cell focusing, as well as laser power, exposure time, number of spectra collected, sample plating methods and the objective used are important for reproducible Raman measurements [156] [157] [158] and as such, these parameters were kept consistent for each experiment.

Spectra were collected using 100% laser power (55 ± 5 mW). Data for all experiments were collected within a two month period, therefore any significant degradation in laser power within that time is considered negligible. As a check prior to data collection for each population, a silicon reference spectrum centered at 520.000 ±0.500 cm^{-1} is collected, as shown in Figure 4.7. Any obvious problems in laser alignment or system alignment which would affect laser intensity at the sample would be reflected in this reference silicon peak intensity and location. The average initial silicon peak intensity over all experiments was 19000 counts ± 9% and the average silicon peak location was $520.252 \pm 0.119\ \mathrm{cm}^{-1}$, suggesting that the laser power at the sample was relatively consistent throughout all experiments. Prior to data acquisition the cell is exposed to 10 seconds of photobleaching where the cell is irradiated with 100% laser power in order to quench background fluorescence before the spectrum is acquired. Following photobleaching, the cell is exposed to 100% laser power for 10 seconds and the spectrum is simultaneously recorded with the CCD detector. A summary of data acquisition parameters kept consistent throughout all experiments are listed in Table 4.5.

The number of dead cells encountered when collecting spectra is dependent on the fraction of viable cells in that specific sample (appendix B). When spectra with characteristics that represent a dead cell [59] were encountered, the spectrum was discarded and a new cell selected for acquisition. Spectra with cosmic ray contamination occurred in 5% of spectra collected. Spectra with abnormally high background fluorescence were encountered in 0.6% of spectra collected. In both cases the abnormal spectra were discarded, and a new cell was selected for acquisition.

Acquisition Parameter	Default Setting
Number of spectra collected per sample	20
Number of samples per day	8
Number of days per experiment	3
Total spectra per experiment	480
Sample storage conditions	On ice (maximum 4 hours)
Number of cells per sample†	$20.6 \times 10^6 \pm 2\%$ (H460) $28.5 \times 10^6 \pm 15\%$ (MCF-7) $4.4 \times 10^6 \pm 2\%$ (MDA-MB-231) $10.3 \times 10^6 \pm 30\%$ (LNCaP)
Sample preparation	Technique described in section 4.2.1
Spectral region	423.570 cm^{-1} to 1819.520 cm^{-1}
Detector resolution	2.3 cm^{-1}
Objective	100x
Aperture size	5 mm
Laser/cell focus	Technique described in section 4.3.2
Photobleaching laser power	100%
Photobleaching duration	10s
Excitation laser power	100%
Spectral acquisition duration	10s

Table 4.5: Raman spectral acquisition parameters. †Absolute cell counts in 0 Gy flask, four days after plating (first day of harvesting in experiment) averaged over two experiments with three independent measures per experiment; n=6.

4.4 Spectral processing

After all 480 spectra are collected for an experiment, the spectra are batch processed to remove background biological fluorescence, normalize the spectra, shift spectra to account for system drifts during data acquisition and isolate correlated spectral features using PCA. Programs were developed using Matlab version 7.12.0.635 R2011a (Mathworks Inc., Natick, MA, USA) to carry out these tasks.

4.4.1 Background fluorescence removal

Unaltered Raman spectra of biological materials are composed of the Raman signatures superimposed with a fluorescence spectrum resulting from fluorescence of the many organic molecules intrinsic to the sample volume as well as any presence of MgF_2 disk in the sample volume. The intensity of the background biological fluorescence is dependent on the amount of biological material and MgF_2 disk present in the sample volume and will vary from cell to cell. Background removal is necessary to remove the resulting source of variability between spectra that these differences can create.

Background fluorescence gives rise to the low frequency structure of the raw spectrum. In order to remove this component of the raw spectrum, a Savitsky-Golay filter is used to provide an initial estimate of the baseline (BL) of the spectrum. This filter is based on a generalized moving average [159] where the coefficients of the filter are determined by linear least-squares regression to fit the data points within a window of interest, to a polynomial of 1^{st} order. The size of the filter window is selected to be 7% of the total length of the spectral data set (see next paragraph for discussion of this). This gives an initial threshold to classify the spectral data as either signal or BL based on whether a given data point is above or below the estimated BL, respectively. The estimated BL is then used to modify the raw spectrum data set such that data points larger than the estimated baseline are set to the value of the BL at that point. The BL is then re-estimated based on the modified data set. This allows conformation of the estimated BL to the low-frequency structure of the background without the high frequency Raman signals influencing the BL estimate [80]. The BL fitting process is reiterated 20 times, as this level of re-iteration converged on an overall BL fit for the data. The estimated BL is then subtracted from the raw spectrum, leaving a spectrum with significantly less biological fluorescence contamination. An example of a raw and BL corrected spectrum are shown in Figure 4.8.

Selection of the Savistsky-Golay filter window must be carefully considered for optimal BL estimation. The size of the filter window affects curvature of the BL estimate; a large filter window (ex. 7% of the data range) gives a low curvature BL estimate and a small filter window (ex. 1% of the data range) gives a high curvature BL estimate. The filter window size was optimized to a value of 7% by visually selecting the size which best balances between avoiding an overestimate of the BL while avoiding an underestimate in the curvature of the BL. Figure 4.8 demonstrates the effect of window size on BL estimate.

4.4.2 Spectral normalization

Following removal of background fluorescence absolute intensity differences of Raman spectral features must be accounted for by spectral normalization. The quantity of

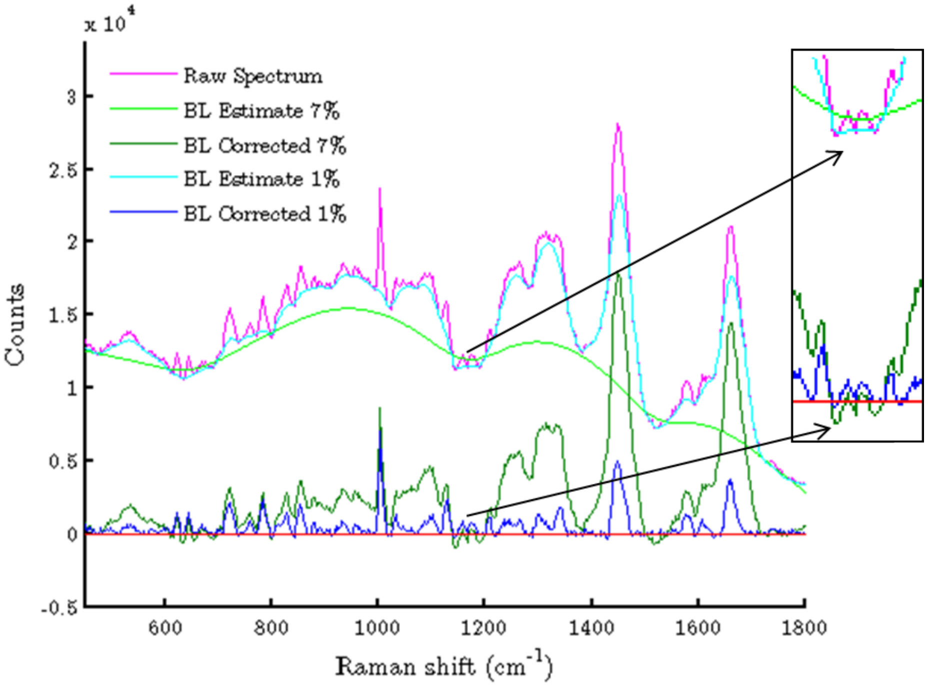

Figure 4.8: Raw spectrum (magenta) and baseline (BL) corrected spectrum (dark green) using the Savitsky-Golay BL estimate technique (7% window size was used for processing the work presented in this thesis). BL estimate and corrected spectrum for a 1% filter window size is also shown for comparison. Inset illustrates a spectral region where using 7% window size slightly over estimates the biological fluorescence (due to the lower curvature of the BL for this window size) as a trade-off for avoiding the drastic over estimate of the rest of the spectrum obtained with using a 1% window size.

biological material in a given sample volume as well as minor fluctuations in laser output power and Raman system alignment can effect the absolute intensity of Raman peaks. Individual spectra are normalized to the total area under the baseline corrected spectrum.

4.4.3 Spectral shifting

Prior to data collection for each sample, a reference silicon spectrum is collected. The details of this process are discussed in section 4.3.2. Spectra are collected if the silicon peak is measured to have a Raman shift of 520.000 ± 0.500 cm^{-1}, however slight drifts of the Raman system during data acquisition can result in slight drifts in the Raman shift read out by the detector for a given peak. The difference in Raman shift before and after data acquisition for one sample was 0.08 cm^{-1} ± 0.14 cm^{-1} on average and never exceeded 0.959 cm^{-1}. In order to eliminate any drift in Raman shifts for a given experiment, all 480 spectra are aligned relative to the first spectrum in the data set. The first spectrum was arbitrarily picked, and ultimately any one of the spectra within the data set could have been used as the reference spectrum for shifting.

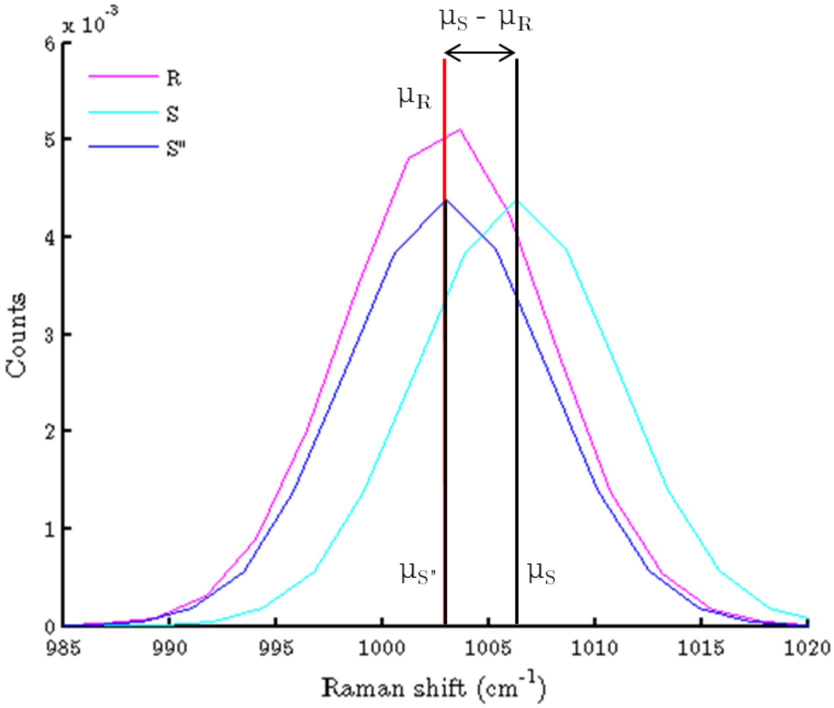

Figure 4.9: Result of spectral shifting; before shift (S), after shift (S'') and reference spectrum (R).

First, the sharp phenylalanine Raman peak centred around 1004 cm^{-1} is isolated and fit to a Gaussian distribution for both the reference spectrum (R) and the spectrum to be shifted (S). The mean of the Gaussian distribution (μ) for each S spectrum is individually compared to the mean of the phenylalanine peak fit for R. The difference between the centre of the Gaussian for R and S is used to define the required shifting magnitude (which was always less than half a pixel) and direction. The intensity values for S are interpolated between subsequent pixels at a resolution of 0.01, for the entire range of wavelengths in the spectrum. To shift S to higher wavenumbers (R's phenylalanine peak greater than S's peak), the interpolation occurs between intensity values assigned to pixel $(i-1)$ and i (where i refers to pixel index in the array containing all intensity values for S). To shift S to lower wavenumbers (R's phenylalanine peak less than S's peak), the interpolation occurs between pixels $(i+1)$ and i. The interpolation yields a 100 data point model of the Raman spectrum between the two pixels. The new shifted data set (S') at pixel i is filled with the interpolated value which is the appropriate shifting magnitude between the two pixels. This interpolation and shift is repeated for all pixels in S. The last pixel in S can not be filled by interpolated data because of the finite size of S, hence this pixel is filled with intensity data from the pixel adjacent to it. The process of fitting the phenylalanine peak, interpolating and shifting is repeated on S' relative to R creating S''. The net result of this shifting process is a set of intensity data (S'') which is shifted relative to the original data set (S), but maintains the same spectral shape and features and is aligned with R. Figure 4.9 illustrates this shifting process by comparing the mean phenylalanine peak position for an intensity data set to the reference spectrum for that experiment.

4.4.4 Data analysis

Following collection of Raman data and spectral processing, analysis is carried out using PCA as described in chapter 3, section 3.3. PCA is used to identify trends in the Raman spectra as a function of dose and time post irradiation. The main interest of this work is to investigate the feasibility of using Raman spectroscopy to detect dose-dependent responses in individual cells at doses which are clinically relevant to the first few fractions of a RT patient's treatment. This typically means doses less than 10 Gy (see chapter 1, section 1.4.2). As such, PCA was first run on only the 0, 2, 4, 6, 8 and 10 Gy populations (referred to herein as the low dose experiment) in each of the three days of an experiment. PCA was then run on the full data set (0, 2, 4, 6, 8, 10, 30 and 50 Gy, referred to herein as the high dose experiment). Results from the high dose experiment are intended to be used to bolster results obtained with the low dose experiment. PCA isolates correlated Raman peaks within a spectrum (determine the PCs), and scores the degree of expression of that PC for the entire data set. Programs were developed using Matlab to perform this analysis. Following from the technical description of PCA in section 3.3, the data set submitted to Matlab for analysis consisted of an $n \times p$ array made up of n samples ($i = 1, ..., n$) corresponding to the spectra in a given data set (low or high) and p measurements ($j = 1, ..., p$) corresponding to the number of data points in a single spectrum.

Following PCA the Matlab program outputs a total of $n - 1$ PCs and the corresponding component scores for each cell. The component scores for each population are represented by the mean component score of the cells in that population with the uncertainty on that value being the standard error. These mean component scores are plotted as a function of dose and time post irradiation in what is referred to herein as a score plot, an example of which is shown in chapter 5, Figure 5.2b.

In order to determine if the differences in mean PC scores between two populations are statistically significant, the two sample t-test is used. This tests the null hypothesis that the two PC score means being compared are independent random samples from a normal distribution with equal means and equal variances. If this null hypothesis is disproved, the two PC score means come from normal distributions with unequal means, i.e the scores represent two different distributions. This null hypothesis is tested to a 5% significance level. The p-value for this result is also returned. A p-value describes the probability of obtaining a t-test result at least as extreme as that which was returned. If the two sample t-test's null hypothesis is disproved with a p-value of ≤ 0.05 then the difference between the two mean PC scores is statistically significant, and so the two populations represented by these means are significantly shifted relative to one another.

To better elucidate statistically significant trends in the data sets, each mean component score is assigned either a square or star data point marker. A square marker indicates that the mean score of that population is significantly different from the control population. A star data point indicates that the mean score of the population is not significantly different from the control population. The 0 Gy populations at 42 and 66 hours post irradiation are compared to the 0 Gy, 18 hour control population to monitor any component score trends which would be independent of dose. For each time point (18, 42 or 66 hours) the irradiated populations are compared to the 0 Gy population for that time point. As an example, the 50 Gy population harvested at 66 hours post irradiation is compared to the 0 Gy, 66 hour population and the 0 Gy, 66 hour population is compared to the 0 Gy, 18 hour population.

Chapter 5

Results & Discussion I: H460 cell line

5.1 General considerations

For each of the four cell lines studied, two identical full experiments (0, 2, 4, 6, 8, 10, 30 and 50 Gy populations) have been performed. Only one representative experiment is presented in this work, however repeating the experiment for a second time yielded highly reproducible results (in terms of the trends observed in the score plots as well as the components which emerged from the data set) for all cell lines. Reproducibility between the two experiments was evaluated by calculating the Pearson's r-value to indicate correlation (r-value=1) or anti-correlation (r-value=-1). Only those components with Pearson's r-values greater than $r=\pm0.75$ when comparing it to a similar component in the second experiment are considered highly reproducible and are reported in this work. This r-value threshold was determined based on subjective experience in how well the features between two components agree with one another, and their corresponding r-values. Furthermore, components below 1% of the total variance are not considered since below this threshold the components contain little to no features which can be interpreted as Raman peaks and rather contain mostly high frequency noise.

5.2 Significance of principal components

In order to demonstrate that the principal components obtained following PCA do represent Raman spectral features, spectra from two independent cells are shown in Figure 5.1. Cell #468 and #469 are both from the 50 Gy, 66 hour harvesting population of the H460 experiment. From Figure 5.1 it is clear that the general features of Raman spectra of individual cells are similar; as discussed in chapter 2, section 2.2 the biochemical content from one cell to the next will remain relatively consistent. In addition to the common features between the two cell spectra shown in Figure 5.1 there are some noticeable differences in some of the peak intensities and peak content (ex. around 480 cm^{-1}). The visible differences in Raman spectra between these two cells is a result of inherent differences in the biochemical content of these cells. The biochemical content of an individual cell will depend on many factors such as cell cycle position or cell response to external stressors like radiation damage or starvation.

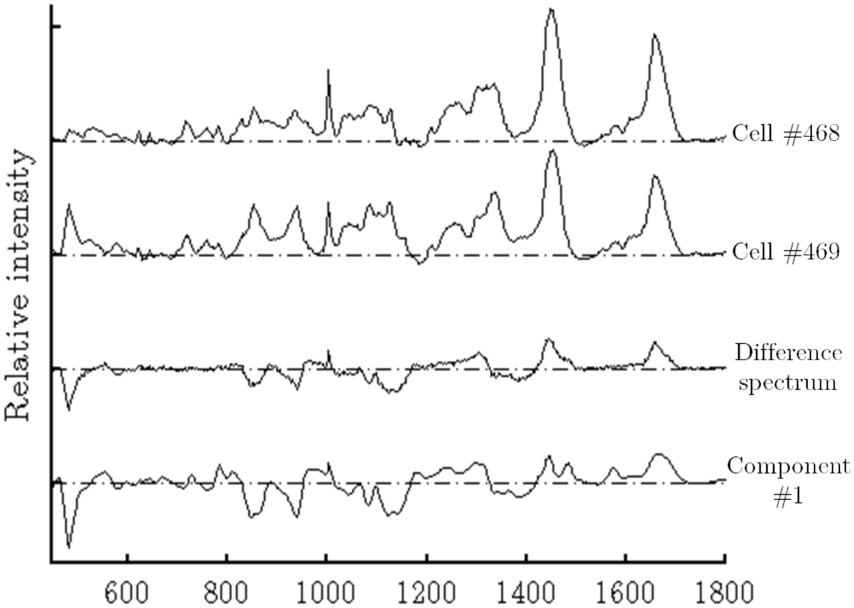

Figure 5.1: Raman spectra of two cells (cell #468 & #469) from the 50 Gy, 66 hour H460 population illustrating spectral differences between cells in the same population resulting from differing biochemical content in cells. The difference spectrum between cell #468 and #469 is also shown for comparison with component 1 of the H460 experiment.

One of these cells has a positive score while the other has a negative score for component 1; cell #468 has a score of 1.02×10^{-3} and cell #469 has a score of -1.79×10^{-2}. Relative to the other cells in this data set these two cells have drastically different scores. The difference spectrum found by subtracting the Raman spectrum of cell #469 from cell #468 is shown in Figure 5.1 and shows the main feature differences between the Raman spectrum of these two cells. The difference spectrum suggests that cell #469 contains higher intensity Raman peaks as illustrated by the negative features of the difference spectrum and cell #468 contains higher intensity Raman peaks at the positive features of the difference spectrum. Comparison of the difference spectrum to component 1 of the H460 experiment (shown in Figure 5.1, full experiment presented in section 5.4) shows that the major spectral differences between cell #468 and #469 are represented by component 1. Therefore it can be concluded that the components obtained using PCA as described in this work represent variability in Raman spectral features (and hence biochemical content) between the various cell spectra collected for an experiment. Also, the component score for cell #469 was a (relatively) large negative value in comparison to cell #468 and the corresponding difference spectrum did show that cell #469 contains more of the negative features of component 1 compared to cell #468. This suggests that the component scores accurately mirror the relative expression of each component for a given cell.

The information provided in this and the previous section applies to all four cell lines studied.

5.3 Population characteristics

The H460 cell line used in this experiment presented its self as a robust cell line compared to the other lines used. The growth kinetics for the H460 cells were fast, requiring the largest splitting ratio (see chapter 4, section 4.1.2) out of all the cell lines used and this cell line tends to form distinct colonies in the flask. The H460 cell line also has the second highest average literature reported SF_2 value (SF_2=0.64, chapter 4, section 4.1.1) compared to the other three cell lines explored.

5.4 Raman experiment results

Both the low and high dose H460 Raman data sets consist of three components with percent variances larger than 1%. All three of these components were highly reproducible (r-values > 0.97) between the two independent experiments for this line. Components 1 and 2 represented recognizable biochemical changes or relevant dose and time dependent trends and will be presented here. Component 3 will not be discussed in any detail in this thesis and can be found in appendix D.

Component 1

Component 1 accounts for 54.9% of the total variance in the low dose data set and 59.6% of the total variance in the high dose data set. Component 1 of the high dose data set is identical to that of the low dose experiment with an r-value of 1.00 ± 0.03%.

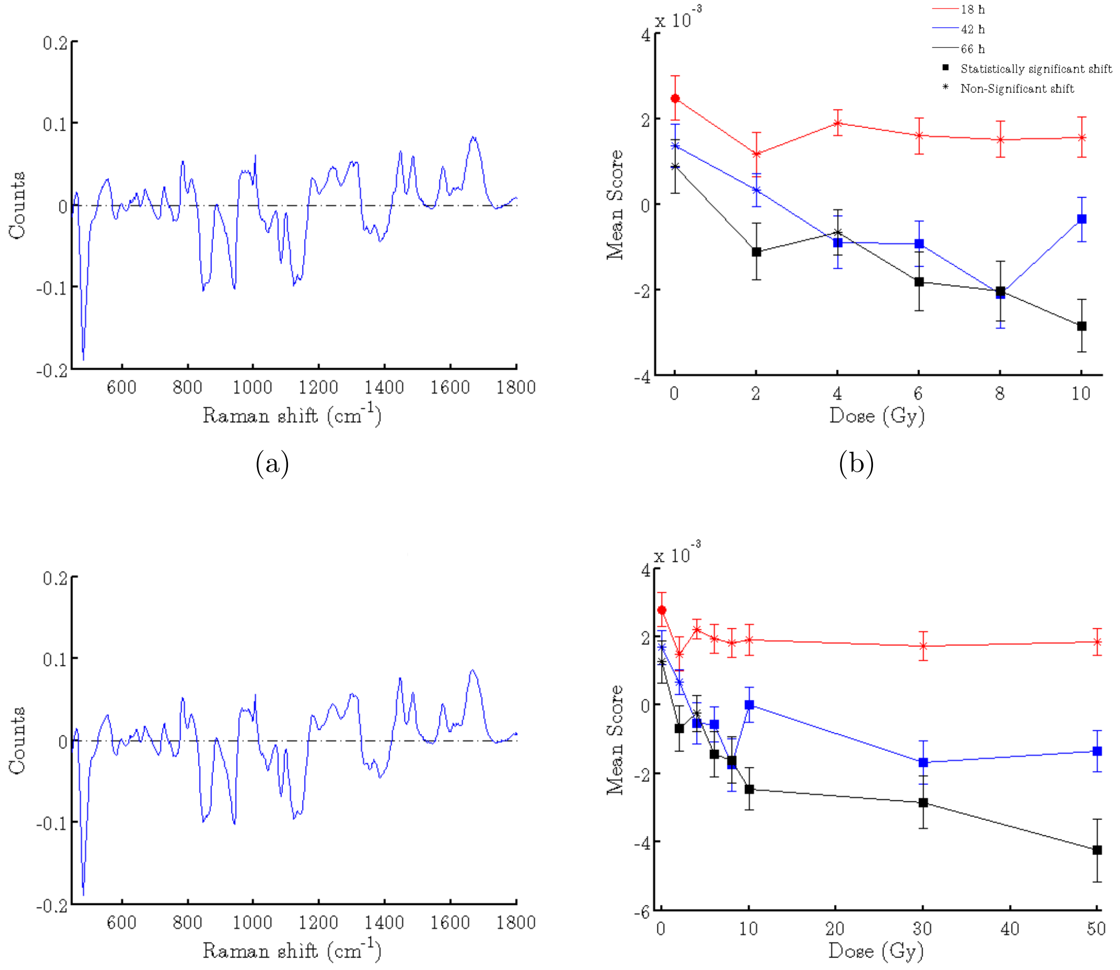

(a)

(b)

(c)

(d)

Figure 5.2: Component 1 and corresponding score plot for the H460 low dose data set (a) & (b) and the high dose data set (c) & (d).

Component 2

Component 2 accounts for 18.3% of the total variance in the low dose data set and 16.0% of the total variance in the high dose data set. Component 2 of the high dose data set is identical to that of the low dose data set with an r-value of 1.00 ± 0.03%.

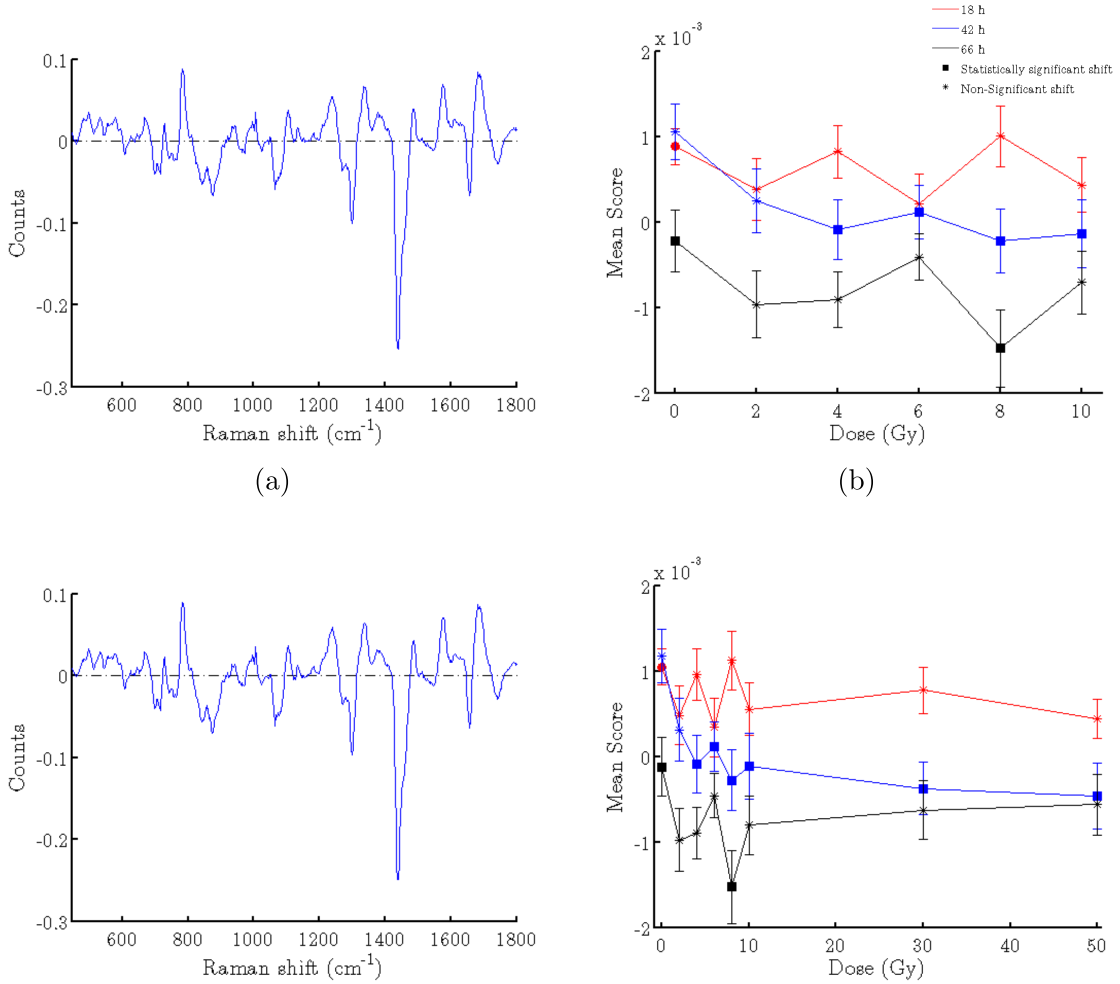

(a) (b)

(c) (d)

Figure 5.3: Component 2 and corresponding score plot for the H460 low dose data set (a) & (b) and the high dose data set (c) & (d).

5.5 Discussion

5.5.1 Cell cycle Raman component

Peaks making up component 2 can be described as originating from mostly nucleic acid, protein and lipid structures. The major peaks contributing to this component are labeled for the high dose experiment in Figure 5.4 and the corresponding molecular assignments are listed in Table 5.1. The nature of a given peak in the component, whether it be from nucleic acid, protein, lipid or carbohydrate is indicated on the figure in order to elucidate the nature of contributing molecular features.

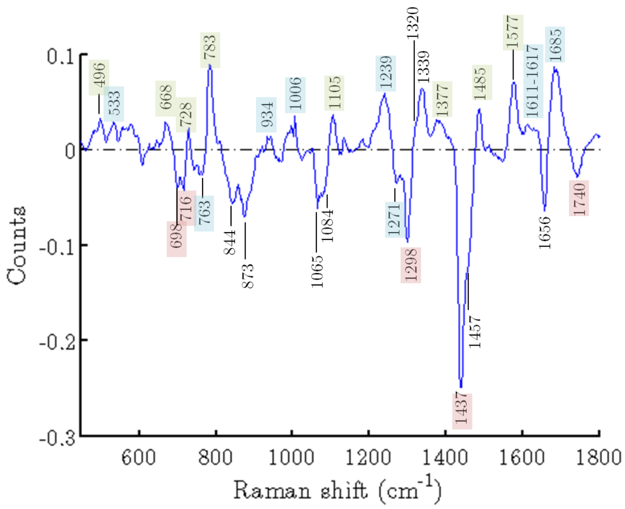

Figure 5.4: Cell cycle component (component 2) with major peaks labeled for H460 high dose experiment. Peaks arising from nucleic acids are shown in green, protein in blue, lipid in pink and carbohydrate in purple. Table 5.1 gives assignments for these peaks.

This component is a result of variations in the protein, nucleic acid and lipid content between individual cells. Positive features indicated in Figure 5.4 are mainly composed of protein and nucleic acid Raman shifts. In the 490-950 cm^{-1} range the most dominant (highest number of counts) feature is at 783 cm^{-1} and arises from ring bending modes in thymine, uracil and cytosine vibrations and symmetric stretching in the phosphate backbone of nucleic acids. In the 1000-1400 cm^{-1} range the dominant features are from protein and nucleic acid vibrations, including the amide III band. From 1400-1750 cm^{-1} the main contributors to the positive features of this component include the bases guanine and adenine at 1485 cm^{-1} and 1577 cm^{-1} and the Amide I band for proteins with β sheet configuration at 1685 cm^{-1}.

Negative features of this component, as indicated in Figure 5.4, mainly arise from lipid molecular vibrations. Between 490-950 cm^{-1} major contributions are a result of nucleic acid backbone and the protein tyrosine, as well as features from the lipids cholesterol and choline. From 1000-1400 cm^{-1} the negative features of this component mainly arise from CH_2 deformation and twisting on lipid species occurring around 1298 cm^{-1}. The most dominant contribution to the negative features of this component occur at 1437 cm^{-1} and are a result of CH_2 deformations in lipid species. A very similar component to that shown in Figure 5.4 has been identified in the literature which contains the same positive nucleic acid and protein features and negative lipid features [160]. Matthews et al. describe this component as arising from differences in the biochemical content of individual cells as a result of being at different stages in progression through the cell cycle [160]. Therefore in the presented H460 experiment component 2 represents variations in biochemical content between cells in different phases of the cell cycle.

	Assignment			
Raman shift (cm^{-1})	**Nucleic Acid**	**Protein**	**Lipid**	**Carb.**
496	G,T[150]			
533		S-S str.[161]		
668	G,T,[150],[162] A[162]			
698			Ch.[150]	
716			Cho.[150]	
728	A[59]			
760		trp.[150]		
783	U, C T rb.[59] O-P-O sym. str.[153]			
817-900	O-P-O str.[59]	tyr.[150],[161]		
934		C-C str. α[150]		
1006		Phe. rb.[163],[59]		
1065-1084		C-N str.[59]	C-C[150]	C-O str.[59]
1105	PO_2^- sym. str.[95],[161]			

Continued ...

Table 5.1: Raman peak assignment for H460 cell cycle component. Only main contributors of a band are listed.

Table 5.1 continued ...

	Assignment			
Raman shift ($\mathbf{cm^{-1}}$)	**Nucleic Acid**	**Protein**	**Lipid**	**Carb.**
1230-1244		am. III rc am. III β[59]		
1271		am. III α[95]		
1298			CH_2 def.[161] CH_2 tw.[150],[95]	
1320	G[59]	CH def.[59]		
1339	A,G[59]	CH def.[59]		
1377	T[150]			
1437			CH_2 def. [150]	
1457		CH_2 def.[95]	CH_2 def.[95]	
1485	G[150],[153] A[153]			
1577	G,A[150]			
1611		tyr.,[95] phe.[59]		
1617		tyr., trp.[59]		
1656		am. I α[95]	C=C[95]	
1685		am. I β[95]		
1740			C=O[95]	

Table 5.1: Raman peak assignment for H460 cell cycle component. Only main contributors of a band are listed. Abbreviations: A: adenine, C: cytosine, T: thymine, G: guanine, U: uracil, trp: tryptophan, phe: phenylalanine, carb: carbohydrate, am: amide, tyr: tyrosine, ch: cholesterol, cho: choline, str: stretch, sym: symmetric, def: deformation, tw: twist, rb: ring breathing, rc: random coil, α: α helix, β: β sheet.

The H460 cell cycle component contributes 18.3% and 16.0% of the total variance to the low and high dose data sets, respectively. The cell cycle score plots for the H460 cell line in Figures 5.3b and 5.3d show a trend towards increasingly negative scores in the 0 Gy population at 66 hours post irradiation compared to 18 hours post irradiation. This trend is related to a reduction in the nucleic acid and protein feature intensities relative to lipid features for the cells probed in this population, on average, with time post irradiation. Continued proliferation in the control populations from 18 to 66 hours post irradiation leads to the increase in absolute cell count (viable + dead) observed in the 66 hour control population as shown in appendix C, Figure C.1, relative to the control populations at 42 and 18 hours post irradiation. Continued proliferative activity would lead to a full flask of cells causing the cells to reach a plateau in proliferation. Short et al. describe a plateau cell population as one with over 80% of cells in G1 phase [60]. The 0 Gy, 66 hour H460 population does have a large portion of cells in G1, as can be seen in appendix A, Figure A.1. Short et al. describe cells in plateau phase as possessing lower quantities of nucleic acid and protein relative to lipid, as is observed for the H460 66 hour control population in the more negative mean scores in Figures 5.3b and 5.3d.

At 18 hours post irradiation there is little difference in component score for the control population compared to any of the irradiated populations. At 42 hours post irradiation a difference in the component scores emerges between the control and irradiated populations, specifically for 4 Gy and higher. While this shift is statistically significant, within the quoted uncertainty it is minor. At 66 hours post irradiation there is a trend towards increasingly negative cell cycle component scores as a function of dose however the shift in score from control to irradiated population is not statistically significant.

5.5.2 Radiation-induced Raman component

Component 1 contributes 54.9% of the total variance in the low dose data set and represents a large portion of the biochemical changes occurring in H460 cells. The score plot for this component indicates a strongly dose-dependent trend, while there is no statistically significant shift in the 0 Gy populations at 42 and 66 hours post irradiation relative to the 0 Gy 18 hour population. Component 1 from the low dose data set is shown in Figure 5.5a with Raman shifts assigned to major peaks contributing to the component. The molecular assignment of these Raman peaks are listed in Table 5.2.

The majority of positive features in component 1 originate from protein and nucleic acid contributions. In the 450-850 cm^{-1} range, the main component feature at 783 cm^{-1} originates from cytosine and uracil ring stretching. From 950-1100 cm^{-1} major positive features arise from carbon bond stretching modes and deoxyribose between 955-994 cm^{-1}, and phenylalanine symmetric ring breathing at 1004 cm^{-1}. Nucleic

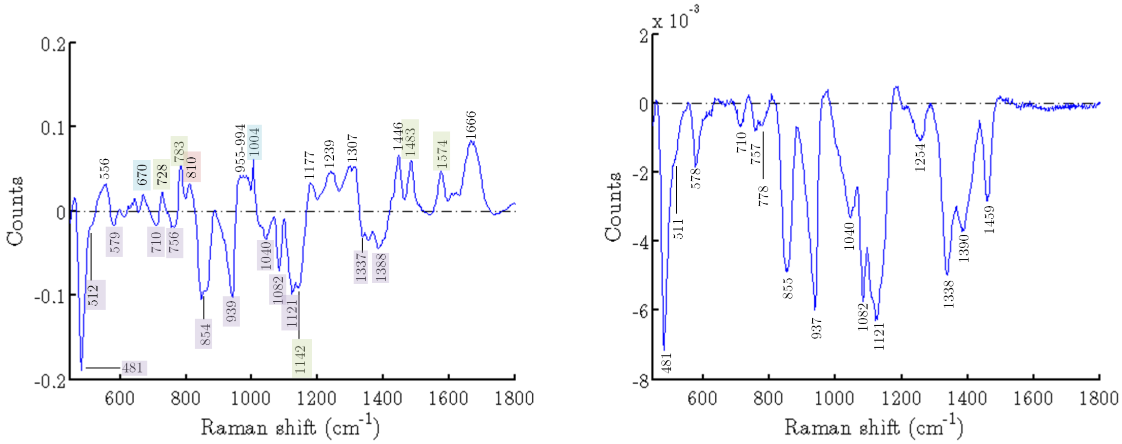

(a) (b)

Figure 5.5: H460 low dose component 1 with major peaks labeled in 5.5a. Peaks arising from nucleic acids are shown in green, protein in blue, lipid in pink and carbohydrate in purple. Table 5.2 gives assignments for these peaks. The Raman spectrum of pure glycogen is shown in 5.5b with major peaks labeled.

acids thymine, cytosine and adenine as well as protein contributions through tyrosine, and carbon hydrogen bond deformation contribute to positive features between 1177-1307 cm^{-1}. The peak at 1239 cm^{-1} arises from the C-N stretching mode of proteins in β sheet conformation. Other major peaks contributing to the positive features of component 1 include carbon hydrogen bond deformations in protein and lipid at 1446 cm^{-1} as well as guanine, adenine, thymine and cytosine contributions between 1483-1666 cm^{-1}.

While the positive features in component 1 originate from a variety of protein and nucleic acid molecular vibrations, the negative features of component 1 almost entirely originate from a single molecule: glycogen. The only exception to this is the possible contribution from deoxyribose and adenine in DNA at 1142 cm^{-1}, however the spectrum of pure glycogen (Figure 5.5b) shows a broad peak around 1121-1142 cm^{-1} so the peak at 1142 cm^{-1} in component 1 may also be purely from glycogen. Taking a look at the pure glycogen spectrum in Figure 5.5b, one can easily identify the striking similarity between pure glycogen and the negative features of component 1 shown in Figure 5.5a.

	Assignment			
Raman shift (cm^{-1})	**Nucleic Acid**	**Protein**	**Lipid**	**Carb.**
481				Glyc.
512				Glyc.
579				Glyc.
670		cys. S-S str. [77]		
710				Glyc.
728	A[150]			
756				Glyc.
783	C,U ring str.[161]			
810			O-P-O[59]	
854				Glyc.
939				Glyc.
955-994	d.[162]	C-C str.[162]	C-C[59]	
1004		Phe. sym. rb.[59]		
1040				Glyc.
1082				Glyc.
1121				Glyc.
1142	d., A[162]			
1177	T, C[162]	tyr.[162]		
1239	T[162]	am. III β[59]		
1307	A[58]	CH def.[58]	CH2 tw.[59]	
1337				Glyc.
1388				Glyc.
1446		CH def.[59]	CH def.[59]	
1483	G[150]			
1574	G, A[150]			
1666	T, C, G[162]	am. I[162]		

Table 5.2: Raman peak assignment for H460 component 1. Only main contributors of a band are listed. Abbreviations: A: adenine, C: cytosine, T: thymine, G: guanine, U: uracil, d: deoxyribose, cys: cystine, carb: carbohydrate, am: amide, tyr: tyrosine, glyc: glycogen, str: stretch, sym: symmetric, def: deformation, tw: twist, rb: ring breathing, β: β sheet.

Trends in component 1 expression

The score plots for component 1 of the low dose experiment indicate no statistically significant shift between the 0 Gy populations at 18, 42 or 66 hours post irradiation. At 18 hours post irradiation there is no statistically significant shift between the unirradiated and irradiated populations. As time post irradiation increases there becomes a statistically significant shift between irradiated and unirradiated populations. Namely, at 42 hours post irradiation populations receiving doses of 4 Gy or higher are significantly shifted from the 0 Gy population. At 66 hours post irradiation populations receiving doses as low as 2 Gy are significantly shifted towards more negative mean scores. This shift in irradiated populations with time post irradiation suggests that in response to radiation, cells appear to be accumulating glycogen. This conclusion can be made because the irradiated populations shift towards increasingly negative mean scores which means the individual spectra for cells in those populations contain a larger proportion of negative features of component 1. Based on the interpretation of the molecular vibrations contributing to component 1 presented in Table 5.2, it is apparent that the negative features represent glycogen and as such these cells contain larger amounts of glycogen than their unirradiated counterparts. Therefore it can be concluded that using RS as described for this work in combination with PCA allows for identification of an accumulation of glycogen in H460 cells as a function of dose, for doses as low as 2 Gy.

With reference to the score plot for component 1 of the high dose data set (Figure 5.2d), a similar trend to that found in the low dose data set (Figure 5.2b) can be observed in the 30 and 50 Gy populations as well. At 18 hours post irradiation there is no significant shift between the 30 or 50 Gy populations and the 0 Gy population for that day, however at 42 and 66 hours post irradiation there is a significant shift towards more negative mean scores. This suggests that there is an important factor of time which must be considered for observing a radiation-induced response in the irradiated H460 populations and may be due to a required initiation of a radiation response pathway (be it a radioresistance or cell death pathway) and subsequent accumulation of glycogen following initiation of this pathway.

Another important observation is that the 30 and 50 Gy populations in the high dose score plot are further shifted towards negative mean scores relative to even the 10 Gy populations for that day. It can also be noted that while the 2 Gy population at 66 hours post irradiation is shifted from the 0 Gy population, it is not as shifted as the 6 Gy population, which is not as shifted as the 10 Gy or 50 Gy population. This suggests not only an accumulation of glycogen in response to exposure to radiation but also a dose-dependent accumulation of glycogen such that the degree of accumulation appears to increase with dose.

Identification of dose-dependent spectral features at low doses

In both the low dose and high dose data set, component 1 is nearly identical with an r-value of 1.00 ±0.03% meaning the addition of the high dose data is not required to pick out a dose-dependent component in the H460 cell lines. While shifts in mean score for the 50 Gy population relative to the 0 Gy population are more drastic than for the 2 Gy population at the same harvesting time, the fact that the low dose populations also have a significant shift in mean score compared to the unirradiated samples means these dose-dependent responses can be detected in an *in vitro* environment with only low doses of radiation. Since the radiation-induced response to express increased levels of glycogen is significant in the H460 cell line (54.9% and 59.6% of the total variance in low and high dose experiments respectively), PCA can be used to identify the radiation-induced component in a data set containing doses below 10 Gy. However, the addition of the high dose data (10 and 50 Gy) is valuable in illustrating further the dose-dependent trend in component 1.

Biological justification

The scope of this thesis is to evaluate the use of RS to identify dose-dependent biochemical changes in various cell lines at low doses. However, in support of the conclusion that H460 cell response to radiation results in glycogen accumulation, a possible biological response pathway to radiation which could result in increased glycogen content is discussed in brief here. Brognard et al. have demonstrated the important role of the Akt/PKB (protein kinase B) pathway in promoting cell survival upon exposure to ionizing radiation in non-small cell lung cancers such as the H460 cell line [164]. A result of Akt signaling is the inhibition through phosphorylation of GSK-3β (glycogen synthase kinase 3 beta) which in turn causes the inability to inhibit glycogen synthase (GS) [165]. GS promotes glycogen synthesis in the cell, and as such regulation of glycogen synthesis can be affected by the pro-survival Akt/PKB signaling. This possible pro-survival cellular response pathway may be a contributing factor to the observed accumulation of glycogen in irradiated H460 populations. Validation of the role of this response mechanism in causing the observed glycogen accumulation in Raman spectra of irradiated cells is underway and is beyond the scope of this thesis.

Chapter 6

Results & Discussion II: MCF-7 Experiment

6.1 Population characteristics and viability

The MCF-7 cell line used in this experiment was a robust cell line compared to the others. This cell line proliferated at the second quickest rate (behind the H460 line), requiring the second largest splitting ratio (see chapter 4, section 4.1.2) out of all the cell lines used. Like the H460 cell line, the MCF-7 cells form well defined colonies. The average literature reported SF_2 value for MCF-7 cells is identical to that of the H460 line (SF_2=0.64, chapter 4, section 4.1.1).

6.2 Raman experiment results

Both the low and high dose MCF-7 Raman data sets consist of four components with percent variances larger than 1%. In the low dose data set, all four of these components were reproducible (r-values > 0.75) between the two independent MCF-7 experiments however components 3 and 4 had r-values of 0.88 ± 2% and 0.75 ± 5% respectively while components 1 and 2 had better reproducibility with r-values of 0.99 ± 0.1% and 0.99 ± 0.2% respectively. Similarly, all four components in the high dose data set were reproducible (r-values > 0.75) between the two independent MCF-7 experiments however components 3 and 4 had r-values of 0.79 ± 4% and 0.85 ± 2% respectively while components 1 and 2 had better reproducibility with r-values of 0.99 ± 0.1% and 0.99 ± 0.2% respectively. Components 1, 2 and 3 represented recognizable biochemical changes or relevant dose and time dependent trends and will be presented here, while component 4 did not and can be found in appendix D.

Component 1

Component 1 accounts for 58.5% of the total variance in the low dose data set and 62.9% of the total variance in the high dose data set. Component 1 of the high dose data set is highly correlated to that of the low dose experiment with an r-value of 0.99 ± 0.2%.

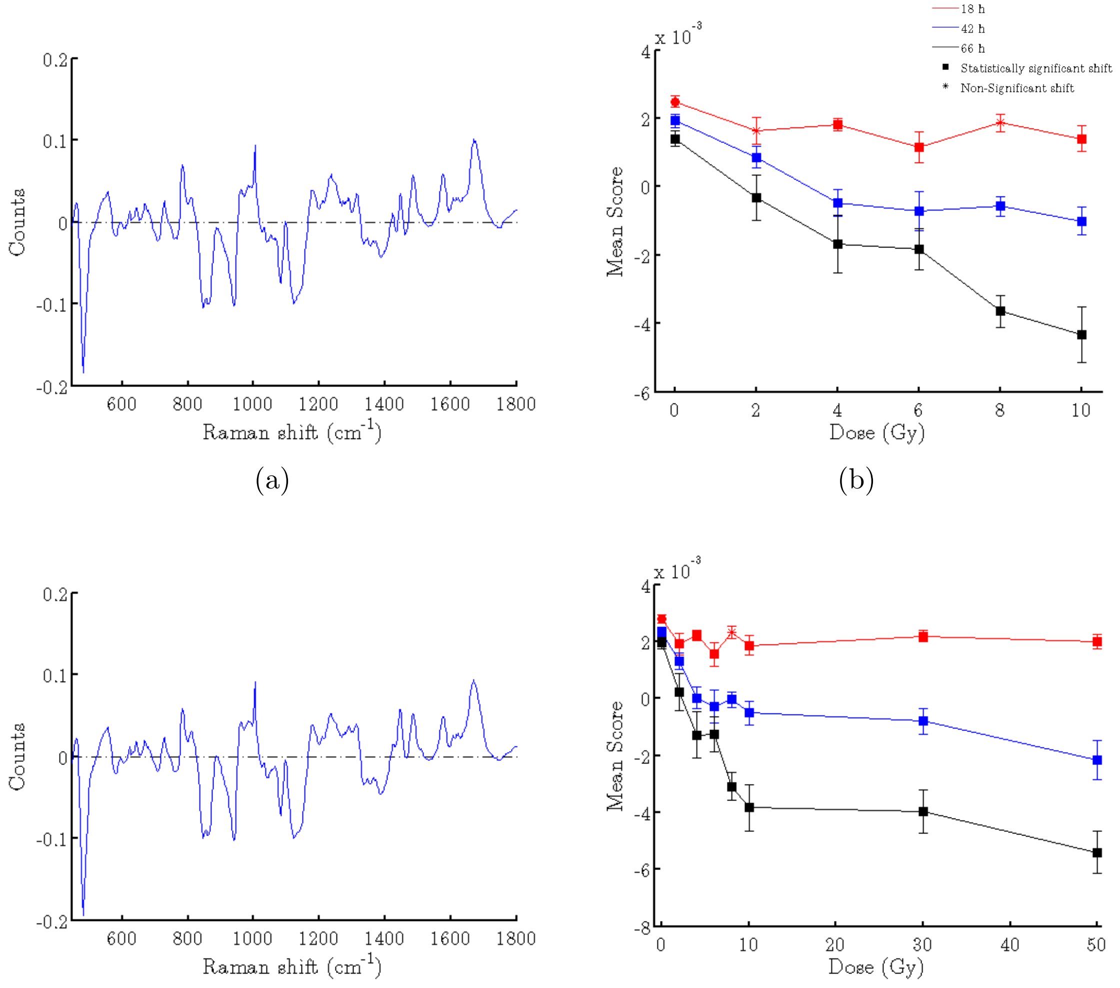

(a) (b)

(c) (d)

Figure 6.1: Component 1 and corresponding score plot for the MCF-7 low dose data set (a) & (b) and high dose data set (c) & (d).

Component 2

Component 2 accounts for 16.2% of the total variance in the low dose data set and 15.8% of the total variance in the high dose data set. Component 2 of the high dose data set is highly correlated to that of the low dose data set with an r-value of 0.99 ± 0.2%.

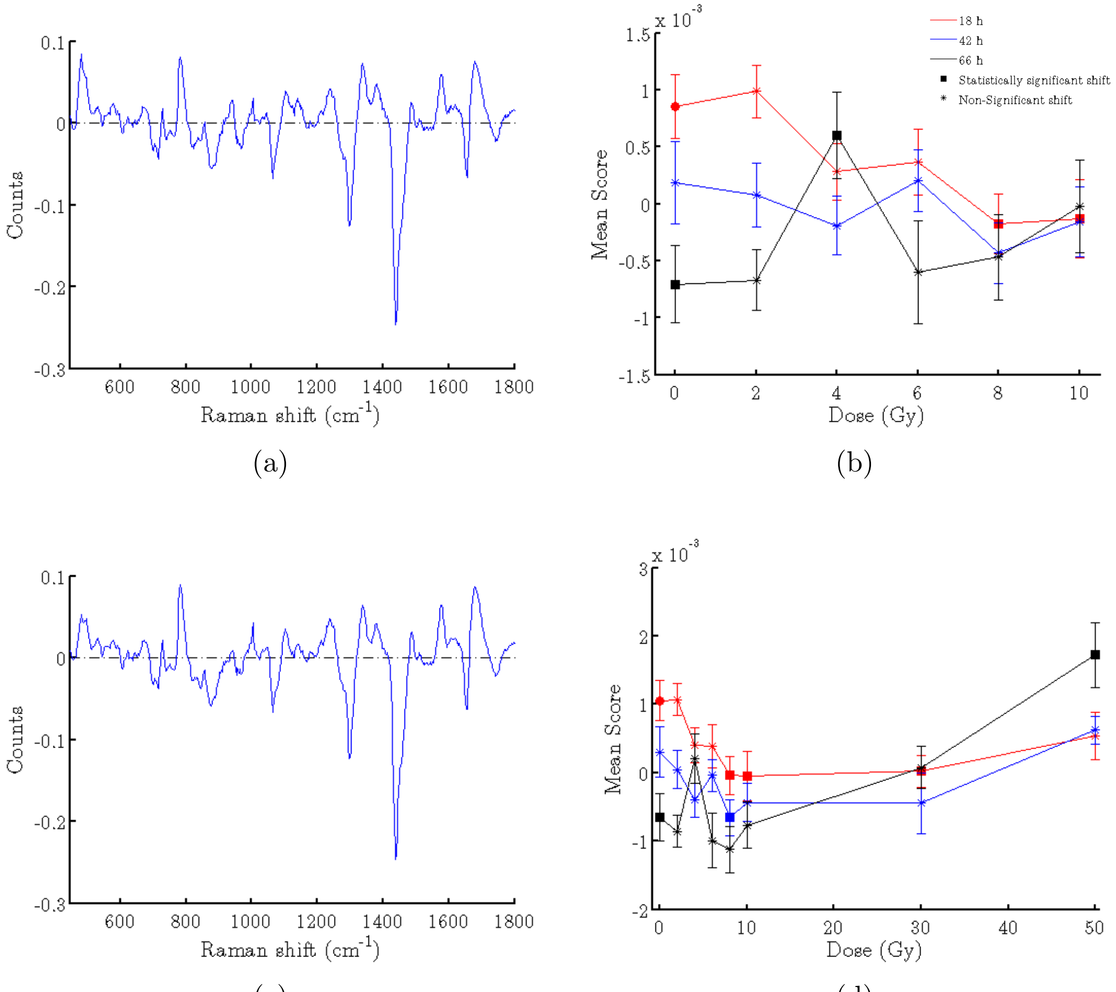

(a) (b)

(c) (d)

Figure 6.2: Component 2 and corresponding score plot for the MCF-7 low dose data set (a) & (b) and high dose data set (c) & (d).

Component 3

Component 3 accounts for 3.3% of the total variance in the low dose data set and is highly correlated to component 4 of the high dose data set, with an r-value of 0.99 ± 0.2%. Component 4 of the high dose data set accounts for 2.6% of the total variance in that data set.

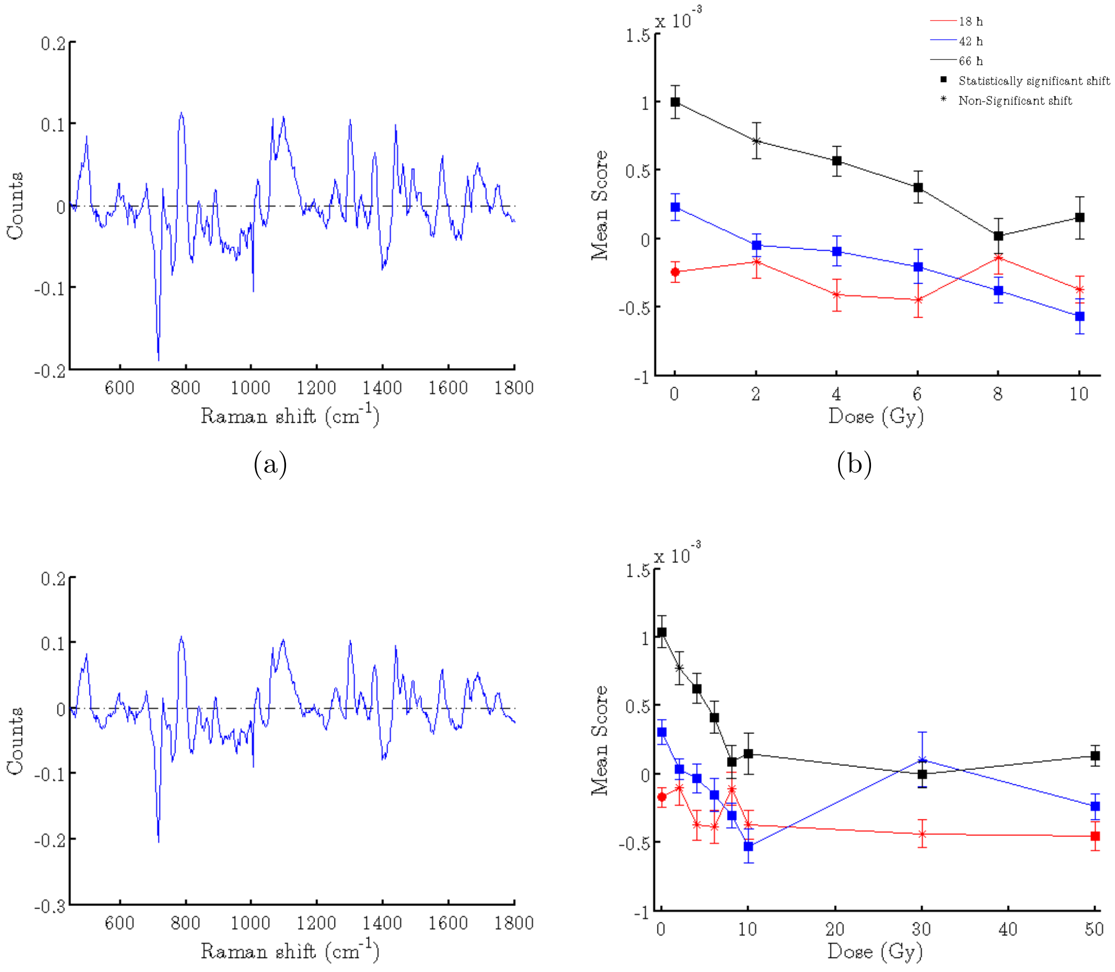

(a) (b)

(c) (d)

Figure 6.3: Component 3 and corresponding score plot for the MCF-7 low dose data set (a) & (b) as well as the highly correlated component 4 of the high dose data set (c) & (d).

6.3 Discussion

6.3.1 Cell cycle Raman component

With a correlation r-value of 0.97 ± 0.5%, component 2 of the MCF-7 high dose data set (Figure 6.2c) is highly correlated to the cell cycle component identified for the H460 experiment (Figure 5.3a). The peak content in both the H460 and MCF-7 cell cycle components are nearly identical with minor differences arising from variations in peak intensities. Therefore, it is concluded that component 2 in the MCF-7 experiment describes variability in the data set as a result of differences in protein and nucleic acid cell content relative to lipid content as a result of cell cycle distributions. The MCF-7 cell cycle component contributes to 16.3% and 15.8% of the total variance in the low and high dose data sets, respectively.

The peak assignment for component 2 is identical to that for the H460 cell cycle component shown in chapter 5, Figure 5.4, with some minor additional peaks as listed in Table 6.1.

	Assignment			
Raman shift (cm^{-1})	**Nucleic Acid**	**Protein**	**Lipid**	**Carb.**
480				Glyc.[166]
954		C-C bnd. α[167] CH_3 rk. [167]		
967	PO_3^{2-} str.[95]			

Table 6.1: Raman peak assignment for additional peaks found in the MCF-7 cell cycle component. Only main contributors of a band are listed. Abbreviations: carb: carbohydrate, glyc: glycogen, str: stretch, bnd: bend, rk: rocking, α: α helix.

The cell cycle score plots for the MCF-7 cell line (Figure 6.2b & 6.2d) show a trend towards more negative scores in both the control and irradiated populations ($<$ 2 Gy) at 66 hours post irradiation relative to 18 or 42 hours post irradiation, however within uncertainty this shift is minor. This is indicative of a reduction in nucleic acid and protein feature intensities relative to lipid content for the cells harvested at 66 hours post irradiation. This shift towards more negative scores could be an indication of more cells in early G1 following mitosis [160] and may be indicative of continued proliferation in these samples from 18 hours to 66 hours post irradiation. This hypothesis is in agreement with the observed increase in total number of cells (viable+dead) in the 42 and 66 hour control and 2 Gy populations relative to the 18 hour populations (appendix C, Figure C.2).

There is no reportable trend in cell cycle component scores as a function of dose relative to the controls for any of the three harvesting times post irradiation at doses less than 10 Gy. However, a statistically significant increase in cell cycle component score in the 50 Gy population and non-significant but noticeable increase in the 30 Gy population relative to the 0 Gy population is observed at 66 hours post irradiation.

This suggests an increase in the nucleic acid and protein features relative to lipid features for the 50 Gy population's cell spectra, on average. Cell cycle distributions for this line (appendix A, Figure A.2) show an increase in the number of cells in G2 relative to the controls for the 50 Gy and even 30 Gy populations at 66 hours post irradiation. As described in Matthews et al. cells in late G2/M tend to express more protein and nucleic acid relative to lipid and hence should posses an increasingly positive mean score in this phase [160]. This trend is in agreement with what is observed in the cell cycle trends from both FACS (appendix A, Figure A.2) and the cell cycle Raman component scores for this line (Figures 6.2b & 6.2d).

6.3.2 Radiation-induced Raman component

Component 1 contributes to the majority (58.5%) of the total variance in the low dose data set. The score plot for component 1 indicates a strongly dose-dependent trend with minor shifts in the 0 Gy populations at 42 and 66 hours post irradiation compared to the 0 Gy, 18 hour population. Component 1 from the low dose data set is shown in Figure 6.4 with Raman shifts assigned to major peaks contributing to the component. The molecular assignment of these Raman peaks are listed in Table 6.2.

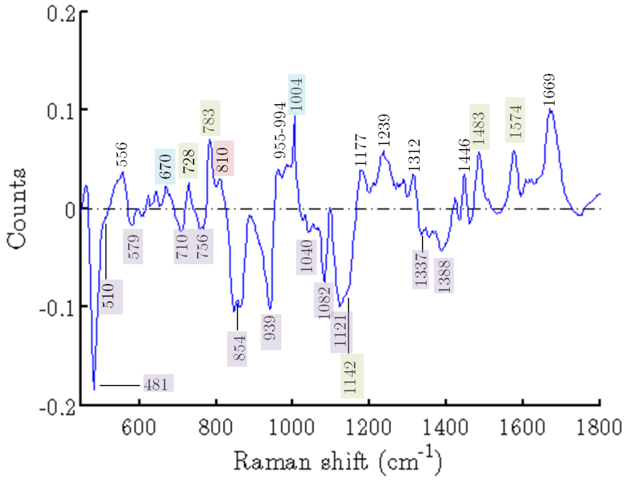

Figure 6.4: MCF-7 low dose component 1 with major peaks labeled. Peaks arising from nucleic acids are shown in green, protein in blue, lipid in pink and carbohydrate in purple. Table 6.2 gives assignments for these peaks.

Positive features in component 1 originate from nucleic acid and protein molecular vibrations as well as some lipid contributions. In the 450-850 cm^{-1} range major con-

	Assignment			
Raman shift (cm^{-1})	**Nucleic Acid**	**Protein**	**Lipid**	**Carb.**
481				Glyc.
510				Glyc.
579				Glyc.
670		cys. S-S str. [77]		
710				Glyc.
728	A[150]			
756				Glyc.
783	C,U ring str.[161]			
810			O-P-O[59]	
854				Glyc.
939				Glyc.
955-994	d.[162]	C-C str.[162]	C-C[59]	
1004		Phe. sym. rb.[59]		
1040				Glyc.
1082				Glyc.
1121				Glyc.
1142	d., A[162]			
1177	T, C[162]	tyr.[162]		
1239	T[162]	am. III β[59]		
1312		CH_3CH_2 tw.[77]	CH_3CH_2 tw.[77]	
1337				Glyc.
1388				Glyc.
1446		CH def.[59]	CH def.[59]	
1483	G[150]			
1574	G, A[150]			
1669	T, C, G[162]	am. I[162]		

Table 6.2: Raman peak assignment for MCF-7 component 1 of the low dose experiment. Only main contributors of a band are listed. Abbreviations: A: adenine, C: cytosine, T: thymine, G: guanine, U: uracil, d: deoxyribose, cys: cystine, phe: phenylalanine, carb: carbohydrate, am: amide, tyr: tyrosine, glyc: glycogen, str: stretch, sym: symmetric, def: deformation, tw: twist, rb: ring breathing, β: β sheet.

tributing positive features originate from cytosine and uracil ring stretching modes at 783 cm^{-1} and lipid PO_2 vibrational modes at 810 cm^{-1}. Dominant positive features between 950-1100 cm^{-1} arise from carbon bond stretching modes in protein and lipid, as well as DNA deoxyribose vibrational modes and phenylalanine symmetric ring breathing. Between 1100 and 1312 cm^{-1} major contributions arise from cytosine and thymine. Protein contributions from tyrosine at 1177 cm^{-1} and amide III band at 1239 cm^{-1} are also major contributors to the positive features in component 1. Between 1400-1670 cm^{-1} major contributions from guanine, adenine, thymine and cytosine as well as protein C=O stretching modes (amide I band) contribute to the positive features. Much like component 1 of the H460 cell line, component 1 in the MCF-7 experiment has negative features entirely originating from glycogen. Comparison of the negative features in Figure 6.4 to the Raman spectrum of pure glycogen (chapter 5, Figure 5.5b) indicates similarity between the two. Based on the molecular origins of the MCF-7 component 1, it is clear that this component is nearly identical (r-value=0.98 ±0.3%) to the dose-dependent component 1 found in the H460 experiment.

Trends in component 1 expression

Since positive features of component 1 are of nucleic acid, protein and lipid molecular origin, populations with positive mean scores in the score plot for component 1 (Figure 6.1a) of the low dose experiment correspond to a cell with inherently higher content of these biomolecules relative to glycogen. Conversely, a population with a negative mean score has a large portion of cells with an inherently high level of glycogen relative to nucleic acid, protein and lipid. The score plot for component 1 shows that there is a significant shift towards a more negative mean score between 0 Gy populations at 42 and 66 hours post irradiation relative to that at 18 hours post irradiation. This suggests that as time in culture increases, the MCF-7 cells are producing more glycogen relative to nucleic acid, protein and lipids. The low dose score plot indicates that at 18 hours post irradiation there is a significant shift towards more negative mean scores in populations receiving 4, 6 and 10 Gy of radiation relative to the controls. At 42 and 66 hours post irradiation all irradiated populations exhibit a significant shift towards negative mean scores.

In the high dose data set, component 1 is nearly identical (r-value=0.99 ± 0.2%) to that for the low dose data set. Minor variations exist in the form of peak intensity differences, while the nature of the peaks remains the same. The high dose score plot shows a similar dose-dependent response in the 30 and 50 Gy populations to that observed for doses below 10 Gy. At 18, 42 and 66 hours post irradiation both the 30 and 50 Gy populations are significantly shifted towards more negative mean scores. This indicates that these populations are accumulating glycogen to a greater extent than their unirradiated counterparts.

Although the 0 Gy populations do shift towards more negative mean scores the shift of the irradiated populations relative to the 0 Gy populations at 42 and 66 hours post irradiation is much larger. Furthermore, the magnitude of shift of the 50 Gy population is greater than that of the 10 Gy population, which is larger than the 2 Gy population, indicating a definite dose-dependent accumulation of glycogen as well. This suggests that MCF-7 cells accumulate glycogen in response to cell density in the flask (shifted 0 Gy populations with time), but also as a response to radiation (shift in irradiated populations relative to 0 Gy populations). While component 1 is not purely radiation-induced there is certainly a dose-dependent trend in the accumulation of glycogen much like was observed in the H460 cell line.

Identification of dose-dependent spectral features at low doses

Component 1 contributes to the majority of the total variance in the low dose data set (58.5%), therefore the high dose data set is not required to facilitate identifying the accumulation of glycogen in the MCF-7 cells. While the shift in mean score from the unirradiated to 2 Gy population is not as drastic as the 50 Gy population, the shift is still significant and it is clear that by 10 Gy at 66 hours post irradiation the magnitude of shift begins to plateau and becomes less drastic in moving to the 50 Gy population. This suggests that even at low doses the glycogen response in the cells as a function of dose is quite significant and stands out within the data set of all other biochemical changes occurring in the sampled cells for the entire experiment. The heterogeneity in glycogen content between irradiated and unirradiated cell populations is distinct enough that RS can be used to identify this response even at doses below 10 Gy. Because of the strong nature of glycogen accumulation even at low doses, the first component models this trend and it can be concluded that RS can be used in combination with PCA to identify dose-dependent responses in MCF-7 cells to radiation for doses as low as 2 Gy with a data set containing doses below 10 Gy. This is indicative that RS is sensitive enough to detect this dose-dependent response at early time points in a typical radiation dosing schedule for a patient.

Biological justification

Mourant et al. have used Fourier transform infrared spectroscopy to study protein, glycogen and lipid content for cell populations in exponential and plateau growth phases [168]. It was found that the protein to glycogen ratio decreases in a plateau-phase versus exponential growth phase population. This is an example of a environment induced state of stress resulting in accumulation of glycogen in cells, and is a potential explanation for the shift towards negative mean scores for the 0 Gy populations at 42 and 66 hours post irradiation relative to 18 hours. Referencing the plot of total cell count in each population (appendix C, Figure C.2), the total number of cells increased by 33% from 18 to 42 hours in the 0 Gy population, however there is a slight reduction in total cell count by 1% from 42 to 66 hours. This is an indication that the cell population may have reached the plateau phase and halted exponential division due to overcrowding. This overcrowding would cause competition for nutrients in the flask and may initiate survival mechanisms such as the Akt/PKB pathway [169], which result in an accumulation of glycogen.

The Akt/PKB pathway has also been shown to play a role in responses to ionizing radiation in a variety of carcinomas and particularly breast carcinomas [170]. As such, cellular stresses resulting from both nutrient deprivation and radiation damage could potentially initiate accumulation of glycogen. The trends observed in the component 1 score plot indicating accumulation of glycogen for both 0 Gy populations as a function of harvesting time, and irradiated populations relative to unirradiated population may be a superposition of both stressors on the observed populations. Biological validation of this pathway is beyond the scope of this thesis however it is important to recognize that possible biological explanations for the observed trends do exist. Validation of the role of the Akt/PKB pathway in causing the observed glycogen accumulation in Raman spectra of irradiated cells should be made before any firm conclusions on the contribution of this pathway are established.

Further evidence that the accumulation of glycogen due to overpopulation may be occurring in this sample can be found in comparing the dose-dependent component of the MCF-7 and H460 data sets. Increased glycogen content can be found in both the irradiated and unirradiated (although to a lesser extent) MCF-7 populations. In the H460 experiment there was no accumulation of glycogen in the 0 Gy populations as a function of time post irradiation. By comparing the total number of cells in the 0 Gy populations for the H460 and MCF-7 experiments (appendix C, Figures C.1 and C.2) it is clear that the absolute number of cells initially plated in the MCF-7 experiment must have been much higher than that for the H460 experiment. At 18 hours post irradiation the 0 Gy H460 population contained 2.08×10^7 cells, while the MCF-7 0 Gy population contained 3.79×10^7 cells indicating that the MCF-7 populations contained a larger number of cells to share the same amount of media and nutrients compared to the H460 populations. Therefore, it can be expected that there would be increased nutrient starvation in the MCF-7 line which may have contributed to the accumulation of glycogen in the 0 Gy populations in this line as compared to the H460 line. This fact could also be a possible explanation as to why the MCF-7 populations began showing significant shifts in component 1 mean scores at lower doses sooner, compared to the H460 line.

Chapter 7

Results & Discussion III: MDA-MB-231 Experiment

7.1 Population characteristics

Growth kinetics for the MDA-MB-231 cell line are not as rapid as the H460 or MCF-7 lines, but are quicker than the LNCaP line as reflected in the splitting ratio (see chapter 4, section 4.1.2). This cell line did not appear to form distinct colonies in the flask like the H460 or MCF-7 lines, rather the cells appeared much more migratory. The MDA-MB-231 cell line has the highest average literature reported SF_2 value (SF_2=0.71, chapter 4, section 4.1.1) compared to the other three cell lines explored.

7.2 Raman experiment results

Both the low and high dose MDA-MB-231 Raman data sets consist of seven components with percent variances larger than 1%. In the low dose data set, four of the seven components were reproducible (r-values > 0.75) between the two independent MDA-MB-231 experiments. Component 1 was highly reproducible with an r-value of 0.99 ± 1%, while components 2, 3 and 4 were less reproducible with r-values of 0.86 ± 3%, 0.80 ± 3% and 0.85 ± 3% respectively. In the high dose data set, six of the seven components were reproducible (r-values > 0.75) between the two independent MDA-MB-231 experiments. Components 1, 2, 3 and 4 were highly reproducible with r-values of 0.99 ± 0.1%, 0.98 ± 0.3%, 0.92 ± 2% and 0.93 ± 1% respectively, while components 5 and 6 were less reproducible with r-values of 0.77 ± 5% and

0.83 ± 3% respectively. Components 1, 2 and 3 represented recognizable biochemical changes or relevant dose and time dependent trends and will be presented here, while components 4, 5 and 6 did not and can be found in appendix D.

Component 1

Component 1 accounts for 44.5% of the total variance in the low dose data set and 43.1% of the total variance in the high dose data set. With an r-value of 1.00 ± 0.01%, component 1 of the high dose data set is identical to that in the low dose data set.

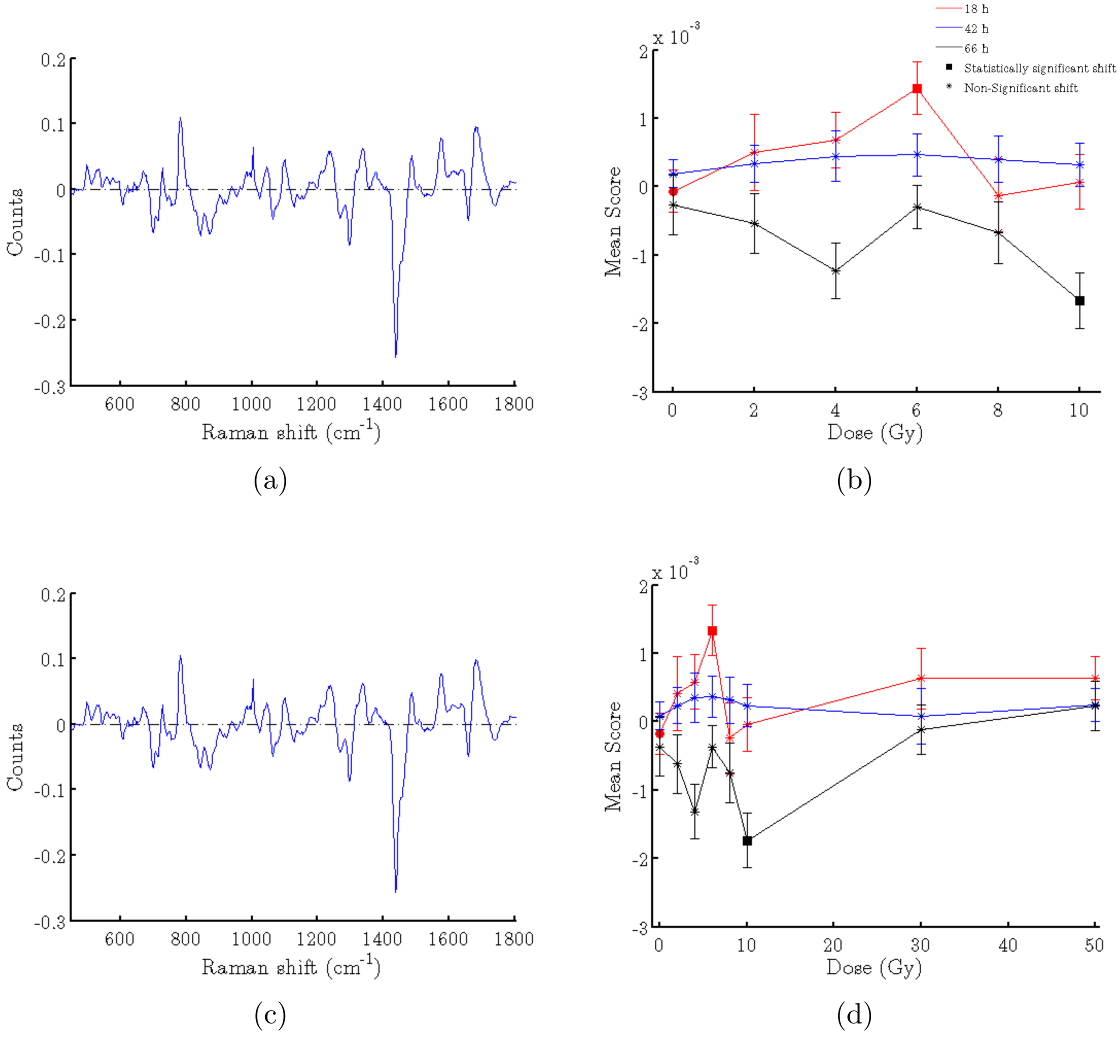

(a) (b)

(c) (d)

Figure 7.1: Component 1 and corresponding score plot for the MDA-MB-231 low dose data set (a) & (b) and high dose data set (c) & (d).

Component 2

Component 2 accounts for 9.0% of the total variance in the low dose data set. Component 2 of the high dose data set accounts for 10.1% of the total variance and appears to be a combination of both components 2 and 3 of the low dose experiment. Pearson's r-values describing the similarity of component 2 of the high dose experiment with components 2 and 3 of the low dose experiment are 0.76 ± 5% and 0.63 ± 8% respectively. These r-values show that this component is most similar to component 2 of the low dose experiment.

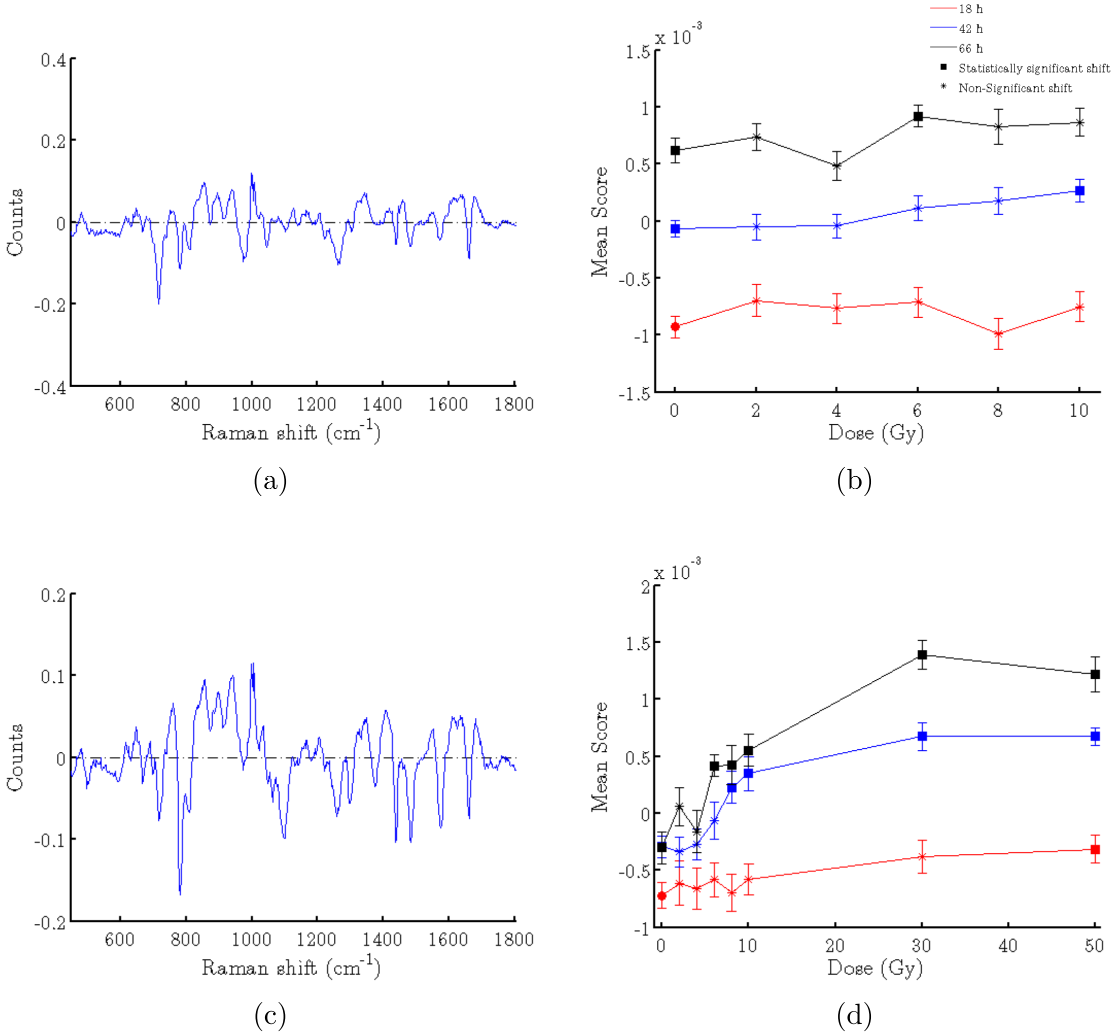

(a) (b)

(c) (d)

Figure 7.2: Component 2 and corresponding score plot for the MDA-MB-231 low dose data set (a) & (b) and high dose data set (c) & (d).

Component 3

Component 3 accounts for 7.1% of the total variance in the low dose data set and 7.5% of the total variance in the high dose data set. Component 3 of the high dose data set is a combination of components 2 and 3 of the low dose data set, with r-values of 0.64 ± 8% and -0.76 ± 4%, respectively. Therefore component 3 of the high dose experiment is most similar to component 3 of the low dose experiment but there are also some features of component 2 of the low dose experiment present.

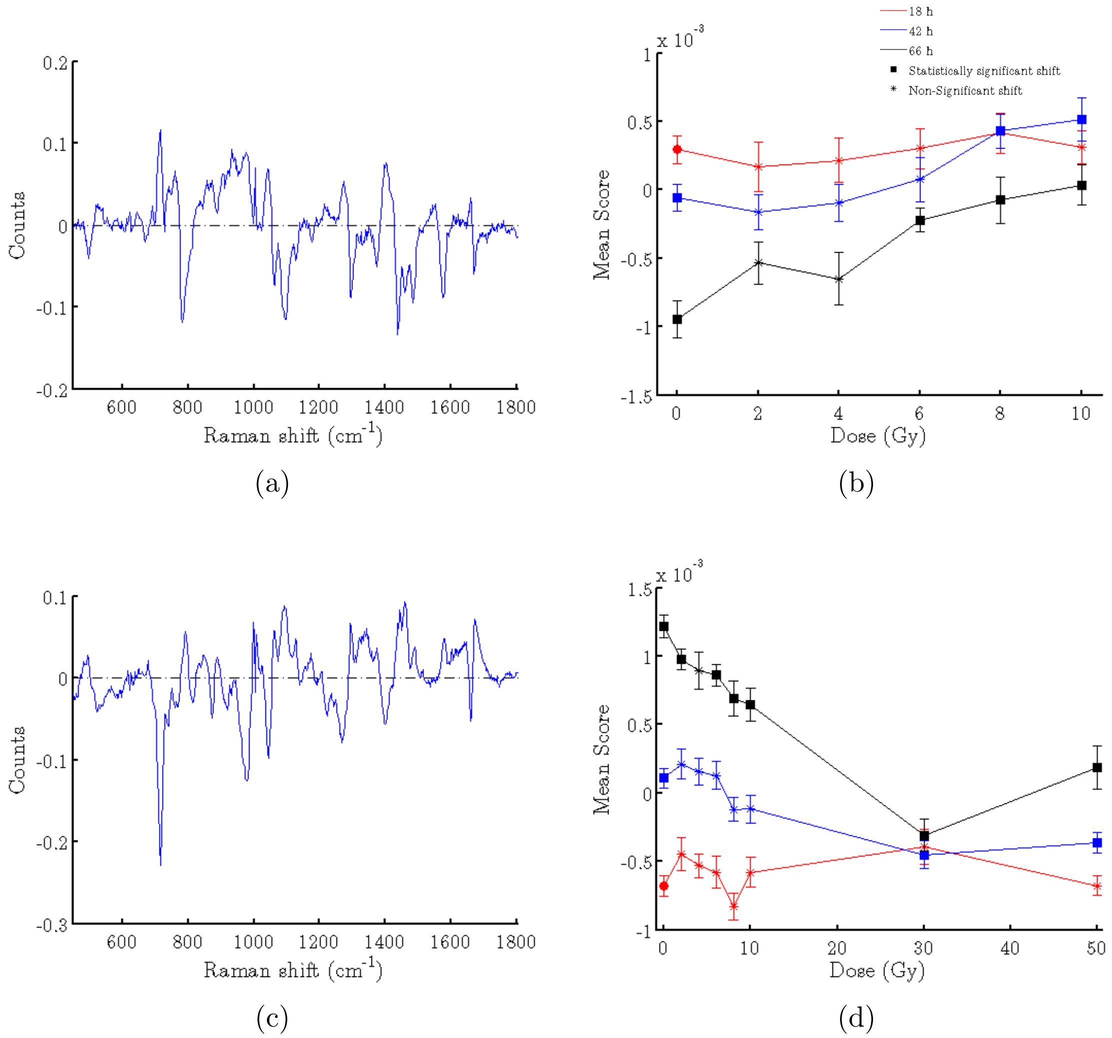

Figure 7.3: Component 3 and corresponding score plot for the MDA-MB-231 low dose data set (a) & (b) and high dose data set (c) & (d).

7.3 Discussion

7.3.1 Cell cycle Raman component

With a correlation r-value of 0.95 ± 1%, component 1 shown in Figure 7.1 is highly correlated to the cell cycle component identified as component 2 for the H460 experiment. The peak assignment for component 1 is identical to that for the H460 cell cycle component shown in chapter 5, Figure 5.4, with minor differences arising from variations in peak intensity. Component 1 of the MDA-MB-231 experiment describes variability in the data set arising from differences in protein and nucleic acid cell content relative to lipid content as a result of cell cycle distributions. The MDA-MB-231 cell cycle component contributes to 44.5% and 43.1% of the total variance in the low and high dose data sets, respectively. Unlike the MCF-7 and H460 cell lines, the cell cycle component is the first isolated principal component and therefore contributes to the majority of the variance in the data set.

Figures 7.1b & 7.1d indicate very little change in component scores for the MDA-MB-231 cell cycle component as a function of dose and harvesting time. There is a slight tendency towards more negative cell cycle component scores for the 66 hour irradiated samples, although this shift is not statistically significant. At both 42 and 66 hours post irradiation the 30 and 50 Gy populations have a slight shift towards more positive mean scores, relative to the 0 Gy population for that day. There is a corresponding drastic increase in the fraction of cells in G2 (appendix A, Figure A.3) which indicates these cells are experiencing G2 cell cycle arrest following large doses of radiation. Despite the shift in number of cells in G2 for these populations, the magnitude of the shift in cell cycle component score is not statistically significant. This agrees with trends described in [160], in which cells in early G2/M did not have significantly different scores from cells in late G1/S.

7.3.2 Radiation-induced Raman component

Identifying a radiation-induced Raman component in the MDA-MB-231 cell line turned out to be the most complicated and enlightening of the four cell lines. First considering the low dose data set, there is no obvious dose-dependent trends among the four reproducible components in this data set. This suggests that at low doses ($<$ 10 Gy) RS in combination with PCA is unable to identify dose-dependent spectral features. It is therefore important to determine whether it is the sensitivity of the Raman and PCA technique to detect dose-dependent trends which is limiting detection of such a component, or a lack of presence of dose-dependent responses at doses of 10 Gy or less for the MDA-MB-231 cell line. By considering the high dose data set, the answer to this question can be made clear. In the high dose data set, score plots for component 2 indicate a clear dose-dependent trend. Component 2 contributes 10.1% of the total variance for the high dose data set and is a mix of component 2 and 3 of the low dose data set. Component 2 from the high dose data set is shown in Figure 7.4 with Raman shifts assigned to major peaks contributing to the component. The molecular assignment of these Raman peaks are listed in Table 7.1.

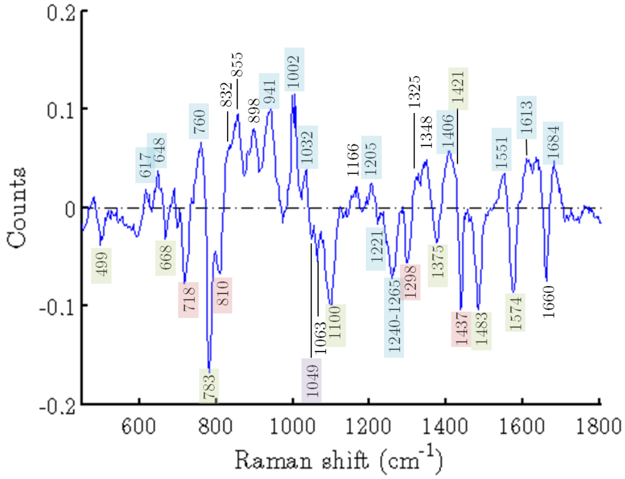

Figure 7.4: MDA-MB-231 high dose component 2 with major peaks labeled. Peaks arising from nucleic acids are shown in green, protein in blue, lipid in pink and carbohydrate in purple. Table 7.1 gives assignments for these peaks.

The molecular origin of the major Raman peaks in this component are colour coded on Figure 7.4 and indicate that the majority of positive features originate from protein and negative features appear to mainly be due to nucleic acid and lipid features. Major positive features arise from PO_2 stretching and tyrosine ring breathing at 832-852 cm^{-1}, deoxyribose backbone in DNA and alanine and lysine modes at 898 cm^{-1}, protein C-C backbone vibrations at 941 cm^{-1} and phenylalanine symmetric ring breathing at 1002 cm^{-1}. At higher wavenumbers major positive features arise from a variety of protein vibrations including the amide I band at 1684 cm^{-1} representing primarily β sheet secondary structure. Negative features include choline at 718 cm^{-1}, cytosine and uracil at 783 cm^{-1}, PO_2 symmetric stretching at 1100 cm^{-1}, vibrational modes from guanine and adenine at 1483 and 1574 cm^{-1} and the amide I band at 1660 cm^{-1} primarily representing α helix secondary structure.

	Assignment			
Raman shift (cm^{-1})	**Nucleic Acid**	**Protein**	**Lipid**	**Carb.**
499	G,T[150]			
617		C-C tw. phe.[77]		
648		C-C tw. tyr.[150]		
668	T,G[150],[162]			
718			C-N[77] cho.[77]	
760		trp.[150]		
783	C,U[77]			
810			O-P-O[59]	
832-852	O-P-O str.[59]	tyr. rb.[150]		
898	d. bk.[59]	ala., lys.[162]		
941		C-C bk. α[59]		
1002		phe. sym. rb.[150]		
1032		phe. C-H bd.[77]		
1049				C-O str.[59]
1063		C-N str.[59]	C-C str.[150]	
1100	PO$_2$ sym. str.[59]			
1166	DNA/RNA ring vib.[163]	phe. ring str.[163] C-H bd.[163]		
1205		phe., trp.[59]		
1221		ile., val., leu.[162]		
1240-1265		am. III[77]		
1298			C-H$_2$ tw.[150]	
1325	G[59]	C-H def.[59]		
1348	A,G[59]	C-H def.[59]		
1375	T[150] A,G[162]			
1406		asp., gla.[162]		
1421	A,G[58]			
1437			CH$_2$ def.[150]	
1483	G,A[153]			

Continued ...

Table 7.1: Raman peak assignment for MDA-MB-231 component 2 high dose experiment. Only main contributors of a band are listed.

Table 7.1 continued ...

	Assignment			
Raman shift (cm^{-1})	**Nucleic Acid**	**Protein**	**Lipid**	**Carb.**
1551		trp.[77]		
1574	G,A[150]			
1613		tyr.[161]		
1660		amide I α[77]	C=C str.[77]	
1684		amide I β[95]		

Table 7.1: Raman peak assignment for MDA-MB-231 component 2 high dose experiment. Only main contributors of a band are listed. Abbreviations: A: adenine, C: cytosine, T: thymine, G: guanine, U: uracil, d: deoxyribose, bk: backbone, asp:aspartic acid, gla: glutamic acid, ala: alanine, ile: isoleucine, val: valine, leu: leucine, trp: tryptophan, phe: phenylalanine, carb: carbohydrate, am: amide, lys: lysine, tyr: tyrosine, cho: choline, str: stretch, sym: symmetric, def: deformation, tw: twist, rb: ring breathing, bd: bending, vib: vibration, α: α helix, β: β sheet.

Trends in component 2 expression

Trends in the score plot for component 2 of the high dose experiment as shown in Figure 7.2d indicates a statistically significant but relatively small (compared to irradiated populations) shift in mean score in the positive direction for unirradiated samples at 42 and 66 hours post irradiation relative to the 18 hour unirradiated population. There is however, no shift between the unirradiated populations from 42 to 66 hours. The populations harvested at 18 hours post irradiation show only minor shifts towards positive mean scores for the irradiated populations relative to the unirradiated population for that day. Only the 50 Gy population is shifted towards a significantly more positive mean score. At 42 hours post irradiation populations receiving 6 Gy or less are not significantly shifted from the control for that day, however doses of 8 Gy or higher do cause a significant shift towards positive mean scores. The same trend is observed at 66 hours post irradiation however only doses of 4 Gy and lower are not significantly different form the unirradiated control for that day. The trends in component 2 score plot for the high dose experiment suggest that a radiation-induced increase in proteins relative to nucleic acid and lipid features as listed in Table 7.1 occurs in the MDA-MB-231 cell line.

Identification of dose-dependent spectral features at low doses

The fact that the high dose information was required to elucidate a radiation-induced trend in the data set makes sense. The score plot for component 2 shows that only doses as low 6 Gy at 66 hours post irradiation were exhibiting the described radiation-induced biochemical changes and at 18 and 42 hours post irradiation there is only expression of the spectral variability described by component 2 in two of the twelve low dose ($\leq$ 10 Gy) populations examined. Therefore, it can be concluded that the radiation-induced biochemical changes observed in the MDA-MB-231 cell line are present at doses as low as 8 Gy at 42 hours post irradiation however the expression of this variability in low doses is too subtle for this Raman technique to detect. As a result, the high dose data is required to make the spectral variability arising from this radiation response a significant portion of the variability in the data set and hence allow PCA to identify and pick out this variability.

Chapter 8

Results & Discussion IV: LNCaP Experiment

8.1 Population characteristics

LNCaP cells used in this experiment had relatively slow growth kinetics compared to the other three cell lines, and this is reflected in the fact that they required the smallest splitting ratio (see chapter 4, section 4.1.2). After plating in a flask, LNCaP cells tended to take longer to begin dividing compared to the other lines used and this is reflected in the use of a smaller splitting ratio. The LNCaP cells also tended to form less distinct colonies compared to the MCF-7 and H460 cell lines. The LNCaP cell line has the lowest average literature reported SF_2 value (SF_2=0.27, chapter 4, section 4.1.1) compared to the other three cell lines explored.

8.2 Raman experiment results

The low and high dose LNCaP Raman data sets consist of seven components with percent variances larger than 1%. Only three of these components were reproducible in both the low and high dose data sets (r-values > 0.75) between the two independent experiments for this line. In the low dose data set component 1 was highly reproducible with an r-value of 0.99 ± 0.2%, while components 2 and 4 were less reproducible with r-values of 0.78 ± 2% and 0.83 ± 3%. In the high dose data set, component 1 was highly reproducible with an r-value of 0.99 ± 0.2%, while components 2 and 4 were less reproducible with r-values of 0.79 ± 5% and 0.85 ± 2%.

Components 1 and 2 represented recognizable biochemical changes or relevant dose and time dependent trends and will be presented here, while component 4 did not and can be found in appendix D.

Component 1

Component 1 accounts for 54.2% of the total variance in the low dose data set and 53.9% of the total variance in the high dose data set. The spectral features of component 1 are very similar in both the low and high dose data sets with an r-value of 1.00 ± 0.01%.

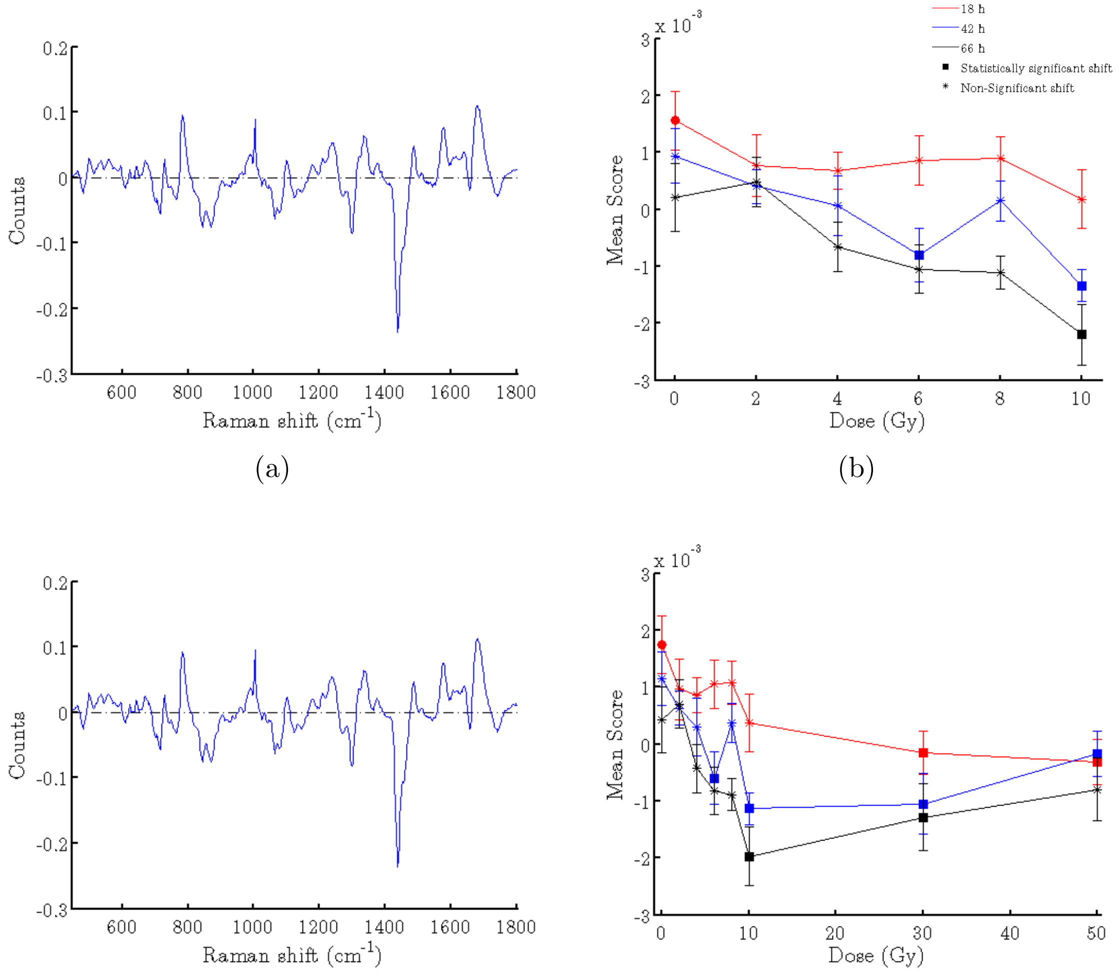

(a) (b)

(c) (d)

Figure 8.1: Component 1 and corresponding score plot for the LNCaP low dose data set (a) & (b) and high dose data set (c) & (d).

Component 2

Component 2 accounts for 6.0% of the total variance in the low dose data set and 5.8% of the total variance in the high dose data set. Between the low and high dose data sets, component 2 is nearly identical with an r-value of 1.00 ± 0.1%.

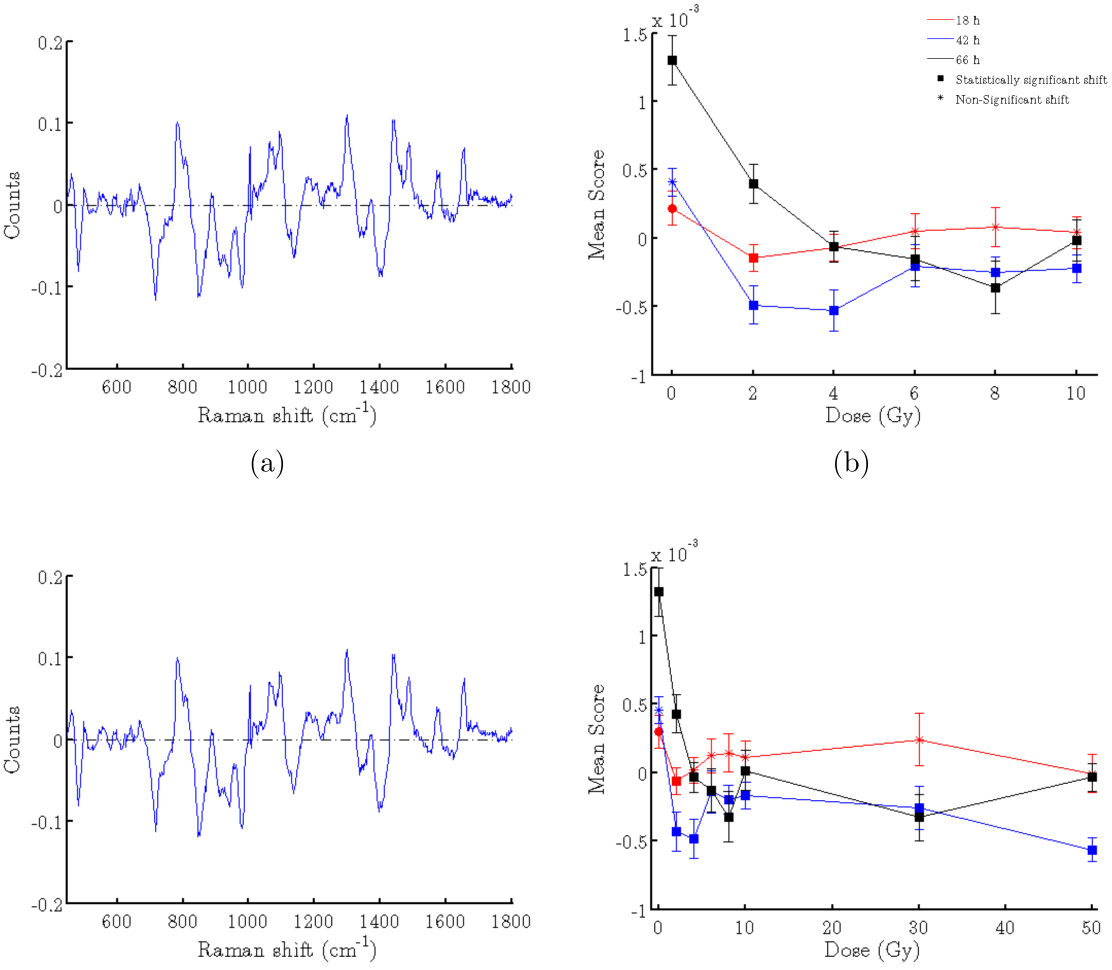

(a) (b)

(c) (d)

Figure 8.2: Component 2 and corresponding score plot for the LNCaP low dose data set (a) & (b) and high dose data set (c) & (d).

8.3 Discussion

8.3.1 Cell cycle Raman component

Component 1 (Figure 8.1) is highly correlated to the cell cycle component identified in the H460 experiment (r-value=0.97 ± 0.5%). Peak content in both are nearly identical with subtle differences between the two arising from peak intensity differences as a result of differing nucleic acid, protein and lipid content. Therefore, it is concluded that component 1 in the LNCaP experiment describes variability in the data set due to differences in protein and nucleic acid cell content relative to lipid content as a result of cell cycle distribution. The LNCaP cell cycle component explains the majority of the total variance in both the low and high dose data sets, with a percent variance of 54.2% and 53.9% respectively. This differs from what was observed for the H460 and MCF-7 cell lines, in which the percent variance for the cell cycle component was less than 20% of the total variance but is similar to what was observed for the MDA-MB-231 experiment. The reason for this difference is that in the H460 and MCF-7 data sets the radiation-induced component is much more dominant and actually makes up the majority of the variance in the data set, where as in the LNCaP (and MDA-MB-231) cell line this is not the case. The peak assignment for the LNCaP cell cycle component is identical to that for the H460 cell cycle component (chapter 5, Figure 5.4).

Scores for the LNCaP cell cycle component shown in Figure 8.1b & 8.1d indicate very little difference in the average expression of nucleic acid, protein and lipid content as a function of time post irradiation and dose (less than 10 Gy). A plot of the fraction of cells in G1, S and G2 in appendix A (Figure A.4) indicates only minor variations in the cell cycle distributions as a function of time post irradiation which agrees with the observed trends in the score plot. There is a slight tendency towards more negative cell cycle component scores for the samples irradiated to less than 8 Gy, in comparison to the controls for each harvesting time point however this shift is not statistically significant. At all three harvesting times the 30 and 50 Gy populations have a statistically significant shift (except 66 hours, 50 Gy) from the controls for that day towards more negative mean scores, and at 42 and 66 hours post irradiation this also occurs for the 10 Gy populations however within the quoted uncertainty for these scores the difference is minimal. Using FACS it is apparent that only minor differences in cell cycle distribution between irradiated and unirradiated populations at 18, 42 and 66 hours post irradiation exist. The irradiated populations tend towards more cells in G2 and less in G1 compared to controls (appendix A, Figure A.4), however these differences are very minor and are reflected by only small differences in mean component score for these irradiated populations.

8.3.2 Radiation-induced Raman component

Trends in score plots for each of the three reproducible components obtained in both the low and high dose LNCaP experiments indicates that component 2 in both the low and high dose data sets presents a significant dose-dependent relationship. This component contributes to 6.0% and 5.8% of the total variance for the low and high dose data sets respectively. Component 2 from the low dose data set is shown in Figure 8.3 with Raman shifts assigned to major peaks contributing to the component. The molecular assignment of these Raman peaks are listed in Table 8.1.

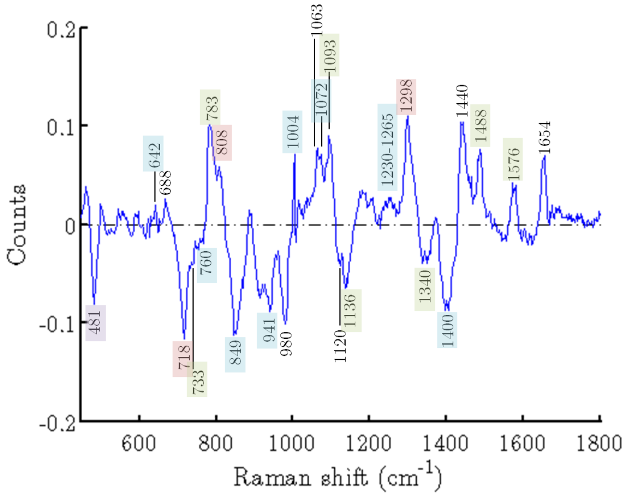

Figure 8.3: LNCaP low dose component 2 with major peaks labeled. Peaks arising from nucleic acids are shown in green, protein in blue, lipid in pink and carbohydrate in purple. Table 8.1 gives assignments for these peaks.

The molecular origin of the major Raman peaks in this component are colour coded on Figure 8.3 and indicate that the strongest positive and negative features arise from a combination of protein, nucleic acid and lipid molecular vibrations. Dominant positive features include the peak at 783 cm^{-1} originating from cytosine and uracil, 1063 cm^{-1} due to N-C stretching in protein, and C-C stretching in lipids and PO_2 stretching in nucleic acids at 1093 cm^{-1}. Other dominant positive features arise

	Assignment			
Raman shift (cm^{-1})	**Nucleic Acid**	**Protein**	**Lipid**	**Carb.**
481				Glyc.[166]
642		tyr.[150]		
668	G,T[150]	C-S str. cys.[77]		
718			cho.[150]	
733	A[150]			
760		trp.[150]		
783	C, U[77]			
808			O-P-O[59]	
849		tyr. rb.[59]		
941		C-C str.[150]		
980	d.[162]		C-C hg.[59]	
1004		phe. sym. rb.[59]		
1063		C-N str.[59]	C-C str.[59]	
1072		phe., lys.[162]		
1093	PO_2^- str.[59]			
1120		C-N str.[77]	C-C str.[77]	
1136	A,d.[162]			
1230-1265		am. III[77]		
1298			CH_2 tw.[150]	
1340	A[150] G[59]			
1400		COO^- sym. str.[95]		
1440		CH_2 bd.[77]	CH_2 bd.[77]	
1488	G,A[153]			
1576	G,A[150]			
1654		am. I α[95]	C=C[95]	

Table 8.1: Raman peak assignment for LNCaP component 2. Only main contributors of a band are listed. Abbreviations: A: adenine, C: cytosine, T: thymine, G: guanine, U: uracil, d: deoxyribose, cys: cystine, trp: tryptophan, phe: phenylalanine, carb: carbohydrate, am: amide, lys: lysine, tyr: tyrosine, cho: choline, hg: head group, glyc: glycogen, str: stretch, sym: symmetric, tw: twist, rb: ring breathing, bd: bending, α: α helix.

from lipid CH_2 twisting at 1298 cm^{-1} and CH_2 bond deformation in protein and lipid at 1440 cm^{-1}. Major negative features appear to be of nucleic acid, lipid and protein origin. Major negative features in component 2 occur at 718 cm^{-1} from choline, 849 cm^{-1} from tyrosine ring breathing, C-C stretching in protein at 941 cm^{-1}, deoxyribose and C-C lipid head groups at 980 cm^{-1}. At higher wavenumbers the negative features are dominated by adenine and deoxyribose at 1136 cm^{-1} and COO^{-} symmetric stretch in protein at 1400 cm^{-1}. Component 2 of both the high dose and low dose experiments are identical, with an r-value of 1.00 ± 0.1%. Minor differences arise in peak intensities, however the specific peak content and hence the biochemicals contributing to the component remain the same between the two.

Trends in component 2 expression

The score plot for component 2 of the high dose experiment shows an interesting dose-dependent trend which appears to manifest its self differently from that observed in the H460, MCF-7, and MDA-MB-231 cell lines. For those cell lines the dose-dependent component showed an induced biochemical change (ex. increased glycogen or increased protein content) in response to radiation, however, in the LNCaP cell line the main feature of the dose-dependent component (component 2) shows a reduced expression of negative features relative to positive features in unirradiated samples with increased time post irradiation, and an attenuation of this reduction in irradiated samples. Observation of the score plot for component 2 of the high dose data set shown in Figure 8.2d shows no significant difference in mean score between the 0 Gy and irradiated populations at 18 hours post irradiation, with the exception of the 2 Gy population, however within the quoted uncertainty for this value the shift can be considered minor. At 42 hours post irradiation, there is no significant shift in the 0 Gy population relative to that at 18 hours, however all irradiated populations are shifted towards negative mean scores compared to the 0 Gy population. This signifies a dose-dependent increase in expression of the negative features relative to positive features for the irradiated samples and represents, among other things, an increase in choline (one of the dominant negative features in component 2) relative to the biomolecules contributing to the positive features. At 66 hours post irradiation the 0 Gy population is significantly shifted towards a positive mean score compared to the 0 Gy populations at 42 and 18 hours. The 66 hour, 2 Gy population is also shifted towards positive mean score relative to the 42 and 18 hour 2 Gy populations. This suggests that cells receiving no radiation or low doses exhibit a decrease in the negative features of component 2 relative to positive features. The 4 Gy population at 66 hours is also shifted towards more positive values relative to that at 42 hours however this causes this population to have a similar mean score to the 4 Gy population at 18 hours. An increase in negative features relative to positive features at 42 hours post irradiation and then a reversal of this increase at 66 hours post irradiation is occurring in the irradiated populations. If the dose is low enough (2 Gy or less) it appears the reversal at 66 hours towards increased positive features relative to negative features is large enough to evoke a change in the biochemical content of these cells which is drastically different than that at 18 hours. For those populations which received higher doses (6 Gy or more) there is no change in the mean score at 66 hours post irradiation relative to 42 hours, indicating an attenuation of the reduced expression of negative features in the irradiated samples.

To summarize, the H460, MCF-7 and MDA-MB-231 cell lines show a clear radiation-induced effect while the LNCaP cell line shows a radiation-induced attenuation of a biochemical change which appears to occur with time in the control samples. Regardless of the nature of the dose-dependent change, be it induction or attenuation of biochemical features, component 2 for the LNCaP study can be identified as possessing a dose-dependent trend which appears to be linked to a radiation response in LNCaP cells.

Choline trends in other cell lines

The entire story becomes a bit more complicated in the fact that not only are the features of component 2 of the LNCaP experiment observed in this cell line, but a very similar component was also identified in the MCF-7 and MDA-MB-231 data sets. Component 4 of the high dose data set for the MCF-7 cell line has an r-value of 0.62 ± 6% with component 2 of the LNCaP high dose data set. Similarly, component 3 of the MDA-MB-231 low dose data set is highly anti-correlated (r-value=-0.72 ± 4%) with component 2 of the LNCaP high dose data set. Herein, for clarity the MDA-MB-231 component will be referred to in the inverted form, removing any confusion associated with the anti-correlated nature between the MDA-MB-231 component and the other two components. Many of the main positive features in the LNCaP component are also found as the main positive features in the MCF-7 and MDA-MB-231 components. Also the main negative features; choline at 718 cm^{-1} and phenylalanine symmetric stretch at 1404 cm^{-1} are also found as the main negative features in the MCF-7 and MDA-MB-231 components. The similar component from the LNCaP, MCF-7 and MDA-MB-231 (inverted) experiments are shown in Figure

8.4, illustrating the similarities in Raman spectral features. A full list of the similar peaks between component 2 of the LNCaP and the comparable MCF-7 and MDA-MB-231 components, whether they contribute to a positive or negative feature, and the molecular origins of these peaks are listed in Table 8.2.

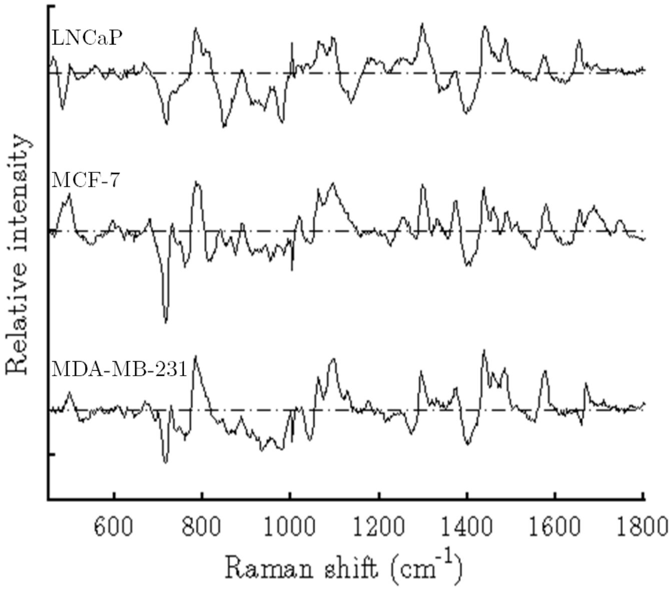

Figure 8.4: Component 2 of the LNCaP high dose data set, component 4 of the MCF-7 high dose data set and component 3 of the MDA-MB-231 low dose data set (inverted), illustrating the similarities between these three components. Table 8.2 lists the common peaks associated with all three components.

It is interesting to note the similarity between these three cell line's components is also reflected in the respective score plots, as shown in Figure 8.5 (note again for simplicity the MDA-MB-231 component 3 low dose score plot will be treated as if it was inverted to remove confusion with the anti-correlation). The LNCaP line shows an increase in positive features relative to negative features for the 0 Gy populations at 66 hours post irradiation while the irradiated populations show little change from 18 to 66 hour time points. The same conclusion can be made about the trends in score plot for the MCF-7 and MDA-MB-231 components. The noticeable difference between score plot trends in LNCaP versus MCF-7 and MDA-MB-231 lines is that at 66 hours post irradiation the LNCaP populations above 4 Gy have negative mean scores while all MCF-7 (up to 50 Gy) and MDA-MB-231 (up to 10 Gy) populations have positive mean scores. This means there is no shift towards negative scores for the irradiated populations in the MCF-7 and MDA-MB-231 lines, where as this is

	Assignment			
Common Raman peak (cm^{-1})	**Orientation LNCaP**	**Orientation MCF-7**	**Orientation MDA-MB-231**	**Molecular Origin**
718	-	-	+	cho.(l)
782	+	+	-	C, U(n)
807	+	n/a	-	O-P-O(l)
979	-	n/a	+	d.(n), C-C hg.(l)
1004	+	-	+	phe. sym. rb.(p)
1061	+	+	-	C-N str.(p), C-C str.(l)
1092	+	+	-	PO_2^- str.(n)
1298	+	+	-	CH_2 tw.(l)
1404	-	-	+	COO^- sym. str.(p)
1440	+	+	-	CH_2 bd.(p, l)
1487	+	+	-	G, A(n)
1575	+	+	-	G, A(n)
1654	+	+	n/a	am. I α(p), C=C(l)

Table 8.2: Common Raman peaks between LNCaP high dose component 2, MCF-7 high dose component 4 and MDA-MB-231 low dose component 3 (not inverted) and the molecular assignment for each peak. Peak orientation is also shown, illustrating the anti-correlation between the MDA-MB-231 component relative to the LNCaP and MCF-7 components. Abbreviations: n/a: not applicable, l: lipid, n: nucleic acid, p: protein, A: adenine, C: cytosine, G: guanine, U: uracil, d: deoxyribose, phe: phenylalanine, am: amide, cho: choline, hg: head group, str: stretch, sym: symmetric, tw: twist, rb: ring breathing, bd: bending, α: α helix.

observed in the LNCaP line.

Based on the average literature reported SF_2 values, the MCF-7 and MDA-MB-231 cell lines are considered radioresistant cell lines (SF_2 >0.35) while the LNCaP line is radiosensitive (SF_2 <0.35) [35]. The shift towards negative scores for irradiated LNCaP populations may be a result of the radiosensitivity of this line compared to the MCF-7 and MDA-MB-231 cells which did not show a significant shift towards negative scores in the irradiated populations. In the MCF-7 and MDA-MB-231 lines, irradiated populations receiving doses below 10 Gy actually behaved more like the unirradiated populations while in the LNCaP line only populations receiving below 4 Gy behaved similar to the unirradiated populations. This suggests that the accumulation of negative features like choline, relative to positive features in the LNCaP line is linked to an active radiation response in the irradiated populations and may be a result of the radiosensitive nature of the cell line. Furthermore, in the MCF-7 and MDA-MB-231 lines a continued, but not increased expression of negative features like choline relative to the positive features in irradiated populations may be an indication of a passive radiation response in these cells. In the context of this situation, a passive radiation response would be continued expression of choline rather than a reduction of choline as observed in the 0 Gy populations for the MCF-7 and MDA-MB-231 lines while the LNCaPs actively increase choline content in the irradiated populations in conjunction with the unirradiated populations reducing choline content.

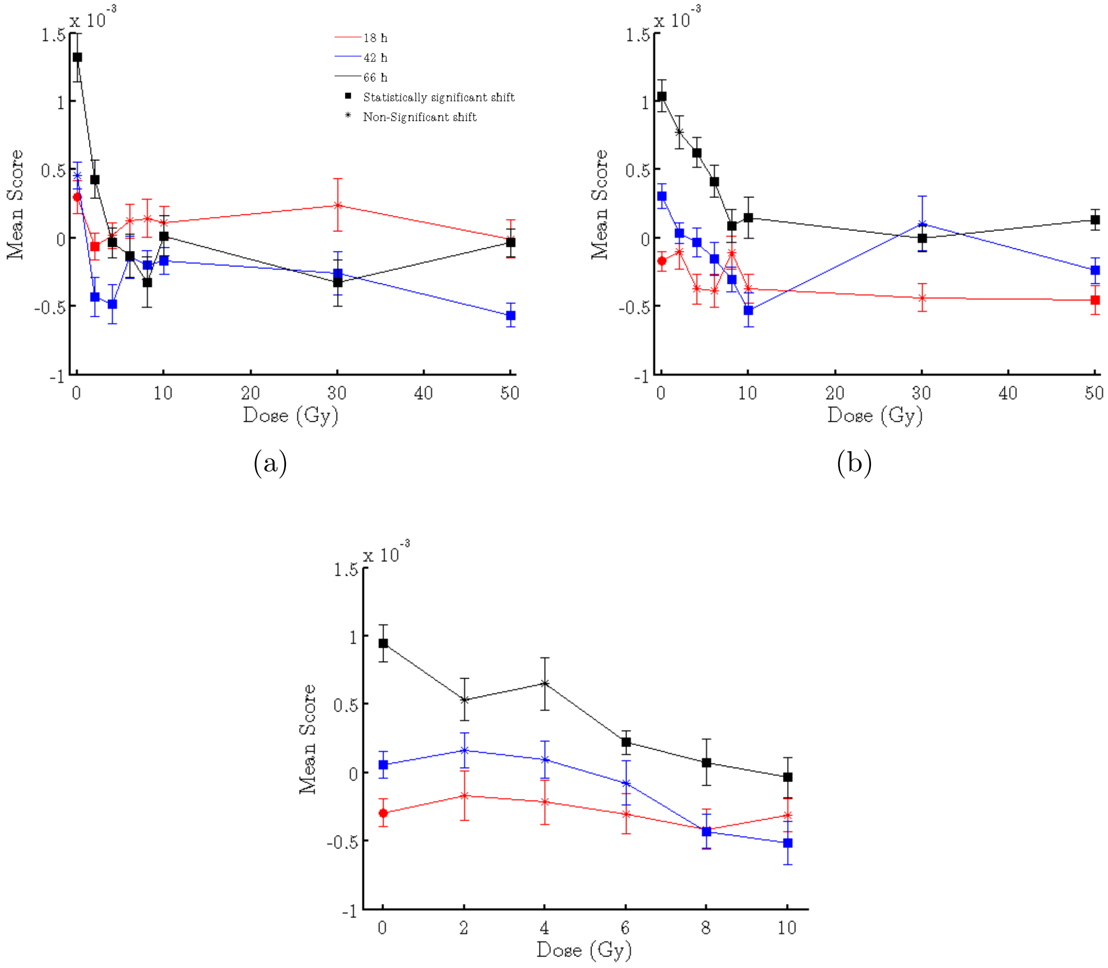

(a)

(b)

(c)

Figure 8.5: Score plots for LNCaP high dose component 2 (a), MCF-7 high dose component 4 (b) and MDA-MB-231 low dose component 3 (c, scores inverted)

In the MDA-MB-231 cell line the choline component (component 3 of low dose data set) splits into component 2 and 3 when high doses are considered (correlation r-values of 0.63 ± 8% and -0.76 ± 4%, respectively). Of all the spectral features in component 3 of the MDA-MB-231 high dose experiment (Figure 7.3c), the choline peak at 718 cm^{-1} is of the highest intensity and contributes greatly to the main negative features of the component. The score plot for component 3 of MDA-MB-231 high dose data set is shown in Figure 7.3d and shows an increase in mean score for unirradiated populations at 42 and 66 hours post irradiation relative to that at 18 hours post irradiation. Meanwhile, the irradiated populations (30 and 50 Gy) at 66 hours post irradiation show a significant shift back towards the 18 hour populations with small but slightly positive mean scores. This indicates that there is a reduction in choline relative to the positive features of this component in unirradiated populations. On the contrary, the irradiated populations reduce their choline content to a lesser extent than the unirradiated populations. This trend is similar to what was observed in component 3 of the MDA-MB-231 low dose data set and in the MCF-7 and LNCaP cell lines.

Biological justification

Konorov et al. have used RS to demonstrate an increase in the Raman peak intensity at 718 cm^{-1} coincident with cells cultured in a stress-inducing nutrient deprived environment [171]. The author suggests that autophagy inducing conditions cause an increase in the number of double-membrane autophagic vesicles in the cells. Recall from chapter 2, section 2.2.1 that a large portion of organelle membranes are composed of lipids and therefore the increased presence of these organelles may be resulting in an increased lipid content in the cell and hence more intense peak at 718 cm^{-1}. Therefore the proportion of cells in an autophagic state may be indicated by the 718 cm^{-1} peak intensity. Paglin et al. have demonstrated that in response to ionizing radiation of doses below 10 Gy, MCF-7 and LNCaP cells showed an increase in the number of acidic vesicular organelles which is linked to the induction of autophagy [172]. As shown in the score plots discussed for MCF-7, MDA-MB-231 and LNCaP lines (Figure 8.5) unirradiated populations reduce choline content (as measured by the 718 cm^{-1} peak) as a function of time post irradiation. This may indicate less cells undergoing autophagy in a population as a function of time post irradiation [173]. Meanwhile in the MCF-7 and MDA-MB-231 irradiated populations, the number of autophagic cells are not decreasing, or, not decreasing as drastically as the unirradiated populations. This makes sense if, based on work by Paglin et al., autophagy is induced as a response to ionizing radiation. Therefore, in irradiated populations, cells which normally would have recovered from an autophagic state are not recovering, or other cells are entering an autophagic state in response to radiation causing the net number of cells in an autophagic state to change less drastically in irradiated populations. In the LNCaP cells the mean scores actually became more negative at 66 hours post irradiation suggesting a net increase in the number of cells entering an autophagic state in this cell line. Again, the LNCaP line is radiosensitive in comparison to the MCF-7 and MDA-MB-231 lines and so it makes sense that there could be a stronger response to radiation by way of increased number of autophagic cells. Precise correlation between the observed trends in the reported Raman components with autophagy should be validated biologically before a rigid explanation of this trend is accepted.

Identifying dose-dependent spectral features at low doses for LNCaP cells

In folding in the high dose data with the low dose data a distinction was made in the MDA-MB-231 between a radiation-induced component (component 2) and a dose-dependent attenuation of choline (component 3). Interestingly, attenuation of choline in unirradiated populations appears to contribute to an extent great enough that it forms a principal component in three of the four cell lines studied. While there is a dose-dependent reduction in the degree of attenuation of choline it is independent of the radiation-induced responses found in the MCF-7 and MDA-MB-231 cell lines (appears as an orthogonal and unique principal component). In the LNCaP cell line, however, this appears to be the only dose-dependent trend observable with either the low dose or high dose data sets. This suggests one of two possible conclusions for the LNCaP cell line: 1) a radiation-induced response (with trends similar to that observed for the H460, MCF-7 and MDA-MB-231 cell lines) in the LNCaP cell line is too subtle to detect at doses up to 50 Gy using Raman as described in this work or 2) the reduced attenuation of choline and slight increase in choline levels in irradiated populations is in fact the only biochemical signature of radiation response for the radiosensitive LNCaP cell line.

Detection of radiation-induced responses at low doses

In the H460 and MCF-7 cell lines a radiation-induced accumulation of glycogen was detected using RS and PCA. The degree of expression of this radiation-induced response was very strong in cells receiving doses below 10 Gy since this component was the first PCA component and explained the majority of the total variance in the low and high dose data sets. As a result of the predominance of the expression of glycogen in cells receiving less than 10 Gy, it was possible to detect this radiation-induced response using the described Raman technique.

A radiation-induced increase in protein content relative to nucleic acid and lipids was observed in irradiated MDA-MB-231 cells however, identifying this radiation-induced response was not as obvious for cells receiving less than 10 Gy. The MDA-MB-231 radiation-induced component was only identified once consideration of the high dose data was also taken into account and it presented as the second PCA component. The radiation-induced component contributed less to the total variance of the data set than the cell cycle component did. The less dominant nature of the radiation-induced component was reflected in the fact that the radiation response of populations receiving less than 10 Gy, resulting in an accumulation of protein content, was less significant and only really became apparent for populations receiving over 8 Gy as early as 42 hours post irradiation. Therefore in the case of the MDA-MB-231 cell line, radiation-induced biochemical changes in irradiated cells are too subtle to identify using RS and considering doses less than 10 Gy.

In the case of the LNCaP cell line the Raman technique did not identify a radiation-induced accumulation of a certain biomolecule or collection of biomolecules, however, a dose-dependent attenuation of the reduction of choline was identified. The dose-dependent trend was identified for doses below 10 Gy, however like the MDA-MB-231 cell line it was not as predominant in the data set as the cell cycle component. The lack of identification of a radiation-induced accumulation of a set of biochemicals, as was observed in the other three cell lines may be because the Raman technique is not sensitive to the radiation-induced response occurring in LNCaP cells (because it is subtle), or there is a lack of such radiation response in this cell line.

Ultimately, the identification of a radiation-induced response in human cells cultured *in vitro* is dependent on the extent to which that response is expressed in a specific cell line. For example, the H460 cells show a strong response to radiation even at doses as low as 2 Gy and at the same time the Raman technique identified this radiation-induced response as representing the majority of the total variance in the data set. In contrast, the MDA-MB-231 cells only showed a radiation-induced response for populations receiving above 8 Gy at 42 hours post irradiation suggesting that radiation-induced response requires a larger dose to trigger a response. As a result the radiation-induced component identified using Raman was less dominant and required data in strongly responding cells (receiving large doses) to identify this response.

Moving forward with this Raman technique for identifying radiation-induced responses in cells in order to quantify cell radiosensitivity it will be important to bear in mind that the ability to do so will be governed by the subtlety of the radiation-induced response inherent to a specific cell line. It is also important to recognize that the type of biochemical changes occurring in response to exposure to radiation will be dependent on the specific cell line. Therefore, effective use of this Raman technique at early time points in a patient's treatment where cells have been exposed to 10 Gy or less will be dependent on the specific carcinoma and the unique radiation response associated with that disease. The nature and strength of the radiation-induced responses observed in the four cell lines studied in this work was established based on *in vitro* work and may change when moving to an *in vivo* system where the biological response mechanisms may become more complex and depend on more factors related to the *in vivo* system.

Chapter 9

Conclusion

Single cell RS in combination with PCA was successfully applied to identify dose-dependent biochemical changes in four human cell lines cultured *in vitro*. The four cell lines studied were human lung carcinoma (H460), breast carcinoma (MCF-7 and MDA-MB-231) and prostate carcinoma (LNCaP) each selected to create a panel of cells varying in tissue of origin, radiation sensitivity and p53 gene status.

Radiation-induced accumulation of glycogen was found to occur in both radioresistant H460 and MCF-7 cell lines. This radiation-induced response was found to be strongly represented in both H460 and MCF-7 irradiated populations and was identified in populations receiving as low as 2 Gy. RS was able to identify these radiation-induced responses in a data set containing only information on cells receiving less than 10 Gy.

A radiation-induced increase in protein relative to nucleic acid and lipid content was identified for the MDA-MB-231 cell line. This radiation-induced response was less dominant than the radiation-induced response found in the H460 and MCF-7 cell lines and was only significantly present in cells receiving 6 Gy or more at 66 hours post irradiation. Therefore larger doses and more time post irradiation was required for this biochemical change to accumulate enough to be detected in irradiated populations. As a result RS was unable to identify this radiation-induced response for a data set containing only doses less than 10 Gy, and the high dose populations in which this response was more dominant was required for recognition of this radiation-induced response.

In the MCF-7, MDA-MB-231 and LNCaP cell lines irradiated populations were found to have an attenuated reduction in the expression of choline relative to unirradiated populations. For the MCF-7 and MDA-MB-231 lines this dose-dependent feature was found to be independent and concurrent with the radiation-induced accumulation of glycogen in MCF-7 and protein in MDA-MB-231 cells. In the LNCaP cell line, this was the only dose-dependent trend identified. This suggests that for the LNCaP cell line no other radiation-induced response exists or it is too subtle to be detected for doses as high as 50 Gy using single cell RS.

In conclusion, identification of a radiation-induced response in human cells cultured *in vitro* is dependent on the extent to which that response is expressed in a specific cell line. The ability to use RS to identify radiation-induced responses in cells will be governed by the subtlety of the radiation-induced response inherent to a specific cell line. Also the type of biochemical changes occurring in response to exposure to radiation will be dependent on the specific cell line.

Ultimately the goal of this work was to demonstrate the use of single cell RS to monitor the response of cells cultured *in vitro* to low doses of radiation (<10 Gy). The work presented in this thesis is one step towards applying this technique for monitoring a specific patient's disease response to radiation, in order to quantify its radiosensitivity and adjust the RT treatment accordingly. It has been shown that effective use of single cell RS to monitor a patient's response to radiation early on in a patient's treatment (where the disease has been exposed to 10 Gy or less) will be dependent on the specific carcinoma and requires a detailed knowledge of the biochemical changes associated with the unique radiation response for that particular disease.

Bibliography

[1] D.R. Welch and J. Wei. Genetic, epigenetic regulation of human breast cancer progression, metastasis. *Endocr. Relat. Cancer*, 5:155–197, 1998.

[2] S. Webb. *The phyics of conformal radiotherapy: Advances in technology.* IOP Publishing, Bristol, 1997.

[3] B.D. Smith, B.G. Haffty, L.D. Wilson, G.L. Smith, A.N. Patel, and T.A. Buchholz. The future of radiation oncology in the United States from 2010 to 2020: Will supply keep pace with demand? *J. Clin. Oncol.*, 28(35):5160–5165, 2010.

[4] Jacob Van Dyk. *The Modern Technology of Radiation Oncology, Volume 2: A compendium for Medical Physicists and Radiation Oncologists.* Medical Physics Publishing Corporation, Madison, WI, USA, 2005.

[5] H.E. Johns and J.R. Cunningham. A precision Cobalt 60 unit for fixed field and rotation therapy. *Am. J. Roentgenol Radium Therapy Nuclear Med.*, 81:4–12, 1959.

[6] C. Nutting, D.P. Dearnaley, and S. Webb. Intensity modulated radiation therapy: a clinical review. *Brit. J. Radiol.*, 73:459–469, 2000.

[7] T. Bortfeld, A. L. Boyer, W. Schlegel, D. Kahler, and T. Waldron. Realization and verification of three-dimensional conformal radiotherapy with modulated fields. *Int. J. Radiat. Oncol. Biol. Phys.*, 30(4):899–908, 1994.

[8] S. Webb. The physical basis of IMRT and inverse planning. *Brit. J. Radiol.*, 76:678–689, 2003.

[9] S. Marnitz, M. Stuschke, J. Bohsung, A. Moys, I. Reng, R. Wurm, and V. Budach. Intraindividual comparison of conventional three-dimensional radiother-

apy and intensity modulated radiotherapy in the therapy of locally advanced non-small cell lung cancer. *Strahlenther Onkol*, 11:651–658, 2002.

[10] A. Eisbruch, L.H. Marsh, M.K. Martel, J.A. Ship, R.T. Haken, A.T. Pu, B.A. Fraass, and A.S. Lichter. Comprehensive irradiation of head and neck cancer using conformal multisegmental fields: Assessment of target coverage and noninvolved tissue sparing. *Int. J. Radiat. Oncol. Biol. Phys.*, 41(3):559–568, 1998.

[11] K.A. Vineberg, A. Eisbruch, M.M. Coselmon, D.L. McShan, M.L. Kessler, and B.A. Fraass. Is uniform target dose possible in IMRT plans in the head and neck? *Int. J. Radiat. Oncol. Biol. Phys.*, 52(5):1159–1172, 2002.

[12] M.J. Zelefsky, Z. Fuks, M. Hunt, Y. Yamada, C. Marion, C.C. Ling, H. Amols, E.S. Venkatraman, and S.A. Leibel. High-dose intensity modulated radiation therapy for prostate cancer: Early toxicity and biochemical outcome in 772 patients. *Int. J. Radiat. Oncol. Biol. Phys.*, 53(5):1111–1116, 2002.

[13] C. Burman, C.S. Chui, G. Kutcher, S. Leibel, M. Zelefsky, T. LoSasso, S. Spirou, Q. Wu, J. Yang, J. Stein, R. Mohan, Z. Fuks, and C.C. Ling. Planning, delivery and quality assurace of intensity-modulated radiotherapy using dynamic multileaf collimator: A strategy for large-scale implementation for the treatment of carcinoma of the prostate. *Int. J. Radiat. Oncol. Biol. Phys.*, 39(4):863–873, 1997.

[14] J.L. Bedford and A.P. Warrington. Commissioning of volumetric modulated arc therapy (VMAT). *Int. J. Radiat. Oncol. Biol. Phys.*, 73(2):537–545, 2009.

[15] E.C. Halperin, C.A. Perez, and L.W. Brady. *Principles and Practice of Radiation Oncology, 5th edition.* Lippincott Williams & Wilkins, Philadelphia, PA, USA, 2008.

[16] J.E. Tepper and C.I Sartor. Radiation therapy and biologics: a ripe opportunity? *Nat. Clin. Pract. Oncol.*, 3(9):463, 2006.

[17] J.J. Caudell, S.A. Eschrich, and J.F. Torres-Roca. Personalized medicine for radiation therapy. *Pers. Med.*, 10(2):107–110, 2013.

[18] A.C. Begg. Predicting response to radiotherapy: Evolutions and revolutions. *Int. J. Radiat. Biol.*, 85(10):825–836, 2009.

[19] L.J. Peters, W.A. Brock, J.D. Chapman, and G. Wilson. Predictive assays of tumor radiocurability. *Am. J. Clin. Oncol.*, 11(3):275–287, 1988.

[20] L.J. Peters. Radiation therapy tolerance limits: For one or for all? - Janeway Lecture. *Cancer*, 77(11):2379–2385, 1996.

[21] T. Bjork-Eriksson, C. West, E. Karlsson, and C. Mercke. Tumor radiosensitivity (SF_2) is a prognostic factor for local control in head and neck cancer. *Int. J. Radiat. Oncol. Biol. Phys.*, 46(1):13–19, 2000.

[22] C.M.L. West, S.E. Davidson, S.A. Roberts, and R.D. Hunter. The independence of intrinsic radiosensitivity as a prognostic factor for patient response to radiotherapy of carcinoma of the cervix. *Brit. J. Cancer*, 76(9):1184–1190, 1997.

[23] T. Bjork-Eriksson, C.M.L. West, E. Karlsson, N.J. Slevin, S.E. Davidson, R.D. James, and C. Mercke. The in vitro radiosensitivity of human head and neck cancers. *Brit. J. Cancer.*, 77(12):2371–2375, 1998.

[24] E.C. Bourton, P.N. Plowman, D. Smith, C.F. Arlett, and C.N. Parris. Prolonged expression of the γ-H2AX DNA repair biomarker correlates with excess acute and chronic toxicity from radiotherapy treatment. *Int. J. Cancer*, 129:2928–2934, 2011.

[25] J.M. Coco Martin, E. Mooren, C. Ottenheim, W. Burrill, M.I. Nunez, D. Sprong, H. Bartelink, and A.C. Begg. Potential of radiation-induced chromosome aberrations to predict radiosensitivity in human tumour cells. *Int. J. Radiat. Biol.*, 75(9):1161–1168, 1999.

[26] E.L. Levine, A. Renehan, R. Gossiel, S.E. Davidson, S.A. Roberts, C. Chadwick, D.P. Wilks, C.S. Potten, J.H. Hendry, R.D. Hunter, and C.M.L. West. Apoptosis, intrinsic radiosensitivity and prediction of radiotherapy response in cervical carcinoma. *Radiother. Oncol.*, 37:1–9, 1995.

[27] P. Vaupel, K. Schlenger, C. Knoop, and M. Hockel. Oxygenation of human tumors: Evaluation of tissue oxygen distribution in breast cancers by computerized O_2 measurements. *Cancer Res.*, 51:3316–3322, 1991.

[28] M.I. Koukourakis, A. Giatromanolaki, E. Sivridis, K. Simopoulos, J. Pastorek, C.C. Wykoff, K.C. Gatter, and A.L. Harris. Hypoxia-regulated carbonic anhydrase-9 (CA9) relates to poor vascularization and resistance of squamous cell head and neck cancer to chemoradiotherapy. *Clin. Cancer Res.*, 7:3399–3403, 2001.

[29] M. Luukkaa, T. Jokilehto, P. Kronqvist, T. Vahlberg, R. Grenman, P. Jaakkola, and H. Minn. Expression of the cellular oxygen sensor PHD2 (EGLN-1) predicts radiation sensitivity in squamous cell cancer of the head and neck. *Int. J. Radiat. Biol.*, 85(10):900–908, 2009.

[30] M. Nordsmark and J. Overgaard. A confirmatory prognostic study on oxygenation status and loco-regional control in advanced head and neck squamous cell carcinoma treated by radiation therapy. *Radiother. Oncol.*, 57:39–43, 2000.

[31] A.C. Begg, K. Haustermans, A.A.M. Hart, S. Dische, M. Saunders, B. Zackrisson, H. Gustaffson, P. Coucke, N. Paschoud, M. Hoyer, J. Overgaard, P. Antognoni, A. Richetti, J. Bourhis, H. Bartelink, J.C. Horiot, R. Corvo, W. Giaretti, H. Awwad, T. Shouman, T. Jouffroy, Z. Maciorowski, W. Dobrowsky, H. Struikmans, D. Rutgers, and G.D. Wilson. The value of pretreatment cell kinetic parameters as predictors for radiotherapy outcome in head and neck cancer: A multicenter analysis. *Radiother. Oncol.*, 50:13–23, 1999.

[32] A. Urruticoechea, I.E. Smith, and M. Dowsett. Proliferation marker Ki-67 in early breast cancer. *Journal of Clinical Oncology*, 23(28):7212–7220, 2005.

[33] N. Bouzubar, K.J. Walker, K. Griffiths, I.O. Ellis, C.W. Elston, J.F.R. Robertson, R.W. Blamey, and R.I. Nicholson. Ki67 immunostaining in primary breast cancer: Pathological and clinical associations. *Br. J. Cancer*, 59:943–947, 1989.

[34] N.N. Khodarev, M. Beckett, E. Labay, T. Darga, B. Roizman, and R.R. Weichselbaum. STAT1 is overexpressed in tumors selected for radioresistance and confers protection from radiation in transduced sensitive cells. *PNAS*, 101(6):1714–1719, 2004.

[35] A.J. McIlwrath, P.A. Vasey, G.M. Ross, and R. Brown. Cell cycle arrests and radiosensitivity of human tumor cell lines: Dependence on wild-type p53 for radiosensitivity. *Cancer Res.*, 54:3718–3722, 1994.

[36] W.J. Slichenmyer, W.G. Nelson, R.J. Slebos, and M.B. Kastan. Loss of p53-associated G1 checkpoint does not decrease cell survival following DNA damage. *Cancer Res.*, 53:4164–4168, 1993.

[37] S.L. Scott, J.D. Earle, and P.H. Gumerlock. Functional p53 increases prostate cancer cell survival after exposure to fractionated doses of ionizing radiation. *Cancer Res.*, 63:7190–7196, 2003.

[38] J.R. Williams, Y. Zhang, J. Russell, C. Koch, and J.B. Little. Human tumor cells segregate into radiosensitivity groups that associate with ATM and TP53 status. *Acta Oncologica*, 46:628–638, 2007.

[39] J.R. Williams, Y. Zhang, H. Zhou, D.S. Gridley, C.J. Koch, J. Russel, J.S. Slater, and J.B. Little. A quantitative overview of radiosensitivity of human tumor cells across histological type and TP53 status. *Int. J. Radiat. Biol.*, 84(4):253–264, 2008.

[40] J.F. Torres-Roca, S.Eschrich, H. Zhao, G. Bloom, J. Sung, S. McCarthy, A.B. Cantor, A. Scuto, C. Li, S. Zhang, R. Jove, and T. Yeatman. Prediction of radiation sensitivity using a gene expression classifier. *Cancer Res.*, 65(16):7169–7176, 2005.

[41] S. Eschrich, H. Zang, H. Zhao, D. Boulware, J.H. Lee, G. Bloom, and J.F. Torres-Roca. Systems biology modeling of the radiation sensitivity network: A biomarker discovery platform. *Int. J. Radiat. Oncol. Biol. Phys.*, 75(2):497–505, 2009.

[42] S.A. Eschrich, J. Pramana, H. Zhang, H. Zhao, D. Boulware, J.H. Lee, G. Bloom, C. Rocha-Lima, S. Kelley, D.P. Calvin, T.J Yeatman, A.C. Begg, and J.F. Torres-Roca. A gene expression model of intrinsic tumor radiosensitivity: Prediction of response and prognosis after chemoradiation. *Int. J. Radiat. Oncol. Biol. Phys.*, 75(2):489–496, 2009.

[43] S.A. Eschrich, W.J. Fulp, Y. Pawitan, J.A. Foekens nd M. Smid, J.W.M. Martens, M. Echevarria, W. Kamath, J.H. Lee, E.E. Harris, J. Bergh, and J.F. Torres-Roca. Validation of a radiosensitivity molecular signature in breast cancer. *Clin. Cancer Res.*, 18(18):5134–5143, 2012.

[44] A. Marusyk and K. Polyak. Tumor heterogeneity: causes and consequences. *BBBA-Rev. Cancer*, 1805(1):105–117, 2010.

[45] J.G. Rajendran, D.L. Schwartz, J. O'Sullivan, L.M. Peterson, P. Ng, J. Scharnhorst, J.R. Grierson, and K.A. Krohn. Tumor hypoxia imaging with [F-18] fluoromisonidazole positron emission tomography in head and neck cancer. *Clin. Cancer Res.*, 12(18):5435–5441, 2006.

[46] N.A. Mayr, W.T.C. Yuh, J.C. Arnholt, J.C. Ehrhardt, J.I. Sorosky, V.A. Magnotta, K.S. Berbaum, W. Zhen, A.C. Paulino, L.W. Oberley, A.K. Sood, and J.M. Buatti. Pixel analysis of MR perfusion imaging in predicting radiation therapy outcome in cervical cancer. *J. Magn. Reson. Imaging*, 12(6):1027–1033, 2000.

[47] M. Fuss, F. Wenz, M. Essig, M. Muenter, J. Debus, T.S. Herman, and M. Wannenmacher. Tumor angiogenesis of low-grade astrocytomas measured by dynamic susceptibility contrast-enhanced MRI (DSC-MRI) is predictive of local tumor control after radiation therapy. *Int. J. Radiat. Oncol. Biol. Phys.*, 51(2):478–482, 2001.

[48] A. Salskov, V.S. Tammisetti, J. Grierson, and H. Vesselle. FLT: Measuring Tumor Cell Proliferation In Vivo With Positron Emission Tomography and 3-Deoxy-3-[F^{18}] Fluorothymidine. In *Semin. Nucl. Med.*, volume 37, pages 429–439. Elsevier, 2007.

[49] H.G. Keen, B.A. Dekker, L. Disley, D. Hastings, S. Lyons, A.J. Reader, P. Ottewell, A. Watson, and J. Zweit. Imaging apoptosis in vivo using I^{124}-annexin V and PET. *Nucl. Med. Biol.*, 32(4):395–402, 2005.

[50] S. Nimmagadda, E.C. Ford, J.W. Wong, and M.G. Pomper. Targeted molecular imaging in oncology: focus on radiation therapy. In *Semin. Radiat. Oncol.*, volume 18, pages 136–148. Elsevier, 2008.

[51] C. Van de Wiele, C. Lahorte, W. Oyen, O. Boerman, I. Goethals, G. Slegers, and R.A. Dierckx. Nuclear medicine imaging to predict response to radiotherapy: a review. *Int. J. Radiat. Oncol. Biol. Phys.*, 55(1):5–15, 2003.

[52] C. Capirci, L. Rampin, P.A. Erba, F. Galeotti, G. Crepaldi, E. Banti, M. Gava, S. Fanti, G. Mariani, P.C. Muzzio, and D. Rubello. Sequential FDG-PET/CT

reliably predicts response of locally advanced rectal cancer to neo-adjuvant chemo-radiation therapy. *Eur. J. Nucl. Med. Mol. Imaging*, 34(10):1583–1593, 2007.

[53] A.J.P. Alix, G. Pedanou, and M. Berjot. Fast determination of the quantitative secondary structure of proteins by using some parameters of the Raman amide I band. *J. Mol. Struct.*, 174:159–164, 1988.

[54] D.C. Goodwin and J. Brahms. Form of DNA and the nature of interactions with proteins in chromatin. *Nucleic Acids Res.*, 5(3):836–850, 1978.

[55] H. Fabian and P. Anzenbacher. New developments in Raman spectroscopy of biological systems. *Vib. Spectrosc.*, 4(2):125–148, 1993.

[56] G.J. Thomas Jr. Raman spectroscopy of protein and nucleic acid assemblies. *Annu. Rev. Biophys. Biomol. Struct.*, 28(1):1–27, 1999.

[57] G.J. Puppels, F.F.M. de Mul, C. Otto, J. Greve, M. Robert-Nicoud, D.J. Arndt-Jovin, and T.M. Jovin. Studying single living cells and chromosomes by confocal Raman microspectroscopy. *Nature*, 347:301–302, 1990.

[58] G.J. Puppels, H.S.P. Garritsen, G.M.J. Segers-Nolten, F.F.M. de Mul, and J. Greve. Raman microspectroscopic approach to the study of human granulocytes. *Biophys. J.*, 60:1046–1056, 1991.

[59] I. Notingher, S. Verrier, S. Haque, J.M. Polak, and L.L. Hench. Spectroscopic study of human lung epithelial cells (A549) in culture: Living cells versus dead cells. *Biopolymers*, 72:230–240, 2003.

[60] K.W. Short, S. Carpenter, J.P. Freyer, and J.R. Mourant. Raman spectroscopy detects biochemical changes due to proliferation in mammalian cell cultures. *Biophys. J.*, 88:4274–4288, 2005.

[61] S. Verrier, I. Notingher, J.M. Polak, and L.L. Hench. In situ monitoring of cell death using Raman microspectroscopy. *Biopolymers*, 74:157–162, 2004.

[62] C. Krafft, L. Neudert, T. Simat, and R. Salzer. Near infrared Raman spectra of human brain lipids. *Spectrochim. Acta A*, 61:1529–1535, 2005.

[63] C.D. Sudworth and N. Krasner. Raman spectroscopy of Alzheimer's diseased tissue. In *Biomedical Optics 2004*, pages 93–101. International Society for Optics and Photonics, 2004.

[64] C.D. Sudworth, J.K.J. Archer, and D. Mann. The potential use of Raman spectroscopy for the diagnosis of Alzheimer's disease. In *Photonics North 2005*, pages 59691G–59691G. International Society for Optics and Photonics, 2005.

[65] J.P Caillé, M. Pigeon-Gosselin, and M. Pézolet. Laser Raman study of internally perfused muscle fibers effect of Mg^{2+}, ATP and Ca^{2+}. *BBA-Gen. Subjects*, 758(2):121–127, 1983.

[66] R. Manoharan, Y. Wang, and M.S. Feld. Histochemical analysis of biological tissues using Raman spectroscopy. *Spectrochim. Acta A*, 52:215–249, 1996.

[67] Q. Matthews, A.G. Brolo, J.J. Lum, X. Duan, and A. Jirasek. Raman spectroscopy of single human tumour cells exposed to ionizing radiation in vitro. *Phys. Med. Biol.*, 56:19–38, 2011.

[68] S.R. Hawi, W.B. Campbell, A. Kajdacsy-Balla, R. Murphy, F. Adar, and K. Nithipatikom. Characterization of normal and malignant human hepatocytes by Raman microspectroscopy. *Cancer Lett.*, 110:35–40, 1996.

[69] A. Mizuno, H. Kitajima, K. Kawauchi, S. Muraishi, and Y. Ozaki. Near-infrared Fourier transform Raman spectroscopic study of human brain tissues and tumours. *J. Raman Spectrosc.*, 25(1):25–29, 1994.

[70] C.J. Frank and R.L. McCreery. Raman specroscopy of normal and diseased human breast tissues. *Anal. Chem.*, 67:777–783, 1995.

[71] A.S. Haka, K.E. Shafer-Peltier, M. Fitzmaurice, J. Crowe, R.R. Dasari, and M.S. Feld. Diagnosing breast cancer by using Raman spectroscopy. *PNAS*, 102(35):12371–12376, 2005.

[72] C.H. Liu, B.B. Das, W.L. Sha Glassman, G.C. Tang, K.M. Yoo, H.R. Zhu, D.L. Akins, S.S. Lubicz, J. Cleary, R. Prudente, E. Celmer, A. Caron, and R.R. Alfano. Raman, fluorescence, and time-resolved light scattering as optical diagnostic techniques to separate diseased and normal biomedical media. *J. Photochem. Photobiol. B: Biol.*, 16:187–209, 1992.

[73] C.M. Krishna, N.B. Prathima, R. Malini, B.M. Vadhiraja, R.A. Bhatt, D.J. Fernandes, P. Kushtagi, M.S. Vidyasagar, and V.B. Kartha. Raman specroscopy studies for diagnosis of cancers in human uterine cervix. *Vib. Spectrosc.*, 41:136–141, 2006.

[74] K. Chen, Y. Qin, F. Zheng, M. Sun, and D. Shi. Diagnosis of colorectal cancer using Raman spectroscopy of laser-trapped single living epithelial cells. *Opt. Lett.*, 31(13):2015–2017, 2006.

[75] M.S. Feld, R. Manoharan, J. Salenius, J. Orenstein-Carndona, T.J. Roemer, J. F. Brennan III, R.R. Dasari, and Y. Wang. Detection and characterization of human tissue lesions with near-infrared Raman spectroscopy. *SPIE*, 2388:99–104, 1995.

[76] A. Molckovsky, L.M Wong Kee Song, M.G. Shim, N.E. Marcon, and B.C. Wilson. Diagnostic potential of near-infrared Raman spectroscopy in the colon: differentiating adenomatous fom hyperplastic polyps. *Gastrointest. Endosc.*, 57(3):396–402, 2003.

[77] N. Stone, C. Kendall, N. Shepherd, P. Crow, and H. Barr. Near-Infrared Raman spectroscopy for the classification of epithelial pre-cancers and cancers. *J. Raman Spectrosc.*, 33:564–573, 2002.

[78] D.P. Lau, Z. Huang, H. Lui, C.S. Man, K. Berean, M.D. Morrison, and H. Zeng. Raman spectroscopy for optical diagnosis in normal and cancerous tissue of the nasopharynx- preliminary findings. *Laser. Surg. Med.*, 32:210–214, 2003.

[79] L.P. Choo-Smith, H.G.M. Edwards, H.P. Endtz, J.M. Kros, F. Heule, H. Barr, J.S. Robinson Jr., H.A. Bruining, and G.J. Puppels. Medical applications of Raman spectroscopy: From proof of principle to clinical implementation. *Biopolymers (Biospectrosc.)*, 67:1–9, 2002.

[80] C.A. Lieber, S.K. Majumder, D.L. Ellis, D.D. Billheimer, and A. Mahadevan-Jansen. In vivo nonmelanoma skin cancer diagnosis using Raman microspectroscopy. *Laser. Surg. Med.*, 40:461–467, 2008.

[81] A. Mahadevan-Jansen, M.F. Mitchell, N. Ramanujam, U. Utzinger, and R. Richards-Kortum. Development of a fiber optic probe to measure NIR Ra-

man spectra of cervical tissue in vivo. *Photochem. Photobiol.*, 68(3):427–431, 1998.

[82] A. Nijssen, T.C. Bakker Schut, F. Heule, P.J. Caspers, D.P. Hayes, M.H.A. Neumann, and G.J. Puppels. Discriminating basal cell carcinoma from its surrounding tissue by Raman spectroscopy. *J. Invest. Dermatol.*, 119(1):64–69, 2002.

[83] A. Mahadevan-Jansen, M. Follen Mitchell, N. Ramanujam, A. Malpica, S. Thomsen, U. Utzingerand, and R. Richards-Kortum. Near-Infrared Raman spectroscopy for in vitro detection of cervical precancers. *Photochem. Photobiol.*, 68(1):123–132, 1998.

[84] C.J. Frank and R.L. McCreery. The use of Raman spectroscopy to differentiate between different prostatic adenocarcinoma cell lines. *Brit. J. Cancer*, 92:2166–2170, 2005.

[85] K. Sailer. Radiation-induced structural modifications in dsDNA analysed by FT-Raman spectroscopy. *Int. J. Radiat. Biol.*, 69(5):601–613, 1996.

[86] C.P. Shaw and A. Jirasek. The use of ultraviolet resonance Raman spectroscopy in the analysis of ionizing-radiation induced damage in DNA. *Appl. Spectrosc.*, 63(4):412–422, 2009.

[87] A. Synytsya, P. Alexa, J. de Boer, M. Loewe, M. Moosburger, M. Wurkner, and K. Volka. Raman spectroscopic study of calf thymus DNA: an effect of proton- and γ-irradiation. *J. Raman Spectrosc.*, 38:1406–1415, 2007.

[88] A. Synytsya, P. Alexa, J. de Boer, M. Loewe, M. Moosburger, M. Wurkner, and K. Volka. Raman spectroscopic study of serum albumins: an effect of proton and γ-irradiation. *J. Raman Spectrosc.*, 38:1646–1655, 2007.

[89] A. Torreggiani, M. Tamba, I. Manco, M.R. Faraone-Mennella, C. Ferreri, and C. Chatgilialoglu. Radiation damage of lysozyme in a biomimetic model: some insights by Raman spectroscopy. *J. Mol. Struct.*, 744:767–773, 2005.

[90] K. Sailer, S. Viaggi, and M. Nusse. Kinetics of radiation- and cytochrome c-induced modifications in liposomes analysed by FT- Raman spectroscopy. *BBA*, 1329:259–268, 1997.

[91] S.P. Verma. Low levels of irradiation modify lipid domains in model membranes: A laser Raman study. *Radiat. Res.*, 107:183–193, 1986.

[92] S.P. Verma and A. Rastogi. Role of proteins in protection against radiation-induced damage in membranes. *Radiat. Res.*, 122:130–136, 1990.

[93] S.P. Verma and N. Sonwalkar. Structural changes in plasma membranes prepared from irradiated Chinese hamster V79 cells as revealed by Raman spectroscopy. *Radiat. Res.*, 126:27–35, 1991.

[94] A. Synytsya, A. Synytsya, P. Alexa, R. Wagner, M. Davidkova, and K. Volka. Raman spectroscopic study on sodium hyaluronate: an effect of proton and γ irradiation. *J. Raman Spectrosc.*, 42:544–550, 2011.

[95] A. Synytsya, P. Alexa, J. Besserer, J. de Boer, S. Froschauer, R. Gerlach, M. Loewe, M. Moosburger, I. Obstova, P. Quicken, B. Sonsa, K. Volka, and M. Wurkner. Raman spectroscopy of tissue samples irradiated by protons. *Int. J. Radiat. Biol.*, 80(8):581–591, 2004.

[96] R.J. Lakshmi, V.B. Kartha, C.M. Krishna, J.G.R. Solomon, G. Ullas, and P.U. Devi. Tissue Raman spectroscopy for the study of radiation damage: Brain irradiation of mice. *Radiat. Res.*, 157:175–182, 2002.

[97] M.S. Vidyasagar, K. Maheedhar, B.M. Vadhiraja, D.J. Fernendes, V.B. Kartha, and C.M. Krishna. Prediction of radiotherapy response in cervix cancer by Raman spectroscopy: A pilot study. *Biopolymers*, 89(6):530–537, 2008.

[98] D.C. Rizzo. *Fundamentals of Anatomy and Physiology 3ed.* Delmar Cengage Learning, Clifton Park, N.Y., 2010.

[99] A. Mahadevan-Jansen and R. Richards-Kortum. Raman spectroscopy for the detection of cancers and precancers. *J. Biomed. Opt.*, 1(1):31–70, 1996.

[100] Q. Matthews, A. Jirasek, J.J. Lum, and A.G. Brolo. Biochemical signatures of in vitro radiation response in human lung, breast and prostate tumour cells observed with Raman spectroscopy. *Phys. Med. Biol*, 56:6839–6855, 2011.

[101] M. Baumann, V. Gregoire, M. Joiner, and A. van der Kogel. *Basic Clinical Radiobiology.* Edward Arnold, London, U.K., 2009.

[102] S.H. Levitt, J.A. Purdy, C.A. Perez, and S. Vijayakumar. *Technical basis of radiation therapy 4 ed.* Springer-Verlag Berlin Heidelberg, 2006.

[103] E.B. Podgorsak, P. Metcalfe, and J. Van Dyk. *The Modern Technology of Radiation Oncology, Volume 1: A Compendium for Medical Physicists and Radiation Oncologists*, chapter Medical Accelerators. Medical Physics Publishing Corporation, Madison, WI, USA, 1999.

[104] F.M. Khan 3 ed. *The Physics of Radiation Therapy.* Lippincott Williams and Wilkins, Philadelphia, PA, USA, 2003.

[105] H.E. Johns and J.R. Cunningham. *The Physics of Radiology 4ed.* Charles C Thomas Publisher, Springfield, IL, USA, 1983.

[106] E.B. Podgorsak. *Radiation Physics for Medical Physicists 2ed.* Springer-Verlag Berlin Heidelberg, 2010.

[107] F.H. Attix. *Introduction to Radiological Physics and Radiation Dosimetry.* Wiley-VCH Verlag GmbH & Co. KGaA, Weinheim, Germany, 2004.

[108] J.M. Orten and O.W. Neuhaus. *Human Biochemistry 9ed.* The C.V. Mosby Company, Saint Louis, MO, USA, 1975.

[109] E.L. Travis. *Primer of Medical Radiobiology 2ed.* Mosby-Year Book, INC., St. Louis, MO, USA, 1989.

[110] S.R. Bolsover, E.A. Shephard, H.A. White, and J.S. Hyams. *Cell Biology: A Short Course.* John Wiley & Sons, Inc., Hoboken, NJ, USA, 2011.

[111] Z. Darzynkiewicz, T. Sharpless, L. Staiano-Coico, and M.R. Melamed. Subcompartments of the G1 phase of cell cycle detected by flow cytometry. *Proc. Natl. Acad. Sci. USA*, 77(11):6696–6699, 1980.

[112] H.A. Crissman, Z. Darzynkiewicz, R.A. Tobey, and J.A. Steinkamp. Correlated measurements of DNA, RNA, and protein in individual cells by flow cytometry. *Science*, 228(4705):1321–1324, 1985.

[113] Z. Darzynkiewicz, F. Traganos, and M.R. Melamed. New cell cycle compartments identified by multiparameter flow cytometry. *Cytometry*, 1(2):98–108, 1980.

[114] H. Lodish, A. Berk, S. Lawrence Zipursky, P. Matsudaira, D. Baltimore, and J. Darnell. *Molecular Cell Biology 4ed.* W.H. Freeman, New York, NY, USA, 2000.

[115] R.L. Warters, K.G. Hofer, C.R. Harris, and J.M. Smith. Radionuclide toxicity in cultured mammalian cells: elucidation of the primary site of radiation damage. *Curr. Top. Radiat. Res. Q.*, 12(1-4):389–407, 1978.

[116] R.L. Warters and K.G. Hofer. Radionuclide toxicity in cultured mammalian cells. *Radiat. Res.*, 69:348–358, 1977.

[117] R. Roots and S. Okada. Estimation of life times and diffusion distances of radicals involved in x-ray-induced DNA strand breaks or killing of mammalian cells. *Radiat. Res.*, 64(2):306–320, 1975.

[118] S. Matsuoka, B.A. Ballif, A. Smogorzewska, E.R. McDonald III, K.E. Hurov, J. Luo, C.E. Bakalarski, Z. Zhao, N. Solimini, Y. Lerenthal, Y. Shiloh, S.P. Gygi, and S.J. Elledge. ATM and ATR substrate analysis reveals extensive protein networks responsive to DNA damage. *Sci. Signal.*, 316(5828):1160–1166, 2007.

[119] J. Lukas, C. Lukas, and J. Bartek. Mammalian cell cycle checkpoints: signalling pathways and their organization in space and time. *DNA Repair*, 3(8):997–1007, 2004.

[120] M.B. Kastan and J. Bartek. Cell-cycle checkpoints and cancer. *Nature*, 432(7015):316–323, 2004.

[121] M. Fernet, F. Mégnin-Chanet, J. Hall, and V. Favaudon. Control of the G2/M checkpoints after exposure to low doses of ionising radiation: implications for hyper-radiosensitivity. *DNA Repair*, 9(1):48–57, 2010.

[122] B. Xu, S. Kim, D. Lim, and M.B. Kastan. Two molecularly distinct G2/M checkpoints are induced by ionizing irradiation. *Mol. Cell. Biol.*, 22(4):1049–1059, 2002.

[123] B. Endlich, I.R. Radford, H.B. Forrester, and W.C. Dewey. Computerized video time-lapse microscopy studies of ionizing radiation-induced rapid-interphase and mitosis-related apoptosis in lymphoid cells. *Radiat. Res.*, 153(1):36–48, 2000.

[124] H.B. Forrester, C.A. Vidair, N. Albright, C.C. Ling, and W.C. Dewey. Using computerized video time lapse for quantifying cell death of X-irradiated rat embryo cells transfected with c-myc or c-Ha-ras. *Cancer Res.*, 59(4):931–939, 1999.

[125] L. Hayflick. The limited in vitro lifetime of human diploid cell strains. *Exp. Cell Res.*, 37(3):614–636, 1965.

[126] B.G. Douglas and J.F. Fowler. The effect of multiple small doses of X rays on skin reactions in the mouse and a basic interpretation. *Radiat. Res.*, 66(2):401–426, 1976.

[127] R.G. Dale. The application of the linear-quadratic dose-effect equation to fractionated and protracted radiotherapy. *Brit. J. Radiol.*, 58(690):515–528, 1985.

[128] J.P. Kirkpatrick, J.J. Meyer, and L.B. Marks. The linear-quadratic model is inappropriate to model high dose per fraction effects in radiosurgery. In *Semin. Radiat. Oncol.*, volume 18, pages 240–243. Elsevier, 2008.

[129] A. Brahme. Dosimetric precision requirements in radiation therapy. *Acta Oncol.*, 23(5):379–391, 1984.

[130] S.M. Bentzen. Steepness of the clinical dose-control curve and variation in the in vitro radiosensitivity of head and neck squamous cell carcinoma. *Int. J. Radiat. Biol.*, 61(3):417–423, 1992.

[131] W.K. Sinclair. Cyclic X-Ray Responses in Mammalian Cells in Vitro 1. *Radiat. Res.*, 178(2):AV112–AV124, 2012.

[132] L.H. Gray, A.D. Conger, M. Ebert, S. Hornsey, and O.C.A. Scott. The concentration of oxygen dissolved in tissues at the time of irradiation as a factor in radiotherapy. *Brit. J. Radiol.*, 26(312):638–648, 1953.

[133] R.H. Thomlinson and L.H. Gray. The histological structure of some human lung cancers and the possible implications for radiotherapy. *Brit. J. Cancer*, 9(4):539–549, 1955.

[134] C.V. Raman and K.S. Krishnan. The production of new radiations by light scattering. Part I. *P. Roy. Soc. Lond. A*, 122(789):23–35, 1928.

[135] E. Smith and G. Dent. *Modern Raman Spectroscopy A Practical Approach.* John Wiley & Sons, Ltd., West Sussex, England, 2005.

[136] J.R. Ferraro and K. Nakamoto. *Introductory Raman Spectroscopy.* Academic Press INC., San Diego, CA, USA, 1994.

[137] D.A. Long. *The Raman effect a unified treatment of the theory of Raman scattering by molecules.* John Wiley & Sons, Ltd., West Sussex, England, 2002.

[138] R.J.H. Clark and T.J. Dines. Resonance Raman spectroscopy, and its application to inorganic chemistry. *Angew. Chem. Int. Ed. Engl.*, 25:131–158, 1986.

[139] D.W. Piston. Choosing objective lenses: the importance of numerical aperture and magnification in digital optical microscopy. *Biol. Bull.*, 195:1–4, 1998.

[140] M. Abramowitz, K.R. Spring, H.E. Keller, and M.W. Davidson. Basic principles of microscope objectives. *BioTechniques*, 33(4):772–781, 2002.

[141] J.M. Lerner and A. Thevenon. *The Optics of Spectroscopy: A Tutorial.* HORIBA Jobin Yvon, Edison, NJ, USA, 2013.

[142] J.E. Pemberton, R.L. Sobocinski, and G.R. Sims. The effect of charge traps on Raman spectroscopy using a Thomson-CSF charge coupled device detector. *Appl. Spec.*, 44(2):328–330, 1990.

[143] I. Notingher and L.L. Hench. Raman microspectroscopy: a noninvasive tool for studies of individual living cells in vitro. *Expert Rev. Med. Devices*, 3(2):215–234, 2006.

[144] I.T. Jolliffe. *Principal Component Analysis.* Springer-Verlag New York, Inc., New York, N.Y., 2002.

[145] K.C. Schuster, I. Reese, E. Urlaub, J.R. Gapes, and B. Lendi. Multidimensional information on the chemical composition of single bacterial cells by confocal Raman microspectroscopy. *Anal. Chem.*, 72:5529–5534, 2000.

[146] D. Pappas, B.W. Smith, and J.D. Winefordner. Raman spectroscopy in bioanalysis. *Talanta*, 51:131–144, 2000.

[147] G.J. Puppels, J.H.F. Olminkhof, G.M.J. Segers-Nolten, C. Otto, F.F.M. de Mul, and J. Greve. Laser irradiation and Raman spectroscopy of single living cells and chromosomes: sample degradation occurs with 514.5 nm but not with 660 nm laser light. *Exp. Cell. Res.*, 195:361–367, 1991.

[148] I. Notingher, S. Verrier, H. Romanska, A.E. Bishop, J.M. Polak, and L.L. Hench. In situ characterisation of living cells by Raman spectroscopy. *Spectroscopy*, 16:43–51, 2002.

[149] A. Zoladek, F.C. Pascut, P. Patel, and I. Notingher. Non-invasive time-course imaging of apoptotic cells by confocal Raman micro-spectroscopy. *J. Raman Spectrosc.*, 42:251–258, 2011.

[150] C. Krafft, T. Knetschke, A. Siegner, R.H.W. Funk, and R. Salzer. Mapping of single cells by near infrared Raman microspectroscopy. *Vib. Spectrosc.*, 32:75–83, 2003.

[151] G. Schulze, A. Jirasek, M.M.L. Yu, A. Lim, R.F.B. Turner, and M.W. Blades. Investigation of selected baseline removal techniques as candidates for automated implementation. *Appl. Spectrosc.*, 59(5):545–574, 2005.

[152] J.R. Mourant, K.W. Short, S. Carpenter, N. Kunapareddy, L. Coburn, T.M. Powers, and J.P. Freyer. Biochemical differences in tumorigenic and nontumorigenic cells measured by Raman and infrared spectroscopy. *J. Biomed. Optics*, 10(3):031106–1 – 031106–15, 2005.

[153] N. Uzunbajakava, A. Lenferink, Y. Kraan, B. Willekens, G. Vrensen, J. Greve, and C. Otto. Nonresonant Raman imaging of protein distribution in single human cells. *Biopolymers (Biospectroscopy)*, 72:1–9, 2003.

[154] J.B. Mitchell, R. Choudhuri, K. Fabre, A.L. Sowers, D. Citrin, S.D. Zabludoff, and J.A. Cook. In vitro and in vivo radiation sensitization of human tumor cells by a novel checkpoint kinase inhibitor, AZD7762. *Clin. Cancer Res.*, 16(7):2076–2084, 2010.

[155] L. Hui, Y. Zheng, Y. Yan, J. Bargonetti, and D.A. Foster. Mutant p53 in MDA-MB-231 breast cancer cells is stabilized by elevated phospholipase D activity and contributes to survival signals generated by phospholipase D. *Oncogene*, 25:7305–7310, 2006.

[156] P.A. Schroeder, N.D. Melear, and R.J. Pruett. Quantitative analysis of anatase in Georgia kaolins using Raman spectroscopy. *Appl. Clay Sci.*, 23:299–308, 2003.

[157] H. Behrens, J. Roux, D.R. Neuville, and M. Siemann. Quantification of dissolved H_2O in silicate glasses using confocal microRaman spectroscopy. *Chem. Geol.*, 229:96–112, 2006.

[158] A. Sadezky, H. Muckenhuber, H. Grothe, R. Niessner, and U. Poschl. Raman microspectroscopy of soot and related carbonaceous materials: Spectral analysis and structural information. *Carbon*, 43:1731–1742, 2005.

[159] A. Savitzky and M.J.E. Golay. Smoothing and differentiation of data by simplified least squares procedures. *Anal. Chem.*, 36(8):1627–1639, 1964.

[160] Q. Matthews, A. Jirasek, J. Lum, X. Duan, and A.G. Brolo. Variability in Raman spectra of single human tumor cells cultured in vitro: correlation with cell cycle and culture confluency. *Appl. Spectrosc.*, 64(8):871–887, 2010.

[161] D. Naumann. FT-Infrared and FT-Raman spectroscopy in biomedical research. *Appl. Spectrosc. Rev.*, 36(2-3):239–298, 2001.

[162] S.A. Overman, K.L. Aubrey, K.E. Reilly, O. Osman, S.J. Hayes, P. Serwer, and G.J. Thomas Jr. Conformation and interactions of the packaged double-stranded DNA genome of bacteriophage T7. *Biospectroscopy*, 4:S47–S56, 1998.

[163] K.M. Omberg, J.C. Osborn, S.L. Zhang, J.P. Freyer, J.R. Mourant, and J.R. Schoonover. Raman spectroscopy and factor analysis of tumorigenic and non-tumorigenic cells. *Appl. Spectrosc.*, 56(7):813–819, 2002.

[164] J. Brognard, A.S. Clark, Y. Ni, and P.A. Dennis. Akt/Protein Kinase B is constitutively active in non-small cell lung cancer cells and promotes cellular survival and resistance to chemotherapy and radiation. *Cancer Res.*, 61:3986–3997, 2001.

[165] J. Tan, L. Geng, E.M. Yazlovitskaya, and D.E. Hallahan. Protein kinase B/Akt-dependent phosphorylation of glycogen synthase kinase-3β in irradiated vascular endothelium. *Cancer Res.*, 66(4):2320–2327, 2006.

[166] G. Shetty, C. Kendall, N. Shepherd, N. Stone, and H. Barr. Raman spectroscopy: elucidation of biochemical changes in carcinogenesis of oesophagus. *Brit. J. Cancer*, 94:1460–1464, 2006.

[167] H.G.M. Edwards, D.E. Hunt, and M.G. Sibley. FT-Raman spectroscopic study of keratotic materials: horn, hoof and tortoiseshell. *Spectrochim. Acta A*, 54:745–757, 1998.

[168] J.R. Mourant, Y.R. Yamanda, S. Carpenter, L.R. Dominique, and J.P. Freyer. FTIR spectroscopy demonstrates biochemical differences in mammalian cell cultures at different growth stages. *Biophys. J.*, 85:1938–1947, 2003.

[169] K. Izuishi, K. Kato, T. Ogura, T. Kinoshita, and H. Esumi. Remarkable tolerance of tumor cells to nutrient deprivation: possible new biochemical target for cancer therapy. *Cancer Res.*, 60:6201–6207, 2000.

[170] J.M. Albert, K.W. Kim, C. Cao, and B. Lu. Targeting the Akt/mammalian target of rapamycin pathway for radiosensitization of breast cancer. *Mol. Cancer Ther.*, 5(5):1183–1189, 2006.

[171] S.O. Konorov, M.A. Jardon, J.M. Piret, M.W. Blades, and R.F.B. Turner. Raman microspectroscopy of live cells under autophagy-inducing conditions. *Analyst*, 137:4662–4668, 2012.

[172] S. Paglin, T. Hollister, T. Delohery, N. Hackett, M. McMahill, E. Sphicas, D. Domingo, and J. Yahalom. A novel response of cancer cells to radiation involves autophagy and formation of acidic vesicles. *Cancer Res.*, 61:439–444, 2001.

[173] J.J. Lum, D.E. Bauer, M. Kong, M.H. Harris, C. Li, T. Lindsten, and C.B. Thompson. Growth factor regulation of autophagy and cell survival in the absence of apoptosis. *Cell*, 120:237–248, 2005.

Appendices

Appendix A

Cell Cycle Distributions

Relative proportions of cells in G1, G2 and S phase as a function of dose and time post irradiation are presented for all four cell lines during a full experiment.

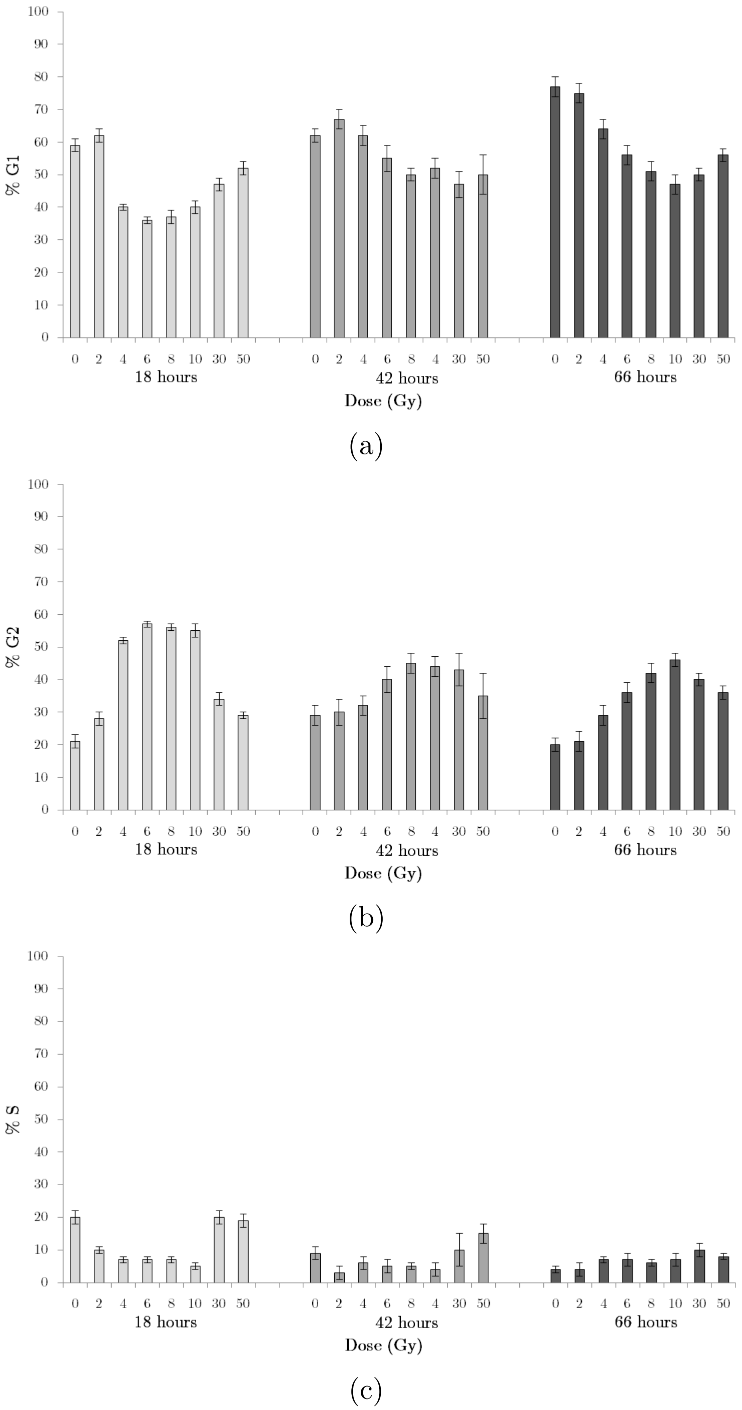

(a)

(b)

(c)

Figure A.1: Relative proportions of H460 cells in (a) G1, (b) G2 and (c) S phase of cell cycle as a function of dose at 18, 42 and 66 hours post irradiation.

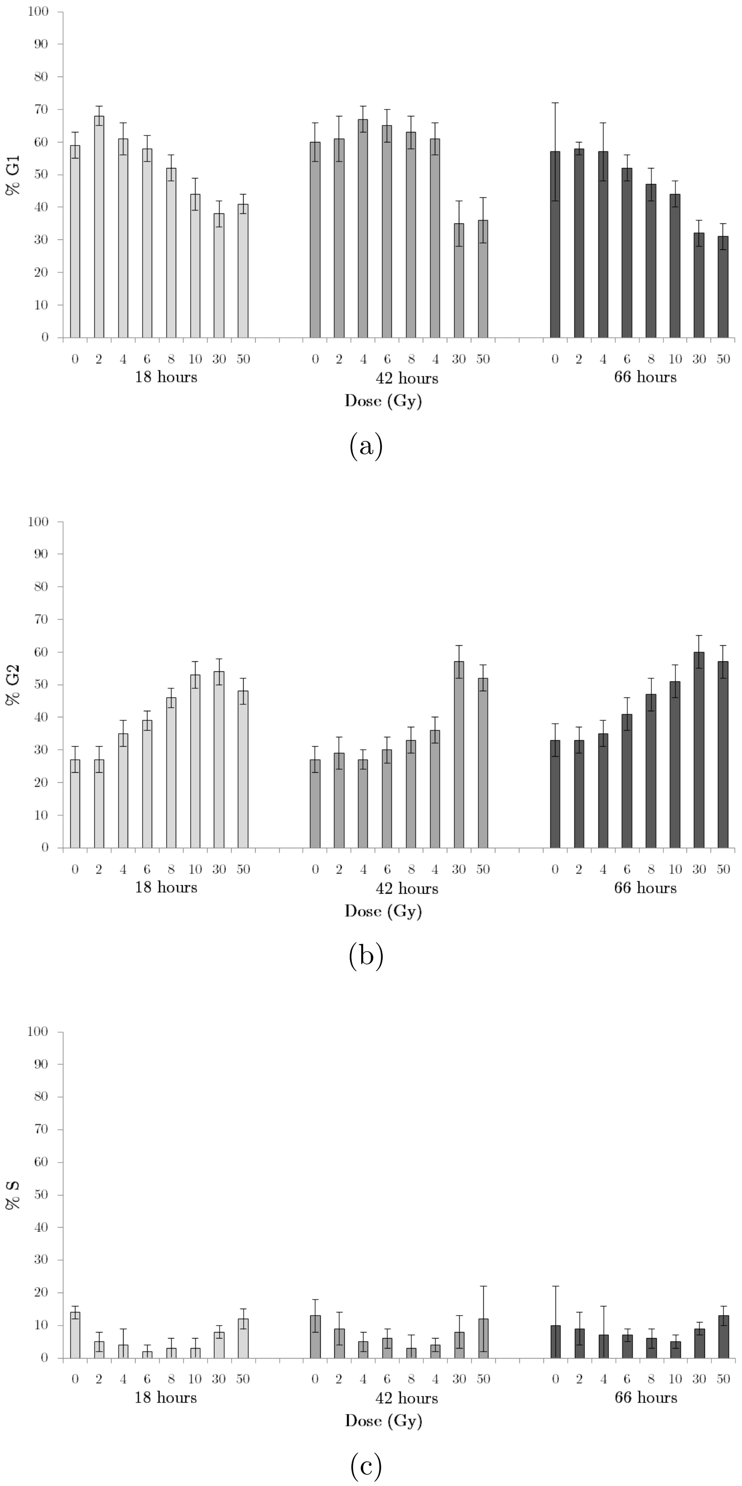

(a)

(b)

(c)

Figure A.2: Relative proportions of MCF-7 cells in (a) G1, (b) G2 and (c) S phase of cell cycle as a function of dose at 18, 42 and 66 hours post irradiation.

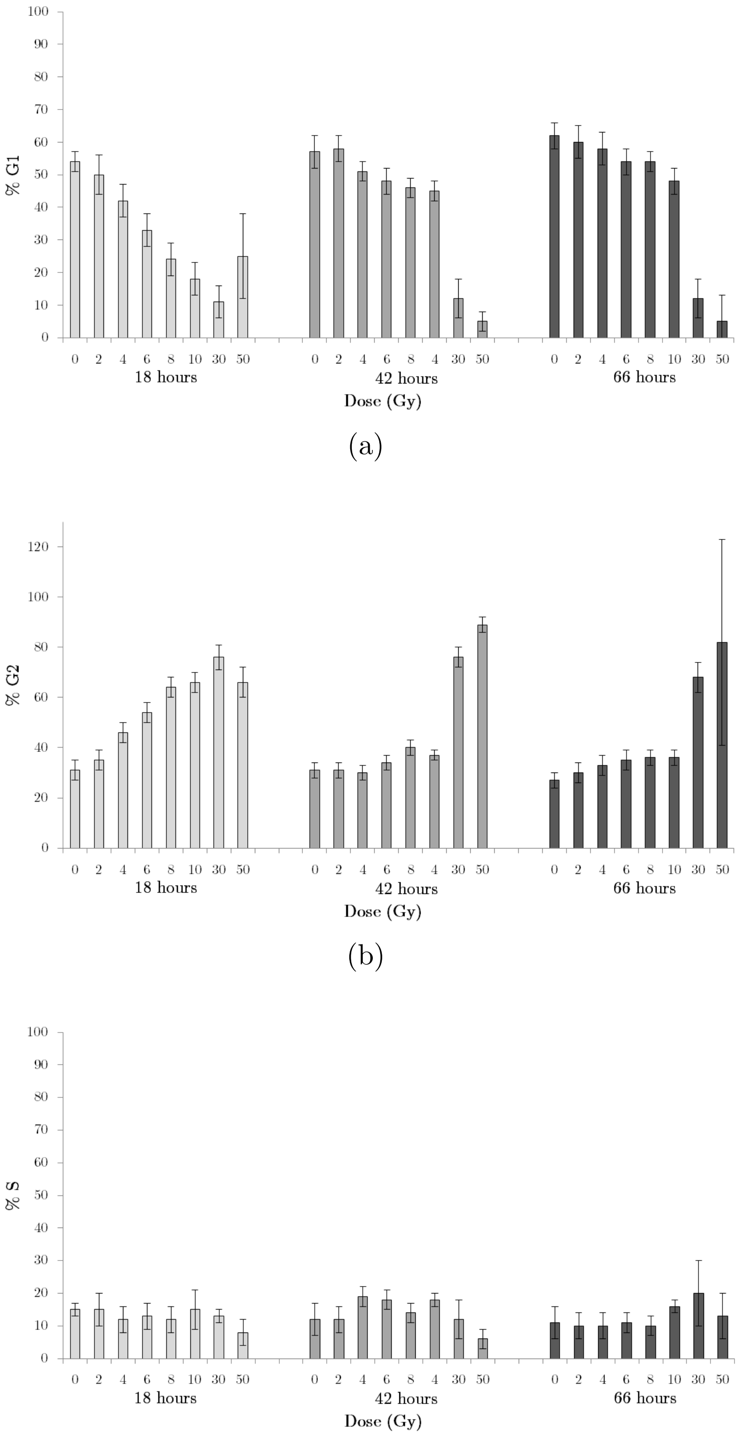

(a)

(b)

(c)

Figure A.3: Relative proportions of MDA-MB-231 cells in (a) G1, (b) G2 and (c) S phase of cell cycle as a function of dose at 18, 42 and 66 hours post irradiation.

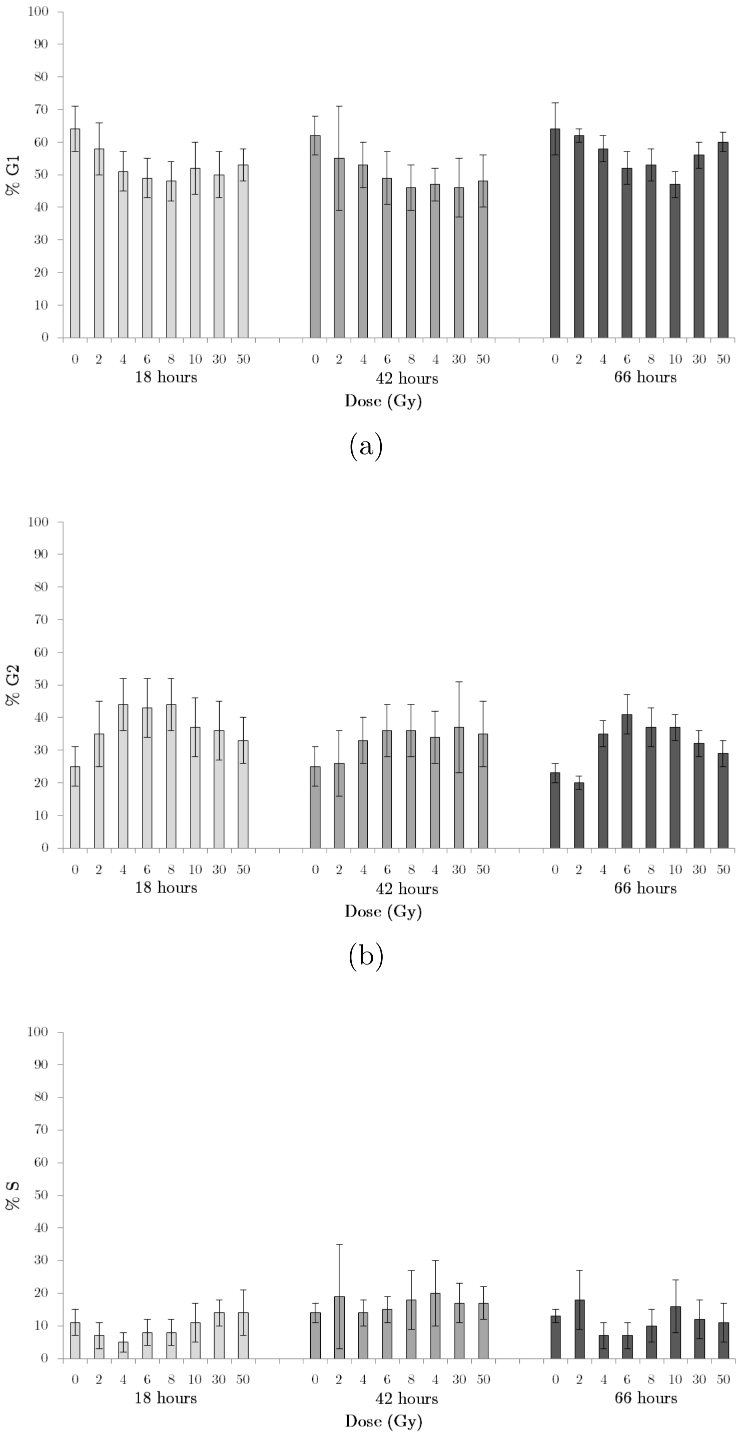

(a)

(b)

(c)

Figure A.4: Relative proportions of LNCaP cells in (a) G1, (b) G2 and (c) S phase of cell cycle as a function of dose at 18, 42 and 66 hours post irradiation.

Appendix B

Population Viability

Fraction of viable cells in the H460, MCF-7, MDA-MB-231 and LNCaP experiments.

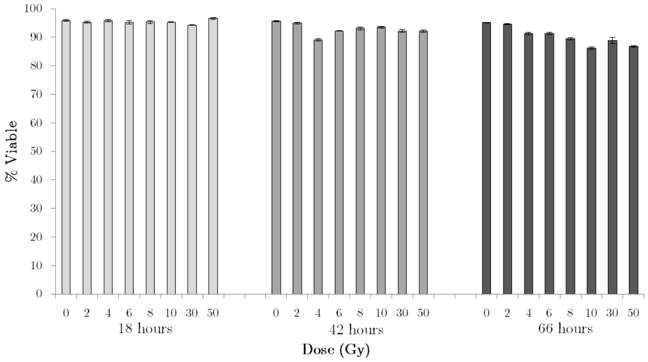

Figure B.1: Fraction of viable cells in the H460 experiment populations as a function of dose at 18, 42 and 66 hours post irradiation.

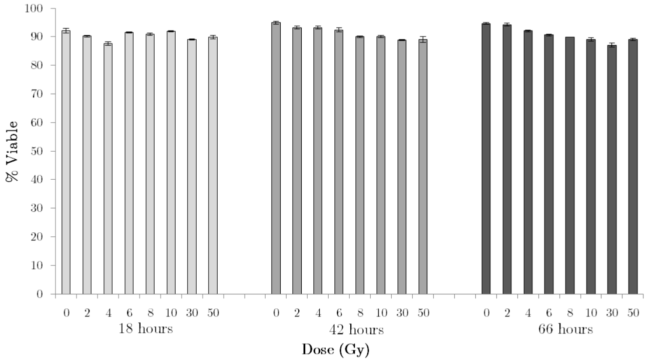

Figure B.2: Fraction of viable cells in the MCF-7 experiment populations as a function of dose at 18, 42 and 66 hours post irradiation.

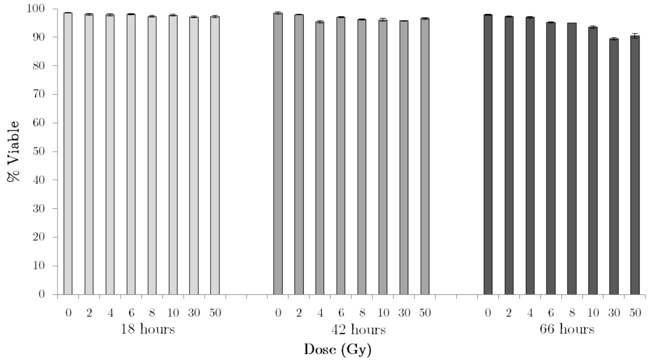

Figure B.3: Fraction of viable cells in the MDA-MB-231 experiment populations as a function of dose at 18, 42 and 66 hours post irradiation.

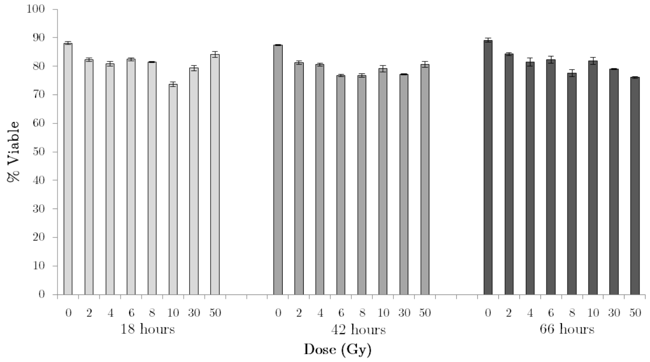

Figure B.4: Fraction of viable cells in the LNCaP experiment populations as a function of dose at 18, 42 and 66 hours post irradiation.

Appendix C

Total Cell Counts

Absolute total (viable + dead) cell counts in each population for the H460, MCF-7, MDA-MB-231 and LNCaP experiments.

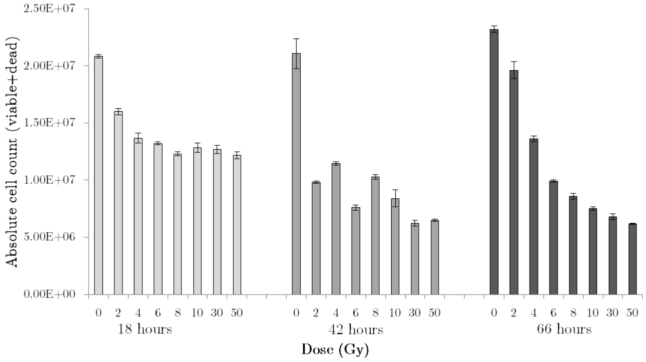

Figure C.1: Total number of cells in the H460 experiment populations as a function of dose at 18, 42 and 66 hours post irradiation.

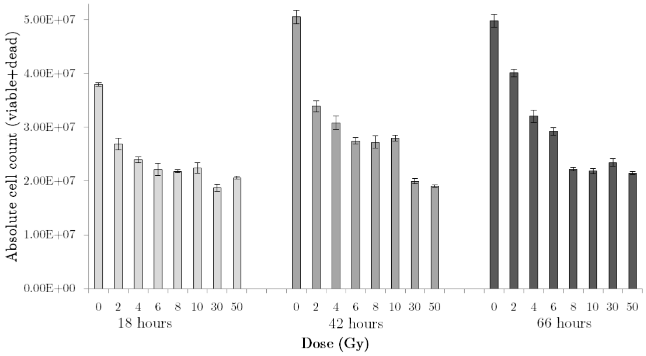

Figure C.2: Total number of cells in the MCF-7 experiment populations as a function of dose at 18, 42 and 66 hours post irradiation.

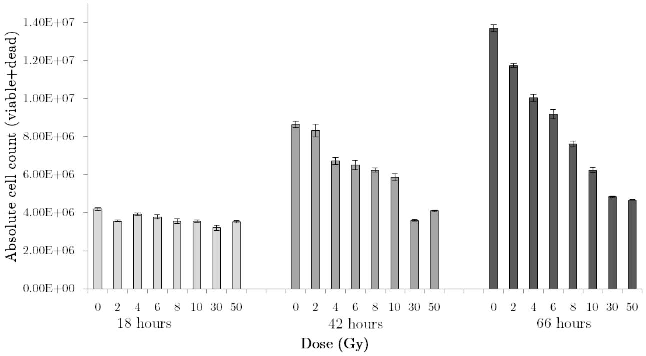

Figure C.3: Total number of cells in the MDA-MB-231 experiment populations as a function of dose at 18, 42 and 66 hours post irradiation.

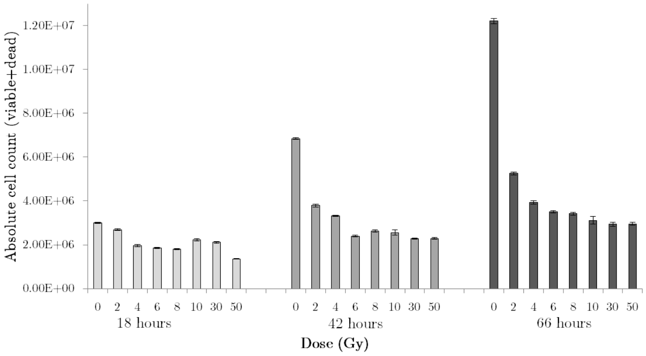

Figure C.4: Total number of cells in the LNCaP experiment populations as a function of dose at 18, 42 and 66 hours post irradiation.

Appendix D

Additional Raman Components

D.1 H460

Component 3

Component 3 accounts for 5.5% of the total variance in the low dose data set and 4.7% of the total variance in the high dose data set. Component 3 of the high dose data set is identical to component 3 of the low dose data set with an r-value of 1.00 ± 0.07%.

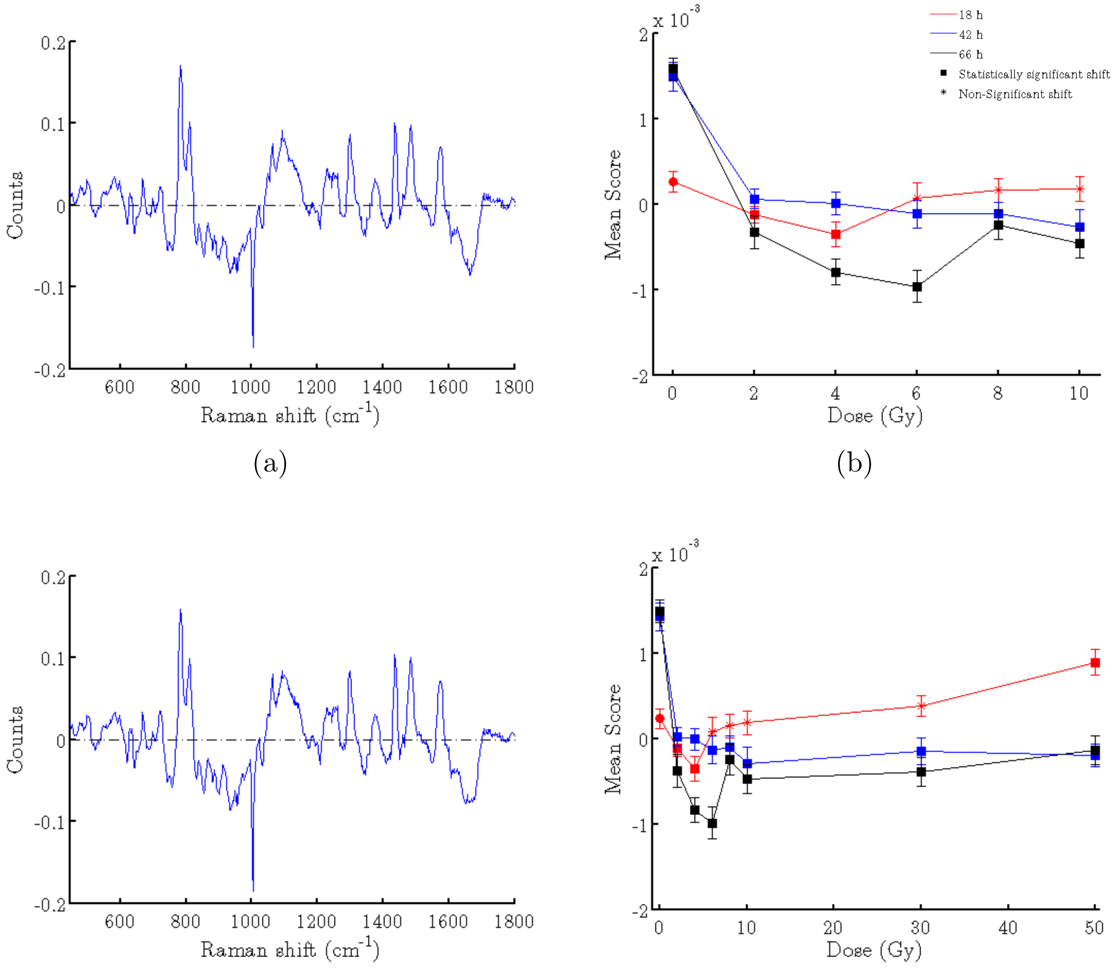

(a) (b)

(c) (d)

Figure D.1: Component 3 and corresponding score plot for the H460 low dose data set (a) & (b) and the high dose data set (c) & (d).

D.2 MCF-7

Component 4

Component 4 accounts for 3.0% of the total variance in the low dose data set. Component 3 of the high dose data set is highly correlated to component 4 of the low dose data set with an r-value of 0.99 ± 0.2%. Component 3 makes up 2.8% of the total variance in the high dose data set.

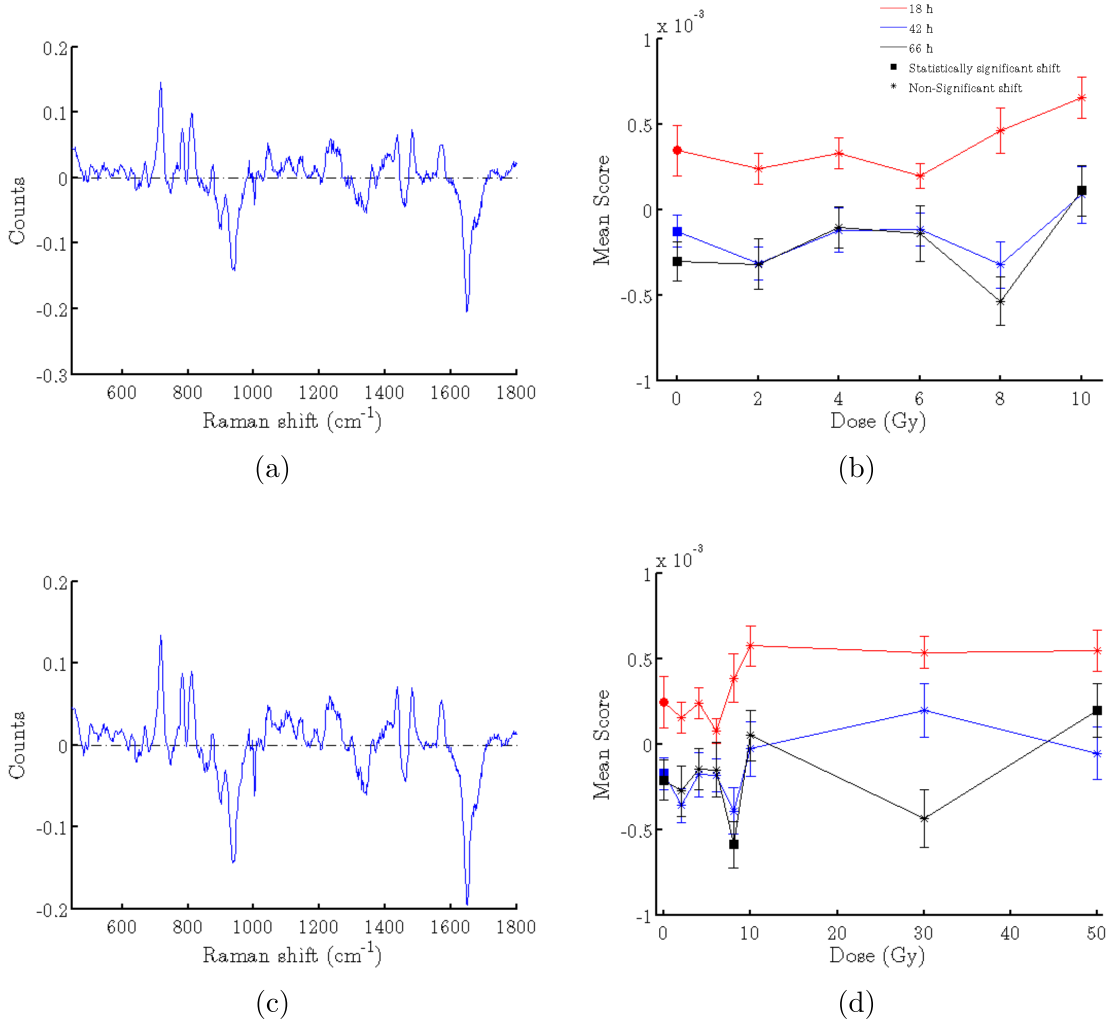

(a) (b)

(c) (d)

Figure D.2: Component 4 and corresponding score plot for the MCF-7 low dose data set (a) & (b) as well as the highly correlated component 3 of the high dose data set (c) & (d).

D.3 MDA-MB-231

Component 4

Component 4 accounts for 3.0% of the total variance in the low dose data set and 2.9% of the total variance in the high dose data set. Component 4 of the high dose data set is nearly identical to that in the low dose data set, with an r-value of 0.99 ± 0.2%.

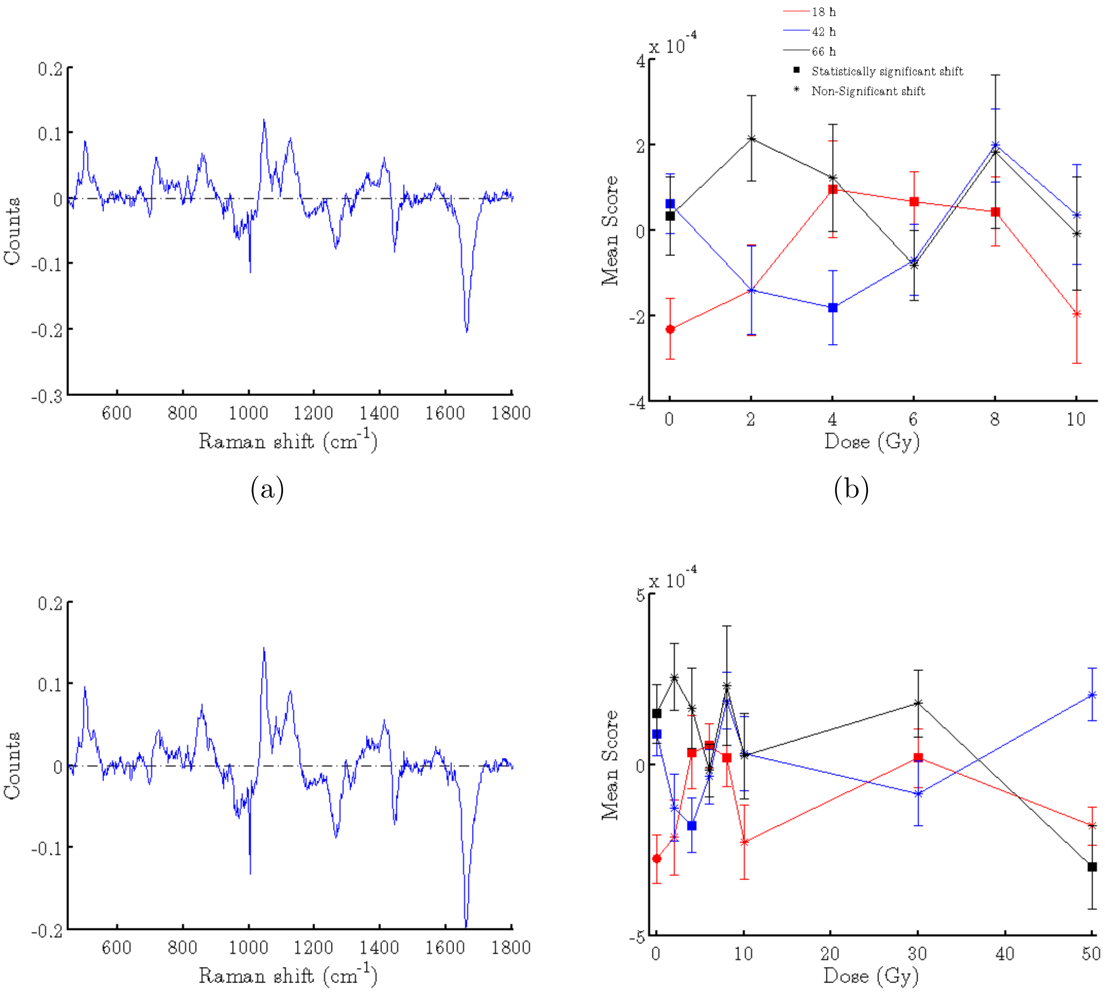

(a) (b)

(c) (d)

Figure D.3: Component 4 and corresponding score plot for the MDA-MB-231 low dose data set (a) & (b) and high dose data set (c) & (d).

Component 5

Component 5 of the high dose data set was reproducible between the two independently repeated MDA-MB-231 experiments and accounts for 2.4% of the total variance. Component 5 of the low dose data set was not reproducible between independent experiments and therefore is not presented.

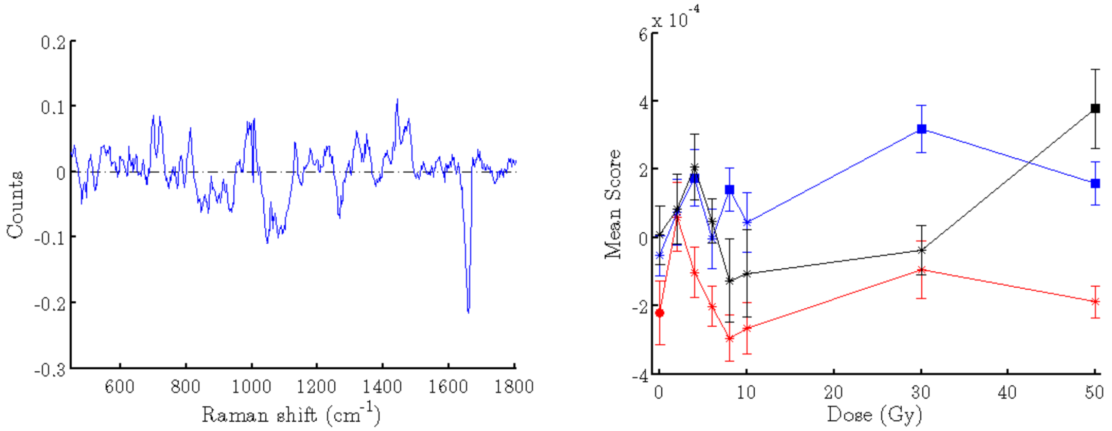

(a) (b)

Figure D.4: Component 5 and corresponding score plot for the MDA-MB-231 high dose data set.

Component 6

Component 6 of the high dose data set was reproducible between the two independent MDA-MB-231 experiments and accounts for 1.7% of the total variance. Component 6 of the low dose data set was not reproducible between independent experiments and therefore is not presented.

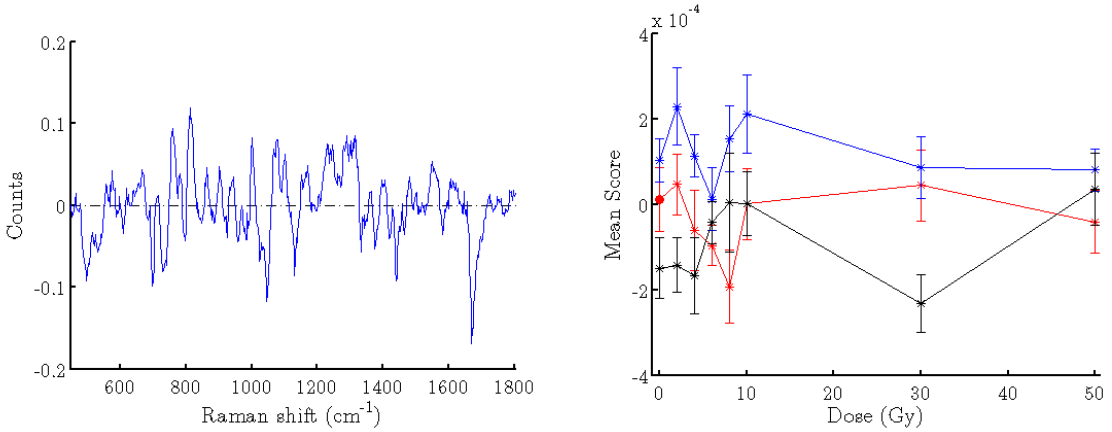

(a) (b)

Figure D.5: Component 6 and corresponding score plot for the MDA-MB-231 high dose data set.

D.4 LNCaP

Component 4

Component 4 accounts for 2.7% of the total variance in the low dose data set and 2.8% of the total variance in the high dose data set. Between the low and high dose data sets component 4 is very similar with an r-value of 0.99 ± 0.2%.

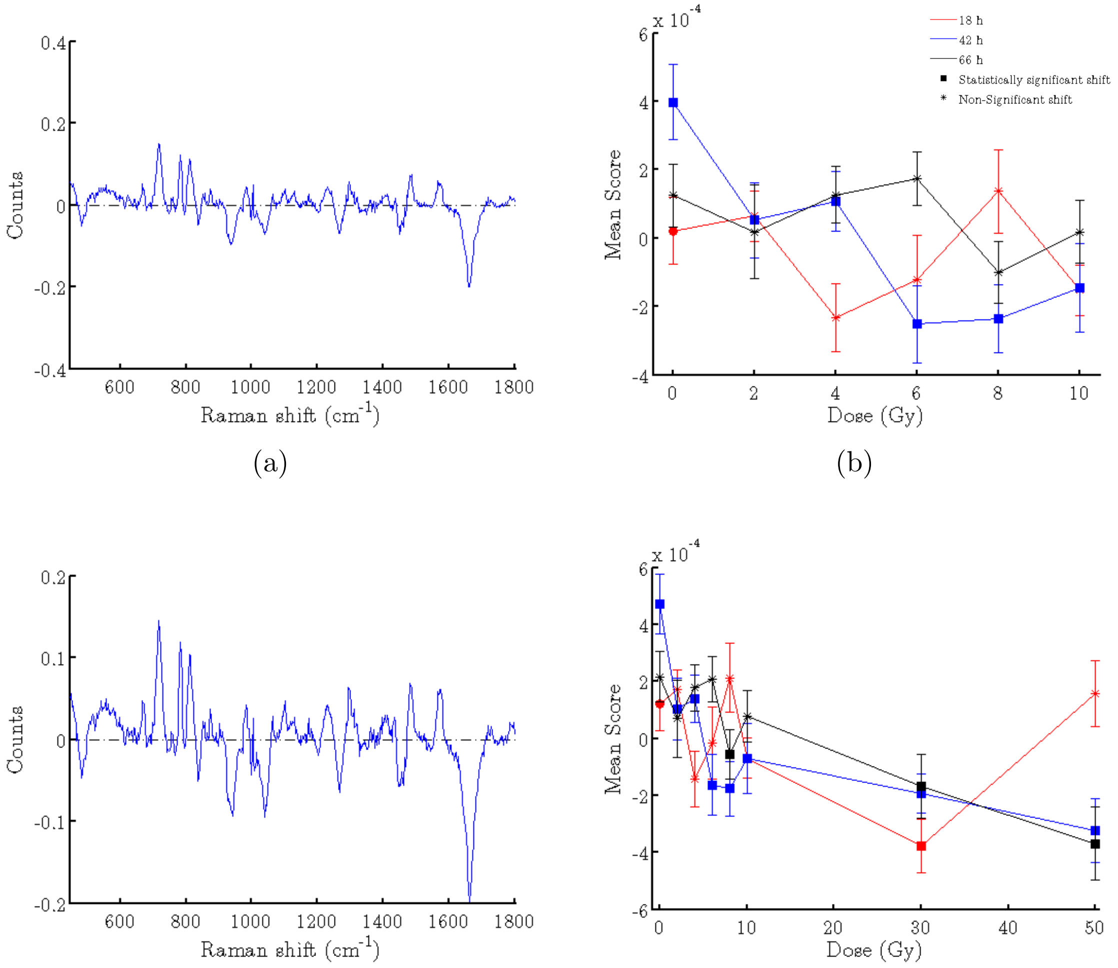

(a) (b)

(c) (d)

Figure D.6: Component 4 and corresponding score plot for the LNCaP low dose data set (a) & (b) and high dose data set (c) & (d).